

**PERFORMANCE AND LONG-TERM STABILITY OF SURFACE-
ENHANCED RAMAN SCATTERING SUBSTRATES
FABRICATED BY DEALLOYING OF GOLD-SILVER
NANOSTRUCTURES**

by

Uraivan Waiwijit

A Dissertation Submitted in Partial Fulfillment of the Requirements for the Degree of
Doctor of Philosophy in Nanotechnology

Examination Committee: Dr. Tanujjal Bora (Chairperson)
Dr. Noppadon Nuntawong (Co-chairperson)
Dr. Gabriel Louis Hornyak
Dr. Oleg Shipin

External Examiner: Prof. Gang Meng
Anhui Institute of Optics and Fine Mechanics
Chinese Academy of Sciences (CAS)
Anhui, China

Nationality: Thai

Previous Degree: Master of Science in Medical Biochemistry
Chulalongkorn University
Thailand

Scholarship Donor: Royal Thai Government - AIT Fellowship

Asian Institute of Technology
School of Engineering and Technology
Thailand
July 2021

AUTHOR'S DECLARATION

I, Uraiwan Waiwijit, declare that the research work carried out for this dissertation was in accordance with the regulations of the Asian Institute of Technology. The work presented in it are my own and has been generated by me as the result of my own original research, and if external sources were used, such sources have been cited. It is original and has not been submitted to any other institution to obtain another degree or qualification. This is a true copy of the dissertation, including final revisions.

Date: July 2021

Name: Uraiwan Waiwijit

Signature: Uraiwan Waiwijit

ACKNOWLEDGMENTS

First of all, I would like to express my special thanks and sincere gratitude to my advisors: Dr. Tanujjal Bora as well as Dr. Noppadon Nuntawong who give me an opportunity to conduct this research. They supported me throughout the work with several ideas, invaluable guidance, suggestions, and necessary facilities. Thanks to them for their patience, time and effort that helped me stay on the track and complete this research successfully.

Besides, I wish to express my sincere thanks to the rest of my thesis committee: Dr. Gabriel Louis Hornyak and Dr. Oleg Shipin for their worthy support, insightful comments, ideas, and suggestions throughout the period of this research. This dissertation would never have been completed without their guidance and persistent help.

I would also like to thank The Royal Thai Government Fellowship (RTG Fellowship) and AIT Fellowship for financial support and the golden opportunity for being a student here.

My thanks to my colleagues and friends who work at National Electronics and Computer Technology Center (NECTEC), National Nanotechnology Center (NANOTEC) and Center of Excellence in Nanotechnology (CoEN) for their help, academic support, valuable opinions, and inspiration.

Finally, I would like to express my most grateful acknowledgement to my family. Their love, understanding, inspiration and encouragement have motivated me to go through all the challenges and hard time in my life.

ABSTRACT

We describe a fabrication method of gold-silver (Au-Ag) nanorods with chemical dealloying process to improve surface-enhanced Raman scattering (SERS) performance and stability. The Au-Ag alloy nanorods are prepared by two different methods. In method one we first sputter Ag nanorods followed by a galvanic replacement of Ag with Au; and in the second method Au-Ag alloy nanorods are directly prepared by co-sputtering using glancing angle deposition method. Dealloying is then performed using acid or base etching in both the cases. The dealloying process of the Au-Ag film fabricated via galvanic replacement was unsuccessful and thus the SERS performance and stability is further carried out only with the Ag-Au nanorods prepared by glancing angle deposition method. For this second method, the SERS sensitivity of the Au-Ag nanorods was improved to 10^{-9} M for 4-mercaptobenzoic acid (4-MBA) used as Raman probe, compared to the pure Ag substrates, with similar shelf-life. For co-sputtering, the optimum condition of Au-Ag dealloyed substrate is achieved after immersing the as-deposited Au-Ag film in 30% NH_4OH : 30% H_2O_2 : methanol for 40 s. Due to its surface roughness, this substrate exhibits an enhancement factor of 1.5×10^6 . Long-term stability of the dealloyed substrates was observed over a month and found superior to the alloyed and Ag substrates. In addition, the dealloyed substrates are used for the detection of urinary crystals and clearly demonstrated SERS spectra of 10^{-4} M synthetic urinary crystals solution composed of calcium oxalate monohydrate, calcium phosphate and uric acid. For uric acid, the substrates showed a good performance with a linear range of 0- 10^{-5} M and detection limit of 1.27×10^{-6} M, which is less than the normal range of uric acid in healthy human. The Au-Ag dealloyed SERS substrates prepared in this study showed potential for early diagnosis of uric acid-type kidney stone diseases.

CONTENTS

	Page
ACKNOWLEDGMENTS	iii
ABSTRACT	iv
LIST OF TABLES	ix
LIST OF FIGURES	xi
LIST OF ABBREVIATIONS	xvi
CHAPTER 1 INTRODUCTION	1
1.1 Background of the Study	1
1.2 Statement of the Problem	2
1.3 Objectives of the Research	4
1.4 Scope of the Study	4
1.5 Organization of the Thesis	5
CHAPTER 2 LITERATURE REVIEW	6
2.1 Raman Spectroscopy	6
2.2 Surface-Enhanced Raman Scattering (SERS)	9
2.2.1 SERS Mechanisms	10
2.3 Alloy SERS Substrates Fabrication	12
2.3.1 Nanoparticles in Suspension	13
2.3.2 Nanoparticles Immobilization on Substrate	14
2.3.3 Nanopattern Arrays on Planar Substrate	16
2.3.4 Galvanic Replacement	24
2.3.5 Dealloying Process	27
2.4 Summary	30
CHAPTER 3 METHODOLOGY	32
3.1 Concepts	32
3.2 Materials	33

	Page
3.3 Fabrication of Au-Ag Dealloyed Substrates (Approach 1)	34
3.2.1 Au-Ag Bimetallic Substrate Preparation	34
3.2.1 Dealloying of Au-Ag Bimetallic Substrates	35
3.4 Fabrication of Au-Ag Dealloyed Substrates (Approach 2)	36
3.5 Characterization of Samples	37
3.5.1 Sample Morphological and Chemical Analysis	37
3.5.2 Surface Wettability Test	37
3.5.3 Optical Characterization	38
3.5.4 Crystallographic Characterization	38
3.5.5 Titration	38
3.6 Raman Measurement	39
3.7 Urinary Crystal Detection	40
3.8 Data Analysis	41
3.8.1 SERS Enhancement factor	41
3.8.2 Limit of Detection	42
CHAPTER 4 RESULTS AND DISCUSSION	43
4.1 Fabrication of Au-Ag Bimetallic Nanorods via Galvanic Replacement and Dealloying Process	43
4.1.1 Ag Film Morphology	43
4.1.2 Au-Ag Bimetallic Film Morphology and Composition	44
4.1.3 Optical and Crystallographic Properties of the Au-Ag Bimetallic Thin Films	49
4.1.4 Raman Characterization and SERS Performance of the Au-Ag Bimetallic Substrates	51
4.1.5 Selective Etching of the Au-Ag Bimetallic Substrates	52
4.1.6 Sensitivity Measurement	56
4.1.7 Long Term Performance	57
4.2 Fabrication of Au-Ag Alloyed Nanorods by Co-sputtering Deposition and Dealloying Process	58
4.2.1 Au-Ag Alloyed Film Morphology and Composition	58

	Page
4.2.2 Selective Etching of the Au-Ag Alloyed Substrates	61
4.2.3 4-MBA Detection	65
4.2.4 Surface Chemical Composition of the Substrates	67
4.2.5 Surface Wettability of the Substrates	68
4.2.6 Optical and Crystallographic Properties of the Substrates	70
4.2.7 Raman Characterization	71
4.2.8 Sensitivity Measurements	73
4.2.9 Reproducibility and Reliability	75
4.2.10 Long Term Performance	76
4.3 Urinary Crystal Detection Using Au-Ag Dealloyed Substrate	77
4.3.1 Crystals Dissolved in Deionized (DI) Water	78
4.3.2 Uric Acid Dissolved in DI Water	80
4.3.3 Uric Acid Detection in Synthetic Urine	81
CHAPTER 5 CONCLUSION AND RECOMMENDATIONS	85
5.1 Conclusion	85
5.1.1 Au-Ag Bimetallic Nanorods via Galvanic Replacement and Dealloying Process	85
5.1.2 Au-Ag Alloyed Nanorods by Co-sputtering Deposition and Dealloying Process	87
5.1.3 Urinary Crystal Detection Using Au-Ag Dealloyed Substrate	88
5.2 Recommendation	88
5.2.1 Fabrication of Au-Ag Bimetallic Nanorods via Galvanic Replacement and Dealloying Process	88
5.2.2 Fabrication of Au-Ag Alloyed Nanorods by Co- sputtering Deposition and Dealloying Process	89
5.2.3 Urinary Crystal Detection Using Au-Ag Dealloyed Substrate	89
REFERENCES	91

	Page
APPENDICES	108
APPENDIX A: DETERMINATION OF 4-MBA MOLECULES ADSORBED ON SERS SUBSTRATES	109
APPENDIX B: SYNTHESIS AND MORPHOLOGY OF PURE AG AND AU SUBSTRATES	111
APPENDIX C: SERS ENHANCEMENT FACTOR CALCULATION	112
APPENDIX D: OTHER ORGANIC MOLECULES DETECTION	115
VITA	120

LIST OF TABLES

Tables	Page
Table 2.1 Comparable Advantages of Three Categories for Alloy SERS Substrate Fabrication	24
Table 2.2 Standard Reduction Potentials for the Half-reaction of AuCl_4^- and Ag	25
Table 4.1 Elemental Composition of the Au-Ag Bimetallic Thin Films Obtained for EDS Analysis. The Au-Ag Bimetallic Structures Were Obtained by Galvanic Replacement of Ag With 0.01 wt% HAuCl_4 Solution for Varying Immersion Time Ranging From 1-10 Minutes	47
Table 4.2 Elemental Composition of the Au-Ag Bimetallic Thin Films Obtained for EDS Analysis. The Au-Ag Bimetallic Structures Were Obtained by Galvanic Replacement of Ag With 0.001 wt% HAuCl_4 Solution for Varying Immersion Time Ranging From 1-10 Minutes	48
Table 4.3 Elemental Composition of the Au-Ag Dealloyed Films Obtained by Etching With 10% HNO_3 Solution at Different Etching Times (0-15 Minutes)	54
Table 4.4 Elemental Composition of Au-Ag Alloyed Nanorods Fabricated With 10, 30 and 50 W of Au Sputtering Power. Ag Sputtering Power was Kept Constant at 80 W During the Process	60
Table 4.5 Elemental Composition of the Au-Ag Alloyed Substrates Fabricated by the Co-sputtering Method and After Etching With 10% HNO_3 Solution up to 15 Minutes	62
Table 4.6 LOD of Uric Acid Dispersed in DI Water Calculated From the Peaks of 632, 1132 and 1214 cm^{-1}	80

	Page
Table 4.7 LOD of Uric Acid Spiked in Synthetic Urine Calculated From the Peaks of 637, 1139 and 1214 cm^{-1}	83
Table 4.8 Summarizes the Performance of Various SERS Substrate for Uric Acid Determination	84

LIST OF FIGURES

Figures	Page
Figure 1.1 Applications of SERS Technique in Various Fields	2
Figure 2.1 The Schematic Diagram of Photon Scattering With Elastic and Inelastic Scattering. (b) Raman Shift of Stoke and Anti-Stoke Scattering	7
Figure 2.2 SERS Chemical Enhancement	10
Figure 2.3 (a) Schematic Representation of SERS Electromagnetic Enhancement Mechanism. (b) The Electromagnetic Enhancement Mechanism Steps	12
Figure 2.4 DC Magnetron Sputtering System	19
Figure 2.5 (a) SEM Image of Au-Ag Nanowire Based on LIL and Sputtering Deposition. (b) Au@Ag/ Pyramidal Silicon 3D Structure Fabricated by a Wet Texturing Process Incorporated With Sputtering. (c) Au-Cu Nanowires by LIL and Sputtering After Electrochemically Dealloying. (d) Gradient Nanoporous Gold Fabricated by Magnetron Sputtering and Dealloying Technique	21
Figure 2.6 Schematic of Glancing Deposition Technique	22
Figure 2.7 Schematic of Au-Ag Formation via Galvanic Replacement	26
Figure 2.8 Schematic of Dealloying Process	28
Figure 2.9 SEM Images of Au-Ag Nanowires Array Fabricated by Electrodeposition Method and HNO ₃ Etching	29
Figure 3.1 Flow Chart of Thesis Methodology	33
Figure 3.2 (a) Schematic of Au-Ag Bimetallic Fabrication and (b) Dealloying Process	35
Figure 3.3 Schematic of Au-Ag Alloyed Fabrication and Dealloying Process	37
Figure 3.4 Raman Instrument	40

	Page
Figure 3.5 Chemical Structure of Calcium Oxalate Monohydrate (COM), Calcium Phosphate (CAP) and Uric Acid	41
Figure 4.1 SEM Images of (a) top and (b) Cross-section of Ag Thin Film Fabricated by GLAD Sputtering With Rotation of Silicon Substrate	44
Figure 4.2 SEM Images of the top and Cross-sectional SEM Views of the Ag Film After Immersion in 0.1 wt% HAuCl ₄ Solution for (a, d) 1, (b, e) 3 and (c, f) 5 Minutes	45
Figure 4.3 SEM micrographs of Au-Ag Bimetallic Thin Films Obtained by Galvanic Replacement of Ag With 0.01 wt% HAuCl ₄ Solution for (a) 1, (b) 3, (c) 5 and (d) 10 Minutes	46
Figure 4.4 SEM Micrographs of Au-Ag Bimetallic Thin Films Obtained by Galvanic Replacement of Ag With 0.001 wt% HAuCl ₄ Solution for (a) 1, (b) 3, (c) 5 and (d) 10 Minutes	48
Figure 4.5 (a) UV-vis Absorption Spectra and (b) XRD Patterns of Pure Ag, Pure Au and Au-Ag Bimetallic Substrates	50
Figure 4.6 (a) Raman Spectrum of 10 ⁻⁴ M 4-MBA on the Au-Ag Bimetallic Substrate With Different Immersion Time in 0.01 wt% HAuCl ₄ Solution and (b) Variations in the Raman Intensities of the 4-MBA Characteristic Peaks at 1078 and 1587 cm ⁻¹	52
Figure 4.7 SEM Micrographs of Au-Ag Dealloyed Substrates Obtained by using 10% HNO ₃ Solution as Etchant Showing the Surface Morphology at Different Etching Time	53
Figure 4.8 (a) SERS Intensity of 10 ⁻⁴ M 4-MBA on the Au-Ag Dealloyed Substrates Obtained by Etching with 10% HNO ₃ Solution at Different Time (0-15 Minutes) and (b) Variations of the Raman Intensities of the Characteristic Peaks of 4-MBA (1078 and 1587 cm ⁻¹) With Respect to the Dealloying Time	55

	Page
Figure 4.9 (a) SERS Intensity of 10^{-9} - 10^{-3} M 4-MBA on Ag Substrate (b) on Au-Ag Bimetallic Substrate. Dependence of the 4-MBA Concentration and Raman Intensities at Characteristic Peaks of (c) 1587 and (d) 1078 cm^{-1}	57
Figure 4.10 (a) SERS Signal of 10^{-4} M 4-MBA at 1078 cm^{-1} Characteristic Peak on Pure Ag and Au-Ag Bimetallic (0.01 wt% HAuCl_4 for 3 Minutes) Substrates and (b) Shelf life Until 35 Days	58
Figure 4.11 Surface and Cross-sectional SEM Images of Au-Ag Alloyed Substrates Fabricated by Co-sputtering With Fixed 80 W Ag Sputtering Power and Varied Au Sputtering Power of (a-d) 10 W (b-e) 30 W and (c) 50 W	59
Figure 4.12 Raman Spectra of 10^{-4} M 4-MBA on the Au-Ag Alloyed Substrates Fabricated with 10, 30 and 50 W Au Sputtering Power	61
Figure 4.13 SEM Micrographs of Au-Ag Alloyed Substrates (a) Before and (b-d) After Etching with 10% HNO_3 Solution at Different Etching Times of 5, 10 and 15 Minutes	62
Figure 4.14 (a) SERS Intensity of 10^{-4} M 4-MBA on the Au-Ag Alloyed Substrate with 10% HNO_3 Etching for 0-15 Minutes and (b) Dependence of the Dealloying Time and Raman Intensities at Characteristic Peaks of 1078 and 1587 cm^{-1} of 10^{-4} M 4-MBA	63
Figure 4.15 Surface and Cross-sectional SEM Images of Au-Ag Alloyed Substrates With Different Dealloying Times	64
Figure 4.16 Titration Curve of 4-MBA Titrated With Strong Base (NaOH) of Au-Ag Alloyed Substrate (a); and (b), for the Au-Ag Dealloyed Substrate	66
Figure 4.17 Schematic Representation Describing the Dealloying Process of the Au-Ag Alloyed Substrates Prepared by co-	67

	Page
Sputtering Deposition Method in $\text{NH}_4\text{OH}:\text{H}_2\text{O}_2$: Methanol Etching Solution	
Figure 4.18 (a) The complete XPS spectra of Au-Ag alloyed and dealloyed substrates. (b) Main peaks of Ag 3d and Au 4f of the Au-Ag alloyed substrates and (c) Au-Ag dealloyed substrates.	68
Figure 4.19 The Water Contact Angle and Drop Profile of Au-Ag Alloyed Substrate (Before Etching) and Au-Ag Dealloyed Substrate With Different Dealloying Times	70
Figure 4.20 (a) UV-Visible Absorption Spectra and (b) XRD Patterns of Pure Au, Pure Ag, Au-Ag Alloyed Nanorods and 40 s Etched Au-Ag Dealloyed Nanorod Samples	71
Figure 4.21 (a) SERS Spectra of 10^{-4} M 4-MBA on the Au-Ag Dealloyed SERS Substrates for Different Etching Times 0, 20, 40, 60, 80, 100 and 120 s From Top-to-bottom. (b) Raman Intensities of 4-MBA at Characteristic Peaks of 1587 cm^{-1} and 1078 cm^{-1} Derived From Spectra Depicted in (a)	72
Figure 4.22 Raman Intensities of 4-MBA at Characteristic Peaks of 1587 cm^{-1} and 1078 cm^{-1} for Different 30% H_2O_2 : 30% NH_4OH : Methanol Etching Time 2-5 Minutes	73
Figure 4.23 Raman Spectra of 4-MBA Molecules With Concentration Ranging From 10^{-4} to 10^{-9} M Absorbed (a) on the Au-Ag Alloyed Substrates (Before Etching) and (b) on the Au-Ag Dealloyed Substrates (40 s etching). SERS Intensity of the Characteristic 4-MBA Raman Bands on the Alloyed and Dealloyed Substrates at (c) 1587 cm^{-1} and for (d) 1078 cm^{-1} as a Function of 4-MBA Concentrations	75
Figure 4.24 (a) SERS Spectra of 10^{-4} M 4-MBA Collected From 30 Different Spots on the Au-Ag Dealloyed Substrates. (b)	76

	Page
Raman Intensities of 30 Spectra at Wavenumber of 1587 cm ⁻¹ and 1078 cm ⁻¹	
Figure 4.25 SERS Signal of 10 ⁻⁴ M 4-MBA at 1078 cm ⁻¹ Characteristic Peak on Pure Ag, Au-Ag Alloyed and Au-Ag Dealloyed Substrates for 35 Days	77
Figure 4.26 SERS Spectrum and Chemical Structure of 10 ⁻⁴ M COM, CAP and Uric Acid Dispersed in DI Water on the Au-Ag Dealloyed and Bare Silicon Substrates	79
Figure 4.27 (a) SERS Spectrum of Uric Acid Dispersed in DI at Different Concentration of 10 ⁻⁷ -10 ⁻³ M. The Signal Intensity at Raman Peak of (b) 632 cm ⁻¹ , (c) 1134 cm ⁻¹ and (d) 1214 cm ⁻¹ at Various Concentrations, 10 ⁻⁷ M to 10 ⁻⁴ M	81
Figure 4.28 (a) SERS Spectrum of Uric Acid Dispersed in Synthetic Urine at Different concentration of 10 ⁻⁷ -10 ⁻³ M. The Signal Intensity at Raman Peak of (b) 637 cm ⁻¹ , (c) 1139 cm ⁻¹ and (d) 1214 cm ⁻¹ at Various Concentrations, 10 ⁻⁷ M to 10 ⁻⁴ M	83

LIST OF ABBREVIATIONS

2D	= Two Dimensions
3D	= Three Dimensions
AAO	= Anodic Aluminum Oxide
AgNPs	= Silver Nanoparticles
AuNPs	= Gold Nanoparticles
BET	= Brunauer-Emmett-Teller
CAP	= Calcium Phosphate
CCD	= Charge Coupled Device
CM	= Chemical Mechanism
COM	= Calcium Oxalate Monohydrate
DC	= Direct Current
DI	= Deionized water
EDS	= Energy-Dispersive X-Ray Spectroscopy
EF	= Enhancement Factor
EBL	= Electron Beam Lithography
EM	= Electromagnetic Mechanism
FCC	= Face Centered Cubic
FESEM	= Field Emission Scanning Electron Microscopy
FWHM	= Full-Width at Half Maximum
GLAD	= Glancing Angle Deposition
GRR	= Galvanic Replacement Reaction
LIL	= Laser Interference Lithography
LOD	= Limit of Detection
LSPR	= Localized Surface Plasmon Resonance
M	= Molarity
NPs	= Nanoparticles
OAD	= Oblique Angle Deposition
PLAL	= Pulsed Laser Ablation
PVD	= Physical Vapor Deposition
RF	= Radio Frequency

RSD	= Relative Standard Deviation
RT	= Room Temperature
SCCM	= Standard Cubic Centimeters per Minute
SD	= Standard Deviation
SERS	= Surface-Enhanced Raman Scattering
SHE	= Standard Hydrogen Electrode
TEM	= Transmission Electron Microscope
XPS	= X-Ray Photoelectron Spectroscopy
XRD	= X-Ray Diffraction
WCA	= Water Contact Angle

CHAPTER 1

INTRODUCTION

1.1 Background of the Study

SERS is a surface-sensitive technique that utilizes surface plasmon properties of metal nanostructures to enhance Raman scattering signals by molecules adsorbed on the metallic surfaces. This technique is very sensitive and specific which allows it to identify trace molecules or even single molecule detection. Owing to its ability, SERS technique has been utilized for several applications as shown in Figure 1.1. Generally, the SERS effect is described in terms of chemical and electromagnetic enhancement mechanism. The chemical enhancement is based on charge transfer between metal nanostructures and molecules absorbed on the metal surface while the electromagnetic enhancement is originated from the excitation of localized surface plasmons (LSP) on metal surfaces resulting in a largely enhanced Raman signal.

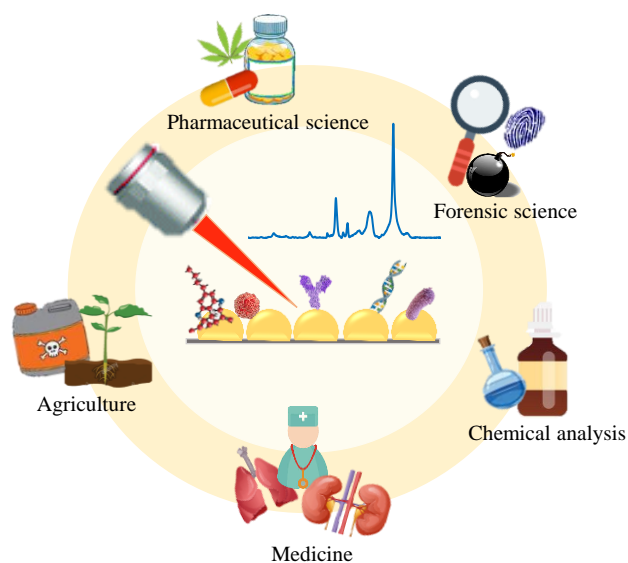
Normally, strong SERS activity is generated from the localized specific regions, also known as hotspots. The plasmonic of hotspots depends on various parameters including metal type, size, morphology, configuration, surface roughness, porosity, gaps and sharp edges of metal nanostructures (Asiala & Schultz, 2011; Tian et al., 2014). Plasmonic noble metals, especially silver (Ag) and gold (Au), are most popular metals for SERS substrates due to their attractive surface plasmon resonance (SPR) characteristics. These two metals produce plasmonic resonance ranging from the visible to the near-infrared wavelength regions, which are conventionally used for Raman measurement.

In terms of the plasmonic properties, Ag exhibits the highest SERS enhancement capabilities. However, prone to oxidation is the main drawback of Ag as it results in a decrease in SERS signal. Meanwhile, Au has a lower SERS performance than Ag, but it exhibits a high chemical stability and biocompatibility. A combination of the fascinating properties of these two metals; forming of Au-Ag bimetallic structures has been extensively studied for SERS active substrates due to their synergistic effects (Alvarez-Puebla et al., 2009; Cui et al., 2006; Gómez-Graña et al., 2013; Olea-Mejía et al., 2015). This bimetallic nanostructure has the potential to produce superior properties in terms of both sensitivity and stability of SERS substrates. Therefore,

most of the active research for SERS substrate fabrication focuses to create Au-Ag bimetallic nanostructures with improved both SERS sensitivity and stability. Moreover, they attempt to design the nanostructure in which promote more hotspots areas by controlling the fabricated structure by different techniques.

Figure 1.1

Applications of SERS Technique in Various Fields.



1.2 Statement of the Problem

The fabrication of Au-Ag bimetallic substrates has been successfully employed by several techniques, for instance, co-reduction, laser ablation and galvanic replacement. Among these methods, galvanic replacement is commonly used to create hollow bimetallic nanostructures. The driving force of the reaction is based on the difference in reduction potential of the two metals. Such nanostructures provide a high surface-to-volume ratio and enhance their plasmonic properties. The morphology and composition of these nanostructures can be controlled by reaction temperature and concentration (Chee et al., 2017; Chen et al., 2006; Kim et al., 2008; Sun & Xia, 2004). The method is preferable because of its capability to produce tunable surface plasmon resonance, cost-effectiveness, and simple fabrication procedure. However, low reproducibility is the major drawback of the galvanic

replacement technique as the nanoparticles (NPs) are randomly deposited on substrate.

To overcome this problem, other techniques which can control either geometrical shapes or periodic structure have been introduced to fabricate a good uniform nanostructure array, for instance, electron beam lithography, interference lithography, focused ion-beam lithography, and template-based electrodeposition. These processes provide high resolution periodic nanopatterns in various structures including triangular nanoprisms, nanodots, nanopillars and square arrays (Le Ru et al., 2008; L. Liu et al., 2017; L. Petti et al., 2016). Nevertheless, these techniques are slow in terms of production and involve complex processes that increase the cost of production. Sputtering is another technique that can be used to fabricate a variety of nanostructures thin films. The controllable structures can be adjusted by sputtering parameters. However, it is considered as a high-cost technique as it requires a vacuum system. This limitation could be compensated by enabling large-scale production. The cost will be cheaper when the fabrication per batch is larger.

Another method to increase SERS sensitivity is the dealloying method. The dealloying is a process to fabricate a nanoporous structure. It is known that a SERS substrate with nanoporous structure exhibits large surface areas. This has advantages due to providing high-density plasmonic hotspots and high absorbability of target molecules. Wet chemical dealloying is one of the conventional methods to create such structures (Adrien Chauvin, Willigis Txia Cha Heu, et al., 2016; Chen-Wiegart et al., 2013). It involves a selective dissolution of one metal from alloy by corrosion process. Thus, the SERS substrates fabrication based on two these methods can create both controllable structure and surface roughness. The desired substrates improve the SERS sensitivity, stability and high throughput production.

1.3 Objectives of the Study

The overall objective of this research is to explore the fabrication process of Au-Ag dealloyed SERS substrates using co-sputtering method followed by chemical etching to achieve high sensitivity and stability.

Following are the specific objectives for this research work:

1. To fabricate SERS substrates by synthesizing Au-Ag bimetallic alloyed nanorod arrays using galvanic replacement and DC magnetron co-sputtering techniques.
2. To produce dealloyed Au-Ag nanorod arrays with enhanced roughness by selectively etching Ag from the Au-Ag alloyed nanorods and study their morphological, optical, and chemical properties.
3. To investigate sensitivity and stability of the fabricated Au-Ag dealloyed SERS substrates using 4-mercaptobenzoic acid (4-MBA) as Raman probe molecule.
4. To apply the Au-Ag dealloyed SERS substrates for the urinary crystal detection including calcium oxalate monohydrate, calcium phosphate and uric acid and demonstrate as a model application for the developed SERS substrates.

1.4 Scope of the Study

This research focuses on the development of Au-Ag SERS substrates using sputtering techniques followed by the dealloying process. For the Au-Ag preparation, it can be divided into 2 different methods which are sputtering of Ag film followed by galvanic replacement to form Au-Ag structure. The second is to fabricate Au-Ag film based on co-sputtering technique.

In the first method, we study the parameters that affect a formation of Au-Ag structure including gold chloride concentration and reaction time. For the co-sputtering, parameters focus on the different sputtering power. That is a key factor to desire metal composition. After complete Au-Ag fabrication, the dealloying process is then carried out by wet-chemical dealloying, which studies both acid and base etchants, as well as their concentrations and etching time. When the structure is optimized, SERS properties were tested by studying the Raman signal amplification with standard 4-MBA substances and its stability over periods of time.

In the last part, we focus on an application of the SERS substrate. That use to measure the SERS signal of nanocrystals related to kidney stone formation: calcium oxalate monohydrate, calcium phosphate and uric acid. Finally, to demonstrate an ability of the SERS substrate to detect uric acid in artificial urine.

1.5 Organization of the Study

This study is divided into five chapters which are included as follows:

Chapter I describes the general background, statement of the problems, objectives, scope and organization of the study.

Chapter II presents reviews of literature including general information related to the study and the state-of-the-art in SERS technique.

Chapter III provides the research methodology used to achieve the specific objectives of the study.

Chapter IV presents the results obtained from the experiments and discuss them.

Chapter V summarizes the research work performed. It develops a clear view about the study in the form of conclusions and future recommendations.

CHAPTER 2

LITERATURE REVIEW

2.1 Raman Spectroscopy

Raman spectroscopy is a technique used to identify fingerprints of molecules. It is based on the inelastic interaction of light and molecular bond vibration leading to Raman scattering. Raman spectroscopy is known as a non-destructive chemical analysis technique, having advantages such as no sample preparation, rapid detection, and measurement in aqueous environment. It also can be used for qualitative and quantitative analysis. Thus, the technique has been attractive in a wide range of applications such as medicine, agriculture, forensic and material science. Raman scattering is typically a weak signal typically generated by one photon in 10^8 photons of incident light. The sensitivity is therefore limited when low concentration detection is desired. To address this, the Surface-enhanced Raman scattering (SERS) technique is used where the signal enhancement is achieved by commonly using a metal nanostructured substrate.

Raman effect is caused by the electron distortion resulting from the interaction of electromagnetic waves with electron clouds of molecules. The electron distortion is defined as polarizability which instantaneously generates the charge separation in molecule forming induced dipole moment. The dipole moment oscillation at different frequencies induces Raman scattering mode. Typically, Raman scattering is an inelastic process involving the excitation of molecules by the incident photons, from ground state to the excited vibrational and rotational state. The excited molecules move to an intermediate state which is commonly called a virtual state. The virtual state is not stable, so the molecules immediately move down to the new energy state causing photons scattering. The photons scattering can be divided into three phenomena based on the energy change in initial and final electronic state of molecule transition. First, the dominant process, the energy of the molecule has no change when interacting with the photon. Thus, the energy and also wavelength of scattered photons is equal to the excited photon: called Rayleigh scattering or elastic scattering.

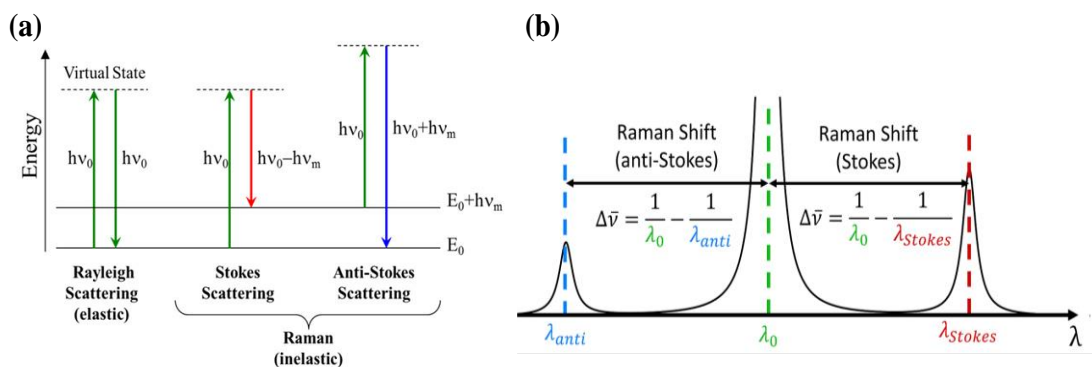
Second phenomenon, the anti-Stokes Raman scattering, occurs when the scattered photons exhibit a higher energy or higher frequency than the incident photon. Inversely, the last phenomenon, in which the scattered photons lose energy during scattering is called Stokes Raman scattering. Normally, molecules prefer to populate at the ground vibrational state resulting in a higher probability in Stokes Raman scattering process. As such, the signal of Stokes Raman scattering is regularly more intense than that of the anti-Stokes scattering. The diagram of photons scattering is shown in Figure 2.1. Typically, Raman spectra are reported in Raman shift or wavenumber. This is because the scattering wavelength depends on the excitation wavelength leading to the incomparable spectra when excitation with a different wavelength source. Thus, Raman scattering wavelength is converted to Raman shift; which is a wavelength shift away from the excitation wavelength. This value is directly related to the energy and can be calculated by the following formula.

$$\Delta\bar{\nu}(\text{cm}^{-1}) = \left(\frac{1}{\lambda_0(\text{nm})} - \frac{1}{\lambda_s(\text{nm})} \right) \times \frac{(10^7 \text{ nm})}{\text{cm}} \dots\dots\dots (2.1)$$

where $\Delta\bar{\nu}$ is the Raman shift expressed in wavenumber (cm^{-1}), λ_0 is the excitation wavelength (nm), and λ_s is the Raman scattering wavelength (nm).

Figure 2.1

(a) The Schematic Diagram of Photon Scattering With Elastic and Inelastic Scattering. (b) Raman Shift of Stoke and Anti-Stoke Scattering.



Note. Rayleigh scattering, energy is the same as incident light ($h\nu_0$) (no change in frequency and wavelength). Stokes Raman scattering is when a molecule absorbs energy, and a scattered photon has a lower energy (longer wavelength) than incident light ($h\nu_0 - h\nu_m$). Anti-stokes Raman scattering is when a molecule loses energy, and scattered photons have a higher energy (shorter wavelength) compared to incident light ($h\nu_0 + h\nu_m$) (Butler et al., 2016)

It is well known that most common light scattering is Rayleigh scattering. Raman scattering is very weak, only one photon in 10^8 photons of incident light. Therefore, the Raman signal needs to be distinguished from the Rayleigh scattering signal in a measurement. Raman spectroscopy is a sensitive technique which can reduce Rayleigh scattering and provide a clear Raman signal (Bumrah & Sharma, 2016). Raman spectroscopy can identify molecular fingerprints corresponding to the vibration, rotation and other low-frequency transitions of a molecule.

The instrument system consists of six main components including laser light source, focusing and collecting sample illumination lenses, filter, grating, CCD detector and recording device. The laser wavelength is usually in the near ultraviolet (300-400 nm), visible (400-700 nm) and the near-infrared (750-1400 nm) range. With the aid of lenses, a laser beam is focused onto the sample and the scattered photons are collected. A filter is used to separate the inelastically scattered light by blocking the Rayleigh scattering. These Raman scattering photons were sent to a monochromator and then grating. Grating will split Raman scattering into its constituent wavelength, and the signal is collected by CCD detector (Butler et al., 2016).

Owing to its high sensitivity and specificity, Raman spectroscopy has become a useful analytical method for many application fields such as organic, inorganic and biological detection. It can be used for both qualitative and quantitative detection and provides the results within a short time. Moreover, sample preparation is not required, and a vacuum system is also no needed. The measurement can be done in solid samples, gases and aqueous solution. However, an important problem of Raman spectroscopy is fluorescence interference which is originated from an analytical compound or the fluorescent impurities in samples. The fluorescence signal is more intense than Raman signal resulting in the hiding of Raman information. Thus, the approach to reduce fluorescence interference is to illuminate the samples with a near-

infrared laser. Operating at a longer wavelength could certainly result in fluorescence background reduction yet the Raman intensity is also lower compared to the excitation by a shorter wavelength. This is because Raman scattering intensity is inversely proportional to the fourth order of the excitation wavelength.

2.2 Surface-Enhanced Raman Scattering (SERS)

Surface-enhanced Raman scattering is a sensitive vibrational technique that enhances Raman scattering of molecules typically adsorbed on or nearby a plasmonic metal surface. The phenomenon was discovered by M. Fleischmann, P. J. Hendra, and A. J. McQuillan in 1974. They observed a large Raman signal of pyridine adsorbed on a roughened Ag electrode of an electrochemical cell. (Fleischmann et al., 1974). Later in 1977, David L. Jeanmaire and M. Grant Albrecht, two independence research groups reported the enhancement Raman scattering of pyridine which generated from surface plasmon resonance effect and the intensity enhancement was around 10^5 (Albrecht & Creighton, 1977; Jeanmaire & Van Duyne, 1977). In 1978, M. Moskovits suggested that the signal enhancement of a molecule adsorbed on metal electrodes surface is arisen from preresonant or resonant excitations of conduction electron resonances (Moskovits, 1978). This phenomenon is subsequently called surface-enhanced Raman scattering. From then on, SERS has been extensively studied in many research groups, owing to the combination of high sensitivity from SERS and the intrinsic advantages of Raman spectroscopy.

There are several study aspects of SERS, starting from the explanation of its fundamental mechanisms and extending to its possible applications. Another key aspect of most active SERS research is the fabrication of SERS substrates with an optimum SERS response. This can be obtained at the hotspot regions where the electric field enhancement occurs. Generally, hotspots are produced from nanogaps between the plasmonic nanoparticles, especially in a range of 2-10 nm. The electromagnetic field amplification could also be generated from the other geometries of plasmonic nanostructures such as the interparticle junctions, sharp edges, crevices, and roughness.

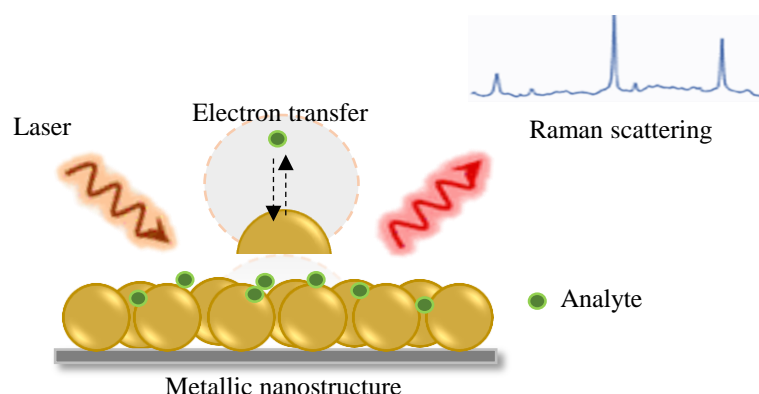
2.2.1 SERS Mechanisms

In general, it is well known that SERS is observed when molecules are absorbed on the metallic nanostructures. Raman signal is amplified by the electromagnetic enhancement through the excitation of localized surface plasmon resonance on the metal surface. However, the SERS mechanism is not exactly clear. After decades of debate, there are two dominant theories which are generally accepted to explain the SERS phenomena: chemical and electromagnetic mechanisms enhancement.

2.2.1.1 Chemical Enhancement. Chemical mechanism (CM) enhancement is associated with charge transfer between the analyte and substrate. The mechanism can be described when molecules bound to the metal surface via chemisorption form a charge-transfer complex. The electrons of molecules interact with metal electrons to form chemical bonding. As shown in Figure 2.2, when the incident light hits the metal surface, the excitation energy is transferred to the adsorbed molecules via the specific functional groups and thus causing Raman scattering. The enhancement factor of this chemical mechanism is calculated to be only 10^1 - 10^3 . Moreover, chemical enhancement mechanism can be described only through chemisorption and depends on the type of molecules. However, it does not consider the other kind of interaction, such as physisorption or physical adsorption (Ouyang et al., 2017).

Figure 2.2

SERS Chemical Enhancement



2.2.1.2 Electromagnetic Enhancement. Electromagnetic mechanism (EM) enhancement is due to a local electromagnetic field enhancement mechanism. The EM can be divided into two steps. First, when an incident electromagnetic field (E_0)

interacts with an electron cloud on metal surfaces, it will excite localized surface plasmon or electron oscillation on the surface. The plasmon oscillation induces charge separation forming oscillating dipole, which is described in the formula:

$$\mu = \alpha E \dots\dots\dots(2.2)$$

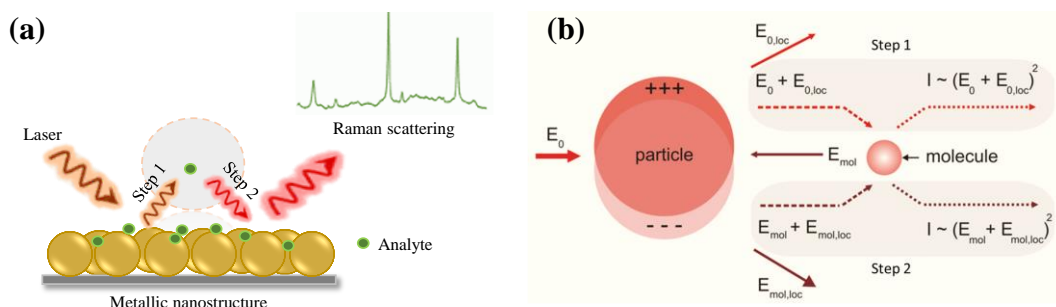
where μ is dipole moment, α is polarizability and E is electromagnetic field, respectively.

The induced polarization generates a large amount of electromagnetic field at this local area ($E_{0, loc}$) yielding the total incident field, $E_0+E_{0, loc}$. The plasmon energy is transferred to the molecule adsorbed on the metal surface, subsequently causing an increased Raman intensity (I), $I \sim (E_0+E_{0, loc})^2$. On a second step, the emitted Raman field from the molecule (E_{mol}) is also enhanced by localized surface plasmon oscillation of the particle ($E_{mol}+E_{mol, loc}$). Consequently, the resultant Raman intensity increase is equal to $(E_{mol}+E_{mol, loc})^2$. Therefore, in most circumstances, the Raman intensity enhancement can be approximately expressed by the magnitude of the localized electromagnetic field to the power of four (E^4), as shown in Figure 2.3 (Jensen et al., 2008).

Figure 2.3

(a) Schematic Representation of SERS Electromagnetic Enhancement Mechanism.

(b) The Electromagnetic Enhancement Mechanism Steps.



Note. The mechanism represents into two steps. First, the Raman enhancement of molecules is due to electromagnetic field enhancement of incident light by induced polarization of metal particles. Second, the emitted field of a molecule is enhanced by the same of the first process. In each step, the Raman intensity is enhanced by E^2 thus leading to a total enhancement of E^4 (Jensen et al., 2008).

The enhancement factor of EM can achieve up to 10^{11} , depending on the nanostructure of plasmonic materials and orientation of molecules on the surface. This is a very large number compared to the chemical enhancement.

2.3 Alloy SERS Substrates Fabrication

Numerous research have been carried out to fabricate SERS substrates with controllable nanostructures, good reproducibility, chemical stability, low fabrication cost and high sensitivity. Traditionally, SERS substrates compose of pure plasmonic materials, especially, Ag, Au and Cu. In general, Ag and Au are mainly used due to their outstanding plasmonic properties. Ag has a high SERS performance because of its strong interparticular near field coupling effect and sharp plasmonic peak. However, the main drawback of Ag is its oxidation in ambient conditions and also Ag has less chemical stability compared to Au. Au, on the other hand, produces less SERS enhancement compared to Ag despite its higher stability. Therefore, the combination between these two materials with extraordinary plasmonic properties, forming of Au-Ag bimetallic or alloy substrates has attracted the interest in SERS substrate development.

In the following section, we mainly focus on the metallic alloy SERS substrates fabrication processes especially Au-Ag. Typically, the alloy SERS substrate fabrication can be obtained using three approaches: (1) colloid or nanoparticles in suspension; (2) immobilization on solid substrate; and (3) nanopattern array on planar substrate (Fan et al., 2011). The common difficulty of these techniques is about the randomness in forming nanostructures resulting in large variations in SERS substrate. Here, we describe these three fabrication methods as well as their advantages and disadvantages.

2.3.1 Nanoparticles in Suspension

2.3.1.1 Chemical Reduction. The synthesis of bimetallic nanoparticles in suspension have been widely used in many studies as SERS substrates because of its simple process, facile surface conjugation, biocompatibility, and large-scale production. It is a wet chemical method based on seed mediated growth in chemical reduction. The Au-Ag bimetallic nanoparticles prepared by co-reduction of Au and Ag precursor in a solution with a reducing agent such as disodium citrate, sodium borohydride, ascorbic acid and hydrazine hydrate. This method can provide surface plasmonic resonance in visible and near-infrared regions depending on the size, shape and composition of the synthesized particles (Link et al., 1999). A diverse pattern of Au-Ag nanoparticles synthesized via the co-reduction method have been reported, including core-shell nanoparticles, flower-like 3D, nanocages, nanostar and nanodisks (Garcia-Leis et al., 2015; Y. Huang et al., 2019; Krishnan et al., 2018; Zhang et al., 2018).

Still, the co-reduction method has some problems because of the signal variation in nanoparticles suspension owing to Brownian motion effect (Aroca et al., 2005). In addition, the size variation and the aggregation also affect the scattering signal because of the randomly distributed hot spots in nanoparticle junctions (Cui et al., 2006; Flegler & Rosenbluh, 2009). This leads to a low reproducibility of SERS activity. However, some studies have reported that the aggregation of the metal nanoparticles provides a significant SERS enhancement, due to EF generated at junction site between adjacent particles (Budnyk et al., 2010; Çulha et al., 2008; Schwartzberg et al., 2004).

2.3.1.2 Pulsed Laser Ablation. Apart from chemical synthesis, another simple method used for Au-Ag alloy NPs fabrication is pulsed laser ablation (PLAL). The method is implemented with a continuous pulsed laser beam. The laser beam is focused on the bulk metal surface to ablate the metal particles into liquid form. The ablated particles interact with molecules in solution to initiate nucleation process, growth and finally nanoparticles formation. PLAL is a very clean, fast, and simple physical method. In addition, it can synthesize the alloy and colloidal suspension with a high purity. The structure, composition and properties of the obtained nanoparticles can be controlled by laser parameters, ablation time, metal targets and pH solution (Herrera et al., 2013; H. Huang et al., 2019; Vinod & Gopchandran, 2015a, 2015b). However, the fabricated samples have a very broad variation and contains not only spherical particles but also some sintered structures (Binh & Dong, 2015; Olea-Mejía et al., 2015; Peng et al., 2006; Vinod & Gopchandran, 2014).

2.3.2 Nanoparticles Immobilization on Substrate

One approach to overcome the random distribution or aggregation is to immobilize nanoparticles on the substrate. The immobilization process usually deposits colloidal nanoparticles onto a substrate by self-assembly process or using chemical functional groups. This brings nanoparticles to a close proximity of the adjacent molecules. Nanoparticles are easily transferred to the supporting substrate by dropping or immersing the substrate into colloidal solution. The substrate could be either solid or flexible supports such as glass, silicon, polymer, and paper (Fortuni et al., 2017; He et al., 2017). This synthesis method can generate a uniform or homogeneous nanoparticles layer on the surface substrates. However, the nanoparticles are still not precisely arranged in ordered structure. The difference in molecular orientation and impurities also induces the signal variations. Moreover, the transferring process has an effect on the stability and adhesion of nanoparticles onto the substrates (Fan et al., 2011; Ouyang et al., 2016).

2.3.2.1 Direct Self-Assembly Process. Self-assembly is a process which constructs spontaneously organized ordered nanostructures from individual nanoparticles building blocks. The self-assembly process is driven by the solvent evaporation and capillary forces which promote packing of adjacent nanoparticles. This renders to generate a high dense intermetallic nanogaps resulting in large effective hotspots. This is a promising method for SERS substrate fabrication

because of low cost, large-scale production, stable structure and uniformity. For example, Gómez-Graña et.al. have reported the fabrication of core-shell Au@Ag nanorods as SERS-active 3D supercrystals by self-assembly process. The Au@Ag nanorods are stabilized with a gemini surfactant by seeded growth method. The synthesized Au@Ag nanorods were then dispersed on ITO-coated glass slide by drop casting. The spontaneous assembly of the nanoparticles on the substrate is controlled by temperature and humidity. The fabricated Au@Ag nanorods is recognized as a good SERS substrate because it has a higher EF than their Au nanorods counterpart and enables large-scale detection (Gómez-Graña et al., 2013).

2.3.2.2 Chemically Modified Substrate. Chemical modification is also one of the methods to functionalize substrates. The metal nanoparticles attach to the surface of a substrate via functional groups of the chemical such as silane coupling agents, polyethylene glycol and thiol group (Bibikova et al., 2017; Caro et al., 2018; Péron et al., 2009). Unlike the self-assembly process, the functional groups render a specific assembled nanostructure on the substrate. Various nanostructures can be fabricated by this technique as there is a diversity of chemical functionalities such as length chains, functional groups, hydrophobic and hydrophilic properties. SERS substrate fabricated by this method can control the packing density of metals and exhibits a good homogeneity (Ouyang et al., 2016). However, the modification with functional groups can interfere with the binding between the target molecule and the SERS substrate, leading to a degraded SERS effect.

Previous work reported AuNPs deposited on polyvinylpyrrolidone (PVP) immobilized on gold electrode as SERS substrate. The AuNPs dispersed on the surface with a uniform submonolayer coverage on the surface. This kind of structure leads to a stronger SERS effect due to the particle-particle and particle-substrate plasmonic coupling. Moreover, they also conclude that SERS effect obtained from a multilayer adsorption is higher than that of monolayer (Cheng et al., 2009). Yang et al. also reported the synthesization of the Au@Ag, Ag@Au core-shell bimetallic nanoparticles by seeding growth method. The nanoparticles were immersed on (3-Aminopropyl) trimethoxysilane (APTMS) - modified glass slides forming a monolayer film via self-assembly process. The Au@Ag and Ag@Au composite nanoparticles showed a good uniformity on glass substrate. For SERS performance,

the Au@Ag substrate provided the highest SERS spectrum of Rhodamine 6G (R6G) than monometallic Ag, Au and Ag@Au substrates (Yang et al., 2008).

2.3.3 Nanopattern Arrays on Planar Substrate

Nanopattern arrays involve a construction based on directly deposited nanostructures on substrate. The nanopattern arrays certainly manipulate LSPR by adjusting size, morphology, periodicity, spacing, dielectric environment and even a distribution of hotspots. The nanopattern arrays can be produced in various controllable structures including nanosphere, nanopillars, nanotriangles, nanotubes and nanocaps (Lai et al., 2018; Li et al., 2008; Lin et al., 2010; Yan et al., 2014; Zhao et al., 2017). Due to a high structural controllability, this fabrication technique has the advantages in terms of reproducibility, uniformity and sensitivity. The nanostructure fabricated by this technique serves an excellent system for SERS simulation modeling. Various techniques have been reported to fabricate the alloy nanopattern arrays SERS substrates, for instance, template-based synthesis, lithography-based method and sputtering.

2.3.3.1 Template based electrodeposition. Template-based electrodeposition is a useful method for nanowire preparation. The technique is low cost, easy and uses only simple equipment. This technique can produce uniform nanowires with a large range of diameter, from several nanometers to a few hundred nanometers. There are many types of templates including polycarbonate membranes, mesoporous oxide and anodic aluminum oxide (AAO) templates. Among these templates, AAO is the most commonly used as SERS substrate because it can control both diameter and length of nanowires by varying the anodizing conditions, along with its good mechanical strength and stable structure.

Weon-Sik Chae et.al. synthesized Au-Ag alloy nanowires by AAO template and selective etching in concentrated nitric acid. After the etching process, the Au-Ag alloy structure turned into the porous nanowires. The resulting SERS spectra of crystal violet indicated that the porous alloy nanowire provided a higher EF in the order of 10^6 than that of a solid Au nanowire (Chae, 2011). A recent study reported a synthesis of porous Au-Ag nanowires by template-based electrochemical deposition and following by dealloying process. Au-Ag alloy nanowires were fabricated by co-electrodeposition using AAO as a template and 15% HNO₃ solution as an etching reagent. The fabricated SERS substrate provided a Raman spectrum of

4-MBA with EF of 5×10^6 . Moreover, the stability of this substrate was determined for 90 days. The result showed that SERS signal of 4-MBA was stable within 35 days (100% of initial signal) and the signal was decreased to 40-45% on the 90th day (Wiriyakun et al., 2016).

After all, the template-based synthesis has some drawbacks. After the etching process, the AAO templates need to be removed using an acidic or alkaline solution leading to the concern in the purity of the nanowires. Moreover, the technique is time consuming as it involves sputtering a metal layer onto the AAO template as a conductive layer of working electrode. Finally, the handling of fragile AAO template during the process is difficult and this could affect the SERS performance and reproducibility (Ali & Maqbool, 2013).

2.3.3.2 Lithography-Based Methods. Lithography is a process to fabricate a precise nano- or micro-scale patterns on solid substrates. The procedure also can create 2D or 3D complex structures with a high precision and repeatability. This technique has been extensively used on fabricating SERS substrates because it can fabricate the desirable and highly homogenous patterns. The fabricated nanopattern arrays could certainly generate a large number of hotspots owing to the narrow gaps between the patterned arrays. Many lithography methods have been used for SERS substrates fabrication such as electron beam lithography (EBL), focused ion beam lithography, nanosphere lithography, Laser interference lithography (LIL), nanoimprint lithography (Gisbert Quilis et al., 2018; Petti et al., 2016; Sivashanmugan et al., 2013; Zhao et al., 2017).

A previous study reported the fabrication of SERS substrate with well-ordered Au-Ag multilayered nanorod arrays using the focused ion beam technique for the detection of the influenza A virus strain. Corresponding to the virus detection, the fabricated substrate showed a good performance with EF order of 10^6 - 10^7 for R6G and low concentration of 10^6 PFU/ml (Sivashanmugan et al., 2013).

Recently, there has been a demonstration of aggregated AuNPs array based on LIL and electrodeposition. The substrates produced a sensitive, reproducible SERS signal, which can detect R6G at a concentration of as low as 10^{-8} M, with EF of 1.25×10^5 (Hwang & Yang, 2018). Furthermore, this approach is able to control nanostructures in a periodic geometry matching with a desirable wavelength. The

periodic structure provides a good system for simulation giving a further understanding of the SERS mechanism. However, its main disadvantages are high cost, time consuming, complex operation process, needs professional training for fabrication and low production scale.

2.3.3.3 DC Magnetron Sputtering. Sputtering is a physical vapor deposition (PVD) technique for thin film fabrication. The deposition of the ejected atoms or molecules onto a surface substrate is achieved by the bombardment of source material by the high energy particles in a high vacuum system. It has been widely used in various research and industrial applications, starting from the simple design coating fabrication until the complex microelectronics fabrication. The properties of the fabricated thin film can be controlled by the sputtering conditions such as pressure, bias voltage, target current, target-substrate distance and deposition time. The sputtering system can be equipped with various sputter deposition sources including direct current (DC), Radio Frequency (RF) and pulsed DC power supplies. Among these, DC power is generally applied for conductive materials especially metals and metal oxide thin films.

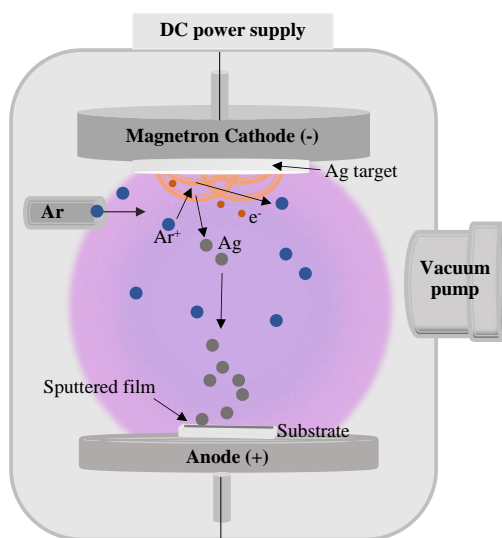
The sputtering process occurs when an inert gas such as argon (Ar) or nitrogen (N₂) is introduced into a vacuum chamber with a constant flow rate and pressure. The DC power applies a constant voltage between target metal and substrate which ionizes Ar gas molecules and generates plasma. The ionized Ar ions are then accelerated to bombard the target source at cathode with sufficient kinetic energy. The target atoms are ejected due to the powerful collision. These atoms travel to the substrate at anode and condense into a film. By maintaining the Ar ionization in a continuous cycle, numerous Ar ions and electrons could be generated, and thus forming a dense and homogenous film.

The magnetron sputtering system has emerged in order to improve a sputtering rate. Magnetron sputtering is a high-rate vacuum coating for metals, alloy and other compound deposition by adding a strong magnetic field near a cathode target of a conventional sputtering system. The magnetic field causes a spiral electron travelling path along the magnetic flux, instead of moving toward an anode substrate. This change in electron travelling path prevents the electrons from damaging a deposited film. Besides, it also confines plasma close to the surface of the sputter target. The

plasma confinement will generate more Ar ions resulting in more ejected target molecules, leading to a high deposition rate and high film purity. The DC magnetron sputtering system is shown in Figure 2.4.

Figure 2.4

DC Magnetron Sputtering System.



The sputtering deposition is able to fabricate the single or multilayer metal coating with high uniformity, density and purity. Moreover, it can sputter the materials with a high melting point and also controls the stoichiometry of the films. The deposition of the multicomponent films, such as metal alloy, can be achieved by a co-sputtering system. The co-sputtering system has two separate metal targets and normally two cathodes. The sputter deposition sources can be independently controlled to adjust their respective sputtering power, time and sequence. Thus, it is capable of fabricating the desired multicomponent film with unique properties. The SERS structure fabricated by the sputtering process is highly controllable in size, shape and metal composition. Moreover, it is an effective SERS substrate fabrication technique as it provides a high purity, uniformity, reproducibility and enables large scale production. However, its fabrication cost is high as it operates in a vacuum system. Nevertheless, this could be compensated for by a large-scale production. The previous reports based on sputtering technique for alloy nanopattern arrays fabrication as the SERS substrate are summarized and their structures are depicted in

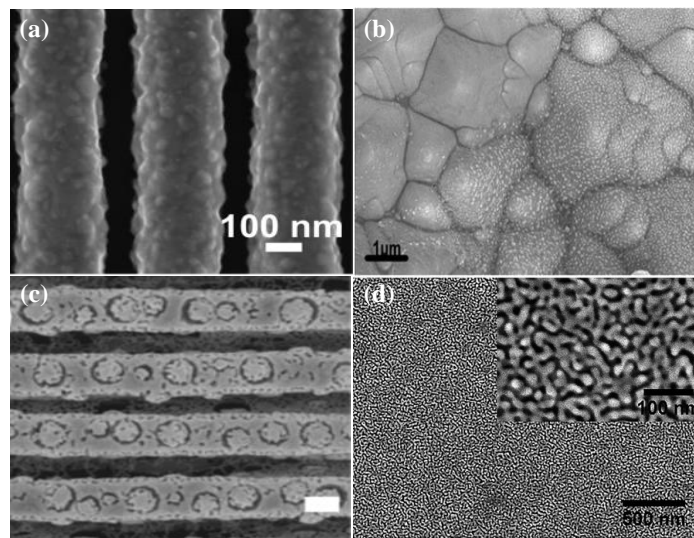
Figure 2.5. It has been demonstrated that the magnetron co-sputtering could fabricate highly ordered porous nanowire arrays up to a few centimeters long.

The Au-Ag alloy nanowires were first synthesized by sputtering targets onto a nanograted silicon substrate. The process was followed by electrochemical dealloying in diluted sulfuric acid to form a nanoporous alloy structure as shown in Figure 2.5 (a) (Chauvin et al., 2017). Zhang, C et al. presented a preparation of Au@Ag/3D-Si substrate with a high reproducibility and sensitivity. First, a 3D-Si substrate was fabricated by a wet-texturing process to form a pyramidal structure. The Ag atoms were then deposited on 3D-Si by thermal evaporation to form Ag-3D-Si. Finally, Au atoms were coated on Ag-3D-Si to form Au-Ag alloy by ions sputtering technique (Figure 2.5 (b)). Raman spectra of R6G were observed and EF was calculated to be 1.2×10^9 (Zhang et al., 2016).

Adrien Chauvin and co-workers reported the porous Au-Cu alloy nanowires that could be potential for SERS substrate. Firstly, a nanograted silicon template was fabricated by laser interference lithography and deep reactive ion etching to create some defects on the substrate. Then, Au-Cu nanowires with a nodular morphology hillock were deposited on the silicon substrate by DC co-sputtering. Au-Cu alloy nanowire was then dealloyed by an electrochemical process to create ring-shaped nanopores (Figure 2.5 (c)) (A. Chauvin et al., 2016). A recent report of Jinglin Huang and co-workers presented a fabrication of gradient nanoporous Au-Ag alloy. The Au-Ag alloy film was first created on silicon substrate by co-sputtering technique with various ratios of the metals and followed by dealloying the substrate with 70% HNO₃ for 5 minutes. The dealloying process created a gradient 3D nanostructure with EF over 10^7 (Huang et al., 2017) as shown in Figure 2.5 (d).

Figure 2.5

(a) SEM Image of Au-Ag Nanowire Based on LIL and Sputtering Deposition (Chauvin et al., 2017). (b) Au@Ag/Pyramidal Silicon 3D Structure Fabricated by a Wet Texturing Process Incorporated With Sputtering (Zhang et al., 2016). (c) Au-Cu Nanowires by LIL and Sputtering After Electrochemically Dealloying (A. Chauvin et al., 2016). (d) Gradient Nanoporous Gold Fabricated by Magnetron Sputtering and Dealloying Technique (Huang et al., 2017).



2.3.3.4 Glancing-Angle Deposition (GLAD). GLAD is a thin film physical vapor deposition technique based on oblique angle deposition (OAD) and substrate rotation. It is a tool emerged for an ordered arrays nanostructure fabrication including nanopillars, zigzag, helical, spirals and columnar structures (Barranco et al., 2016; Jen et al., 2015; Liu et al., 2010; Shuang et al., 2016; Zhou et al., 2012). The basic principle of GLAD is described as follows: the flowing target atoms collide with a substrate resulting in a condensation of adatoms on the substrate. The condensed adatoms create the separated individual islands or nuclei deposited on the substrate. Because of the tilted substrate, incident flux arrives at the substrate with respect to oblique angle, thereby leading a shadowing effect (Figure 2.6). The shadowing effect is the main mechanism to prevent incident vapor coming into an area behind the nuclei. During the deposition process, condensing vapor and shadowing effect cause the self-assembly growth of adatoms at nuclei region forming columnar structure. The controlled substrate rotation is also resulting in a change of incoming vapor and

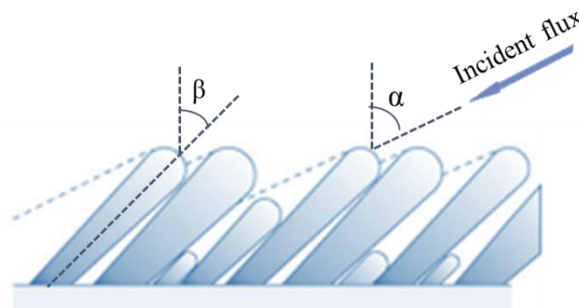
column growth. The column angle of nanostructure is depended on many factors: material, flux energy, film temperature and incident angle of vapor (Daza et al., 2017; Lau et al., 2013; Robbie et al., 1998). An empirical rule has been proposed to describe a relationship between column angle (β) and vapor incident angle (α);

$$\tan \beta = \frac{1}{2} \tan \alpha ; (\alpha < 60^\circ) \dots \dots \dots (2.3)$$

$$\beta = \alpha - \arcsin \frac{(1 - \cos \alpha)}{2}; (\alpha > 60^\circ) \dots \dots \dots (2.4)$$

Figure 2.6

Schematic of Glancing Deposition Technique.



Note. The columnar structure grows on the substrate corresponding to vapor incident angle or flux angle (α) and column angle (β). Both angles are measured with respect to the substrate normal (Robbie et al., 1998).

Ag nanorods arrays fabricated by GLAD technique are considered as good SERS substrates. Such nanostructured surfaces have been reported to detect many molecules with EF greater than 10^7 . It is widely reported that Ag nanorods SERS substrate provides a high sensitivity, reproducibility and uniformity (Nuntawong et al., 2013; Tripp et al., 2008; Wachter et al., 1992). The EF was around 10^7 - 10^8 . Moreover, the relative standard deviation of SERS signal at different detection areas and different batches was 10% and 15%, respectively (Driskell et al., 2008). Another group reported Au-modified Ag nanorod arrays as SERS substrate. Ag nanorods were fabricated by OAD using an electron-beam evaporation system. The Ag

nanorods substrate was then immersed in 1 mM chloroauric acid (HAuCl_4) solution for various reaction times of 1, 5, 10, 15, 20, 25, 30, 35, 40, and 50 minutes. With the increasing reaction time, the Ag nanorods were gradually replaced by Au, and the structure changed to form a hollow and porous shell. At the reaction time of 20 and 30 minutes, Au-modified Ag nanorod substrates showed a higher SERS signal compared with Ag nanorods substrate after 4 days exposure to ambient air (Song et al., 2012).

Apart from the sputtering methods, other methods have been also employed to fabricate nanopatterned SERS substrates. For example, the template-based electrodeposition using porous AAO membranes have been used widely. But the process requires removal of the AAO templates after the completion of the fabrication steps using acid or alkaline solutions, which add additional substrate preparation steps and increase possibilities of substrate impurities. Moreover, the process needs an additional step of sputtering metal on one side of the AAO template as a conductive layer to be able to work as the working electrode during electrodeposition. Handling of fragile AAO templates during the process is another difficulty. It, therefore, affects the reproducibility and also SERS performance (Ali & Maqbool, 2013). Lithography based techniques are also used widely that are capable of creating complex patterns with high resolution. However, it is an expensive and complex multi-patterning process with low throughput. Meanwhile, sputtering technique is also considered as a high-cost technique and consumes time, but it can be performed in large-scale for mass production of SERS substrates with good reproducibility.

The performance comparison of these three categories for alloy SERS substrate fabrication methods are summarized in Table 2.1.

Table 2.1

Comparison of Three Categories of Methods Typically Used for the Fabrication of Alloyed SERS Substrates.

Alloyed SERS substrates fabrication method	High sensitivity	Reproducibility	Large-scale	Low cost	Purity	Simple process
NPs in suspension						
Chemical reduction			✓	✓		✓
Pulsed laser ablation			✓	✓	✓	✓
NPs immobilization on substrate						
Direct self-assemble process		✓	✓	✓		✓
Chemical modification surface		✓	✓	✓		✓
Nanopattern arrays on planar substrate						
Template-based electrodeposition	✓	✓	✓		✓	
Lithography-based method	✓	✓			✓	
Sputtering	✓	✓	✓		✓	

2.3.4 Galvanic Replacement

Galvanic replacement is an effective method that has been utilized to synthesize hollow bimetallic nanostructures. This is an electroless deposition technique where the final structure could be controlled by adjusting the reaction parameters. Galvanic replacement is driven by the difference in the standard potential of the reacting metals: a less noble metal is replaced by the more noble metal. The reduced element has a higher half-cell standard potential than oxidized substrate. In the case of Au-

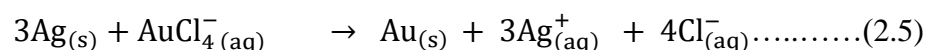
Ag alloy, the reaction spontaneously occurs as the difference in their standard reduction potential (shown in Table 2.2.)

Table 2.2

Standard Reduction Potentials for the Half-Reaction of AuCl₄⁻ and Ag

Reduction Half-Reaction	Standard Potential, E° (V versus SHE)
$\text{AuCl}_4^-_{(\text{aq})} + 3\text{e}^- \longrightarrow \text{Au}_{(\text{s})} + 4\text{Cl}^-_{(\text{aq})}$	1.002
$\text{Ag}^+_{(\text{aq})} + \text{e}^- \longrightarrow \text{Ag}_{(\text{s})}$	0.800

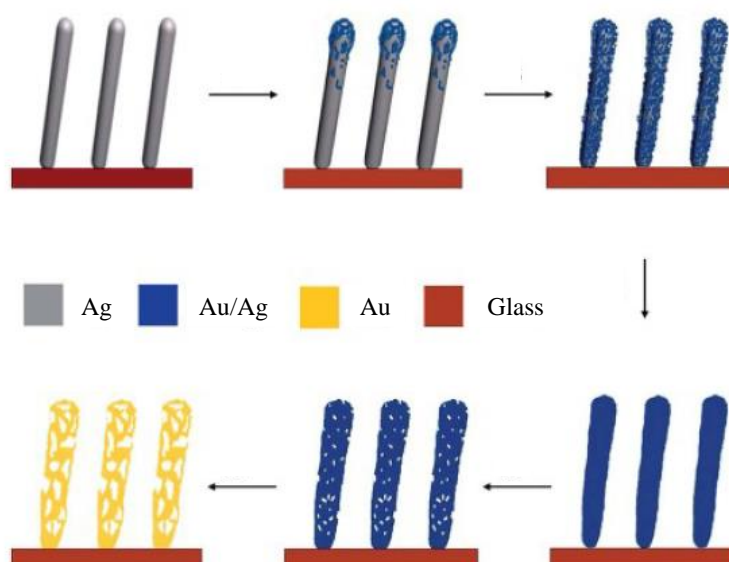
The alloying reaction happens where Au metals deposited on Ag nanostructure by using HAuCl₄ as a gold precursor. AuCl₄⁻ is reduced to Au due to the higher AuCl₄⁻/Au standard reduction potential (1.002V vs SHE). As the Ag⁺/Ag pairs have a lower potential (0.8V vs SHE); Ag is thus oxidized to Ag⁺ and eventually dissolved in solution according to equation 2.5.



Chunyuan Song et al. described a detailed reaction mechanism of Au-Ag nanorods array fabrication via galvanic replacement reaction (GRR). The reaction starts around the tip of nanorods because of the capillary effect between gold chloride solution and nanorods structure. Then, Au particles randomly nucleate and grow to form a layer of Au-Ag alloy deposited on the Ag template surface. In this step, the small pores were formed on the surface of the NR while the Ag template remained compact. Afterwards, the gold solution fully penetrates into the nano-opening pores and the reaction takes place in the whole structure of nanorods. This results in more nucleation sites for fresh Au atom deposition. The interior Ag atoms are continuously replaced, and more Au atoms deposited on the surface to form Au-Ag hollow structure. The reaction occurs continuously until the Ag structure has been completely consumed (Lu et al., 2007; Sun et al., 2002). The enlarged pore size can be obtained as the Au atoms rearrange themselves through surface diffusion into clusters (Song et al., 2012) as shown in Figure 2.7.

Figure 2.7

Schematic of Au-Ag Formation via Galvanic Replacement.



The previous reports with different shapes of Au-Ag alloy based on galvanic replacement are presented as the following. Ziren Yan and co-workers fabricated Ag-Au nanocages using electrodeposition Ag nanoparticles on indium tin oxide (ITO) substrates and subsequently galvanic replacement. The Ag nanoparticles substrates exposed into 0.1 mM HAuCl_4 solution for various times of 0.5, 1 and 2 hr. As time increased, the alloy exhibited small holes and finally formed a nanocage structure. During the dealloying process with 10% HNO_3 solution, Ag-Au nanocages were transferred to form chains (Yan et al., 2015). Besides, Gutés, A. et al. presented the synthesis of Ag dendrites pellets on aluminum foil by immersing in AgF solution. Then, the obtained Ag dendrite pellets were coated with KAuCl_4 by dipping process to form Au-coated Ag dendrites via galvanic replacement. The substrate was kept in ambient condition for more than 15 months. The Raman spectra of a 1, 2-benzenedithiol was clearly observed in Au-coated Ag dendrites with no signal degradation. In comparison with the Au-coated Ag dendrites, the Ag dendrite has a lower stability because of Ag_2O formation (Gutés et al., 2012).

Likewise, Ag@Au core-shell dendrite substrate was fabricated by hydrothermal corrosion and further galvanic replacement. To form Au monolayer on Ag substrate,

Ag dendrite was grown on Si substrate by hydrothermal etching with HF, H₂O₂ and AgNO₃ and then immersed in 1 mM HAuCl₄ solution for 60 s. The prepared substrate showed a high sensitivity, reusability and a stability of over 6 months (Jun Yin et al., 2015). Another report demonstrated a fabrication of Ag-Au nanoalloys film. Briefly, Ag film was deposited on Si/SiO_x wafers by electron beam evaporation. Ag-Au bimetallic film was then prepared by immersing the film into 1 mM of potassium gold chloride (KAuCl₄) solution with different reaction times. The result suggested that SERS effectiveness depends on the film morphology. Moreover, the plasmon resonance of SERS could be controlled and tuned by galvanic reaction time and Ag template thickness (Alvarez-Puebla et al., 2009).

Overall, galvanic replacement is a simple reaction which can be potentially used to create a hollow alloy or bimetallic nanostructure. By varying the concentration of gold chloride solution and reaction time, the metal contents of the nanostructures could be controlled and thus its morphology and LSPR band.

2.3.5 Dealloying Process

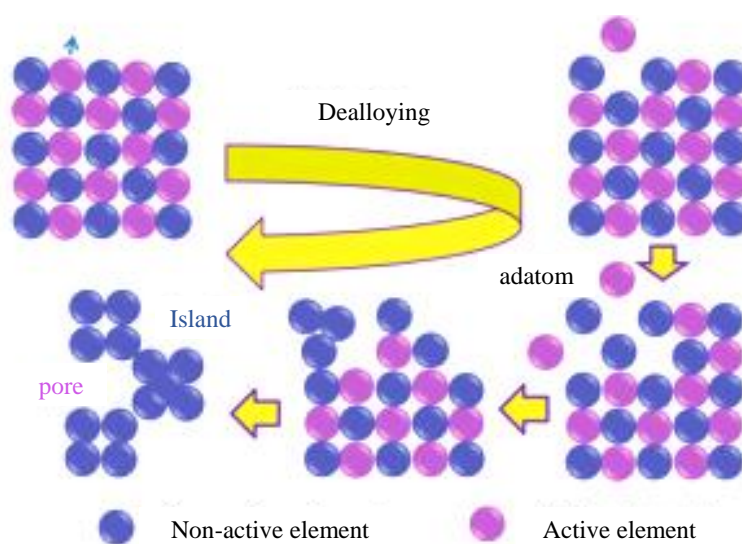
Another method to increase SERS sensitivity is the dealloying method. The dealloying is a process to fabricate a nanoporous structure. It is known that a SERS substrate with nanoporous structure exhibits large surface areas. This has advantages due to providing high-density plasmonic hotspots and high absorbability of target molecules. Wet chemical dealloying is one of the conventional methods to create such structures (Adrien Chauvin, Cyril Delacôte, et al., 2016; Chen-Wiegart et al., 2013). It involves a selective dissolution of one metal from alloy by corrosion process. In case of the dealloying Au-Ag, HNO₃, HCl, and H₂O₂ are typically used to selectively etch Ag metal from the alloy leading to a porous structure formation (Chauvin et al., 2017; Huang et al., 2017; Qiu et al., 2011; Wiriyakun et al., 2016; Xue et al., 2017; Zhang et al., 2010).

Dealloying or selective etching is a type of corrosion in which an alloy is separated by the selective dissolution of the most electrochemically active of its elements. In bimetallic alloy, the least noble metal is defined as the active element, while the rest is called as non-active element. During dealloying process, the active element is selectively dissolved in solution generating the non-coordinated adatoms. The

adatoms reorganized themselves by diffusion and self-assembly process, agglomerating into islands and porous structures (Figure 2.8).

Figure 2.8

Schematic of Dealloying Process



The dealloying process is used to synthesize porous nanostructures in various metals depending on metal alloy precursors including Au-Ag, Ag-Ti, Ag-Al, Ag-Pt and Au-Cu (Li et al., 2008; Liu et al., 2018; Qiu et al., 2011; Satya Bharati et al., 2019; Wang et al., 2018). The mechanism of dealloying process can be described by a corrosion disordering or diffusion reordering model (Forty & Durkin, 1980). For Ag-Au alloy, the corrosion occurs by selective dissolution of Ag metal. It results in a disordered surface and generates non-coordinated Au atoms which are also known as adatoms. The Au adatoms then reorder by surface diffusion forming into gold islands and porous morphology of Ag dealloyed residues with pore size of 5-20 nm (Kertis et al., 2010; Zhang, 2016). These small nanogaps are effective for SERS due to hotspots distribution.

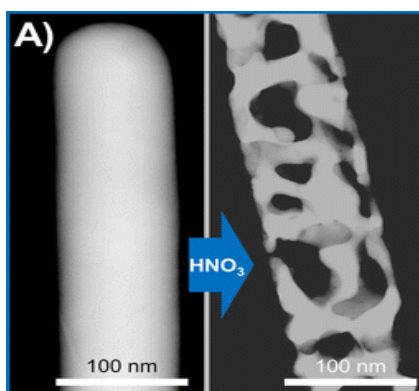
Generally, the dealloying process could be achieved by wet chemical etching and electrochemical process. The electrochemical requires applying voltage for driving the dealloying reaction and thus a complicated instrument is needed. Wet chemical etching is a traditional inexpensive and easy method to produce a porous structure of

the metal alloy. The method involves an immersion of SERS substrates into etchants for a few seconds or minutes depending on an etching strength of solution.

Among all acids, HNO_3 solution is commonly used for selective etching of Ag. Morphology, thickness and composition of etched samples can be controlled by varying the etching conditions such concentration, etching time and temperature. It has been reported that etched-Ag film with HNO_3 acid exhibits excellent SERS enhancement, high reproducibility and stability at both room temperature and high temperature in air (Lu et al., 1993). Figure 2.9 shows the porous Au-Ag alloy nanowires etched with HNO_3 solution (Burr et al., 2015).

Figure 2.9

SEM Images of Au-Ag Nanowires Array Fabricated by Electrodeposition Method and HNO_3 Etching.



Previously, fabrication of gold ribbons has been reported from alloy precursor, $\text{Au}_{20}\text{Cu}_{48}\text{Ag}_7\text{Pd}_5\text{Si}_{20}$, by dealloying process with a mixture of HNO_3 and HF solution. The addition of HF aimed to avoid SiO_2 formation when the alloy precursor contained Si. The experiment was conducted with different HNO_3 concentrations of 2, 5, 10 and 14.4 M at the dealloying times of 10 and 30 minutes, 1, 2, 3 and 4 hr. It was found that HNO_3 concentration, temperature and dealloying times affected SERS performance. Detection limit of Raman probe molecule, 4, 4'-bi-pyridine was reported as down to 10^{-14} M and 10^{-6} M of Melamine (Xue et al., 2017). Another report of L. Zhang et.al. presented the introduction of nanoporous alloy in the commercial $\text{Au}_{25}\text{Ag}_{75}$ alloy leaves. The process was carried out by using 65% HNO_3

with various reaction times. After dealloying, the samples were annealed to form bimetallic nanoporous Au-Ag alloy. The result showed that SERS enhancement increased as more residual Ag. At the same time, the annealing process could enhance the homogeneity of the residual Ag (Zhang et al., 2011).

Besides HNO₃ acid, a base solution; a mixture of NH₄OH and H₂O₂ diluted in methanol, could be used as Ag etchants in the dealloying process. The solution is commonly used in microelectronics fabrication to rapidly remove metallic Ag from metal oxide crystals. This process could be done without creating any defects on the crystal surface. Fumio Okamoto reported that the effect of the etching process depends on the etching time and the ratio of each chemical in the base solution. Their results also show a decrease in etching rate when the amount of added methanol is increased. However, no clear explanation was given regarding the function of methanol in dealloying (Okamoto, 1973).

2.4 Summary

Au-Ag alloy is a promising strategy for effective SERS substrates. It is well known that Ag has the highest SERS performance, but it has a low stability. Meanwhile Au can be used to solve the stability problem however it shows a lower SERS enhancement. Thus, the combination of these two metals; forming an alloy has been widely attempted to fabricate SERS substrate. The alloy substrate fabrication can be classified in three categories including colloid or NPs in suspension, immobilization of NPs on solid substrate and nanopatterned arrays. Among these, the nanopatterned array is a noticeable method that can provide good reproducibility, uniformity, controllable size and shape, high purity and large-scale production especially using sputtering technique.

Besides the desirable nanostructure array, surface roughness is another parameter to provide a large SERS enhancement. A simple method to create Au-Ag alloy with high surface roughness or hollow structure is galvanic replacement. The technique exploits the selective Ag dissolution and Au replacement on the sacrificial Ag template, based on the difference in their reduction potential. The reaction parameters control the morphology and metals composition of nanostructures. Another method to create surface roughness or porosity is by dealloying process. This process is carried out by simple wet chemical etching in strong acid or base solutions. Based on

the literature review, three techniques were identified that can be used for the fabrication of nanoporous arrays of bimetallic or alloyed SERS substrates with a distinctive performance. They are namely sputtering, galvanic replacement and dealloying process.

CHAPTER 3

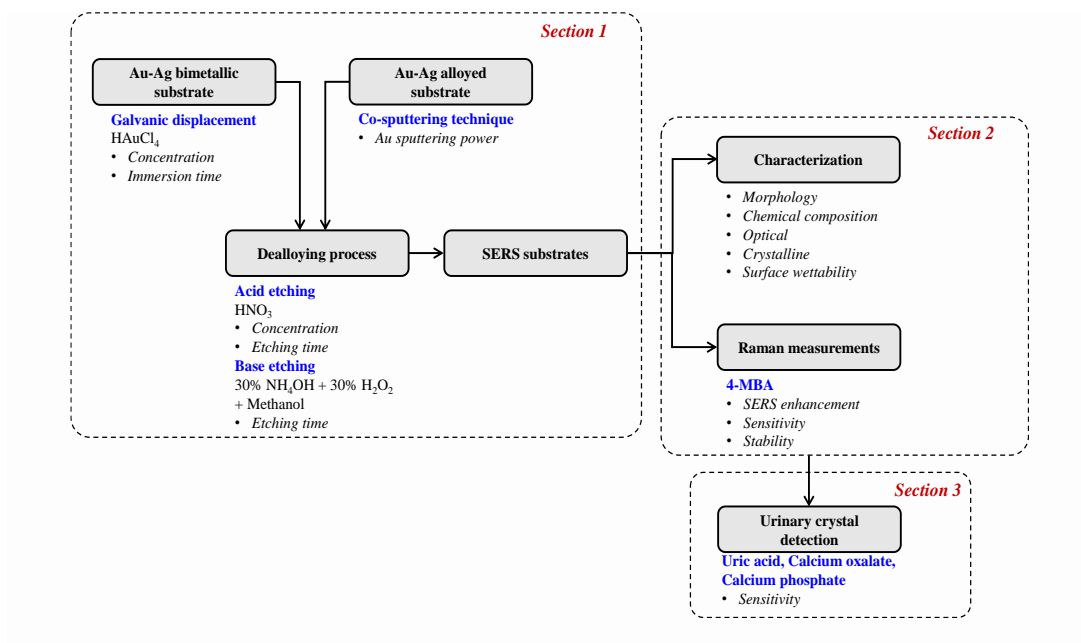
METHODOLOGY

3.1 Concepts

The overall methodology of the study is presented in the form of a flowchart in Figure 3.1. The entire methodology is divided mainly into three sections. In the first section, the procedures to fabricate the Au-Ag dealloyed SERS substrates are described. Briefly, two approaches have been investigated to fabricate the Au-Ag dealloyed SERS substrates: (1) Au-Ag bimetallic SERS substrates using sputtering and galvanic replacement techniques, followed by dealloying with wet chemical etching; and (2) fabrication of Au-Ag alloyed substrate using co-sputtering technique, followed by wet chemical dealloying process. In the second section, various characterization techniques are described that were used to investigate the morphology, chemical composition, crystal structure, optical properties, wettability and the Raman performance of the resultant SERS substrates. The sensitivity and stability of the SERS substrates were also investigated. In the third section, the experimental details for the application of the as fabricated Au-Ag dealloyed SERS substrates for urinary crystal detection are explained.

Figure 3.1

Flowchart of Thesis Methodology



3.2 Materials

Ag and Au sputtering targets were purchased from K.J. Lesker (Purity 99.99%, 2 inch diameter, 0.25 inches thick). Gold (III) chloride trihydrate ($\text{HAuCl}_4 \cdot 3\text{H}_2\text{O}$) from Sigma-Aldrich was used to prepare the Au-Ag bimetallic substrates, and 4-Mercaptobenzoic acid ($\text{HO}_2\text{C}-\text{C}_6\text{H}_4-\text{SH}$, 4-MBA, purity 99%), crystal violet ($\text{C}_{25}\text{H}_{30}\text{ClN}_3$, CV, dye content $\geq 90\%$) and methylene blue ($\text{C}_{16}\text{H}_{18}\text{ClN}_3\text{S}$, MB, dye content $\geq 82\%$) (all from Sigma-Aldrich) were used as Raman probe molecules to investigate SERS performance. Analytical grade 30% hydrogen peroxide (H_2O_2) was purchased from Chem-Supply; 30% ammonium hydroxide (NH_4OH) was obtained from CARLO ERBA. Reagents; and analytical grade methanol (CH_3OH), Isopropanol ($\text{CH}_3\text{CHOHCH}_3$), ethanol ($\text{C}_2\text{H}_5\text{OH}$) and 70% nitric acid (HNO_3) were purchased from RCI Labscan. Deionized water (DI) was prepared from deionized water systems (Labconco). Calcium oxalate monohydrate ($\text{C}_2\text{H}_2\text{CaO}_5$), Tricalcium phosphate ($\text{Ca}_3\text{P}_2\text{O}_8$) and uric acid ($\text{C}_5\text{H}_4\text{N}_4\text{O}_3$) were purchased from Sigma Aldrich. All the chemicals were used without any further purification.

3.3 Fabrication of Au-Ag Dealloyed Substrates (Approach 1)

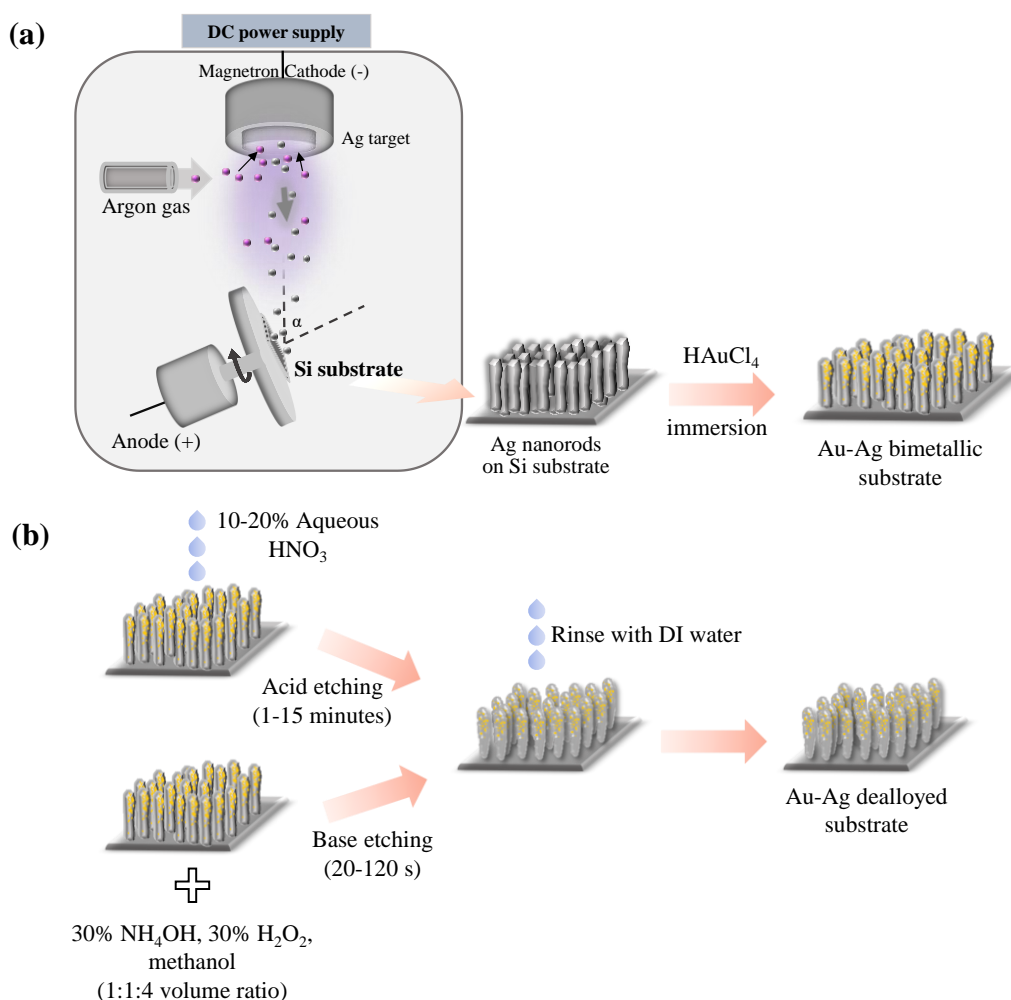
3.3.1 Au-Ag Bimetallic Substrate Preparation

Firstly, Ag substrates were prepared by a customized DC magnetron sputtering system with glancing angle deposition (GLAD) technique. A 3-inch Ag sputtering target was used for the deposition of the Ag nanostructures on a silicon (Si) base substrate of size about $5 \times 5 \text{ mm}^2$. The sputtering was carried out for 30 minutes under operating pressure of 6×10^{-3} mbar with a constant flow of 28 SCCM Argon gas in the system. The voltage and current supply were kept constant at 580 V and 0.43 A respectively. The Si substrate was rotated during the sputtering process with an angle of 85 degrees to fabricate rod shaped Ag nanostructures, as described earlier by our group (Nuntawong et al., 2017). The sputtering process to obtain the Ag substrates is schematically represented in Figure 3.2 (a).

Separately a gold chloride stock solution was prepared by adding 0.020 g HAuCl_4 into 20 ml DI water to obtain a 0.1% by weight HAuCl_4 solution. This stock solution was used to deposit Au on the Ag substrate obtained from the sputtering process. To deposit Au, the stock solution was further diluted to two final concentrations of 0.01 wt% and 0.001 wt% by adding additional DI water to a final volume of 30 ml. Then, to form the Au-Ag alloy, the Ag substrates were dipped into 0.1 wt%, 0.01 wt% and 0.001 wt% HAuCl_4 solutions for 1, 3, 5, 10 and 20 minutes at room temperature (RT). Finally, the substrates were rinsed with DI water for 3-5 times and further dried for 30 minutes at RT. The substrates prepared in this way are called Au-Ag bimetallic substrates.

Figure 3.2

(a) Schematic of Au-Ag Bimetallic Fabrication by Sputtering Technique and (b) Dealloying Process



3.3.2 Dealloying of Au-Ag Bimetallic Substrates

To obtain the dealloyed substrates, the Au-Ag bimetallic substrates were selectively etched to remove Ag metal from the bimetallic template by using a chemical dealloying process in acid and base solutions. For acid etching, 10-20% aqueous HNO₃ was dropped on the Au-Ag bimetallic surfaces for 1, 3, 5, 10 and 15 minutes at RT. Then the substrate was washed with DI and dried in air. For basic etching, a solution composed of 30% NH₄OH, 30% H₂O₂ and methanol in the ratio of 1:1:4 by volume was used. This solution was always prepared freshly before the experiment. Dealloying of the Au-Ag bimetallic substrate was then carried out by immersing it in

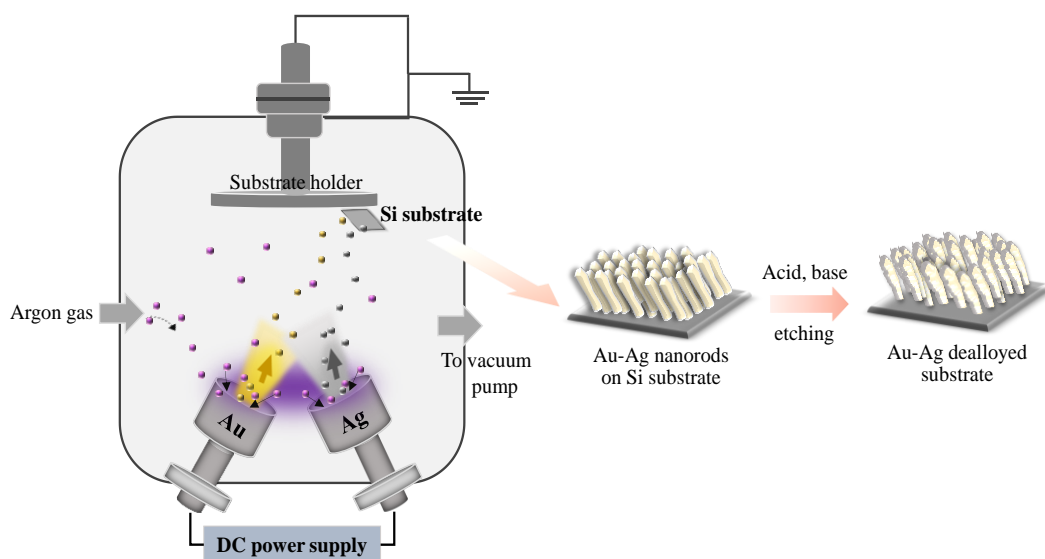
30 ml of the basic etchant solution. The etching time was set at 0 (control sample), 20, 40, 60, 80, 100 and 120 s. After that the de-alloyed substrates were immediately dipped into DI water to quench the etching reaction. Finally, dealloyed substrates were rinsed with DI water several times and dried at RT in air. Schematic of the dealloying process is shown in Figure 3.2 (b).

3.4 Fabrication of Au-Ag Dealloyed Substrates (Approach 2)

In the second approach, first Au-Ag alloy nanostructures were fabricated on $3\times 3\text{ cm}^2$ *p*-type silicon (100) wafers by co-sputtering via the oblique angle deposition (OAD) technique. Prior to the deposition the substrate was scribed to form 36 square sectors. During sputtering, argon gas was purged at a constant flow rate of 20 SCCM at a pressure of 5×10^{-3} Torr with a base pressure held constant at 6.5×10^{-6} Torr. The power outputs for sputtering Au and Ag targets were 10-50 W and 80 W respectively. The variation of Au target power affects the percentage of gold composition in the alloy structure. The silicon substrate was tilted and fixed at a constant angle of 86° with regard to the sputtering targets (as shown in Figure 3.3), and the deposition time was maintained at 20 minutes per sample. In this process, the different positions of the two sputtering targets results in a gradient film of Au and Ag on the substrate. Sectors were then optimized according to the performance and the best sectors (7.5% Au and 92.5% Ag—see results) were selected. These were cut into small pieces with dimension $5\times 5\text{ mm}^2$ for further study. Dealloying process also carried out with the same protocol as above section 3.3.2.

Figure 3.3

Schematic of Au-Ag Alloyed Fabrication and Dealloying Process



3.5 Characterization of Samples

3.5.1 Sample Morphological and Chemical Analysis

In this study, FE-SEM analysis was performed by using a Hitachi SU8030 SEM operated at 5 kV accelerating voltage and 8.0 mm working distance equipped with energy-dispersive X-ray spectroscopy. The morphology was examined on top views. The diameter and length of the nanostructure were determined by a cross-sectional approach. For EDS analysis, it used to identify the metals composition and also their atomic ratio or percent weight. X-ray photoelectron spectroscopy (AXIS SUPRA, SHIMADZU, Japan) with Al K α anode at an energy of 225 W in a vacuum of 10^{-7} Pa was employed to investigate the surface atomic composition and chemical state of the Au-Ag alloyed and dealloyed substrates.

3.5.2 Surface Wettability Test

Water contact angle (WCA) is a conventional method to measure wettability of solid materials. The degree of wetting corresponds to the physical properties of material surface, such as surface energy. A large contact angle ($> 90^\circ$) means a low wettability, while a small contact angle ($< 90^\circ$) is high wettability. The wettability behavior of Au-Ag alloyed and dealloyed substrates would affect the target molecules absorption for SERS measurements. WCA was investigated by using a

sessile drop method with a drop of water (5 μ l) using a standard goniometer (Ramé-Hart, standard goniometer model 250, USA). Due to the small area (5 mm²), only two measurements per sector were accomplished. The static WCA was then determined using the DROPimage software to determine the wettability of the substrates.

3.5.3 Optical Characterization

UV-visible spectroscopy is a common method for optical property analysis. Basic principle is based on the absorption of ultraviolet or visible light by a compound producing a distinct spectrum. The technique can measure not only absorption, but also transmission and reflection of samples. In our case, the samples are metallic thin films deposited on an opaque silicon substrate. Thus, we measured the optical properties of our samples in reflection mode which is suitable for these kinds of samples. Reflectance spectra of the Au-Ag alloyed and dealloyed substrates were measured and compared with pure Au and pure Ag by using a UV-visible spectrophotometer (Agilent technologies, Cary 7000, USA) over the wavelength range from 200 to 800 nm at an incident angle of 8°. The absorption A was then estimated from the measured reflectance R using the relation $A = \log(1/R)$.

3.5.4 Crystallographic Characterization

In this experiment, X-ray diffraction measurements were conducted to identify the crystalline phases of the film using a Bruker USA D8 advance instrument using CuK α 1 x-ray radiation source ($\lambda = 0.15405$ nm). The detection was operated using film mode with a scanning rate of 2° minute⁻¹ and 2θ ranging from 20° to 100°. 2θ is the angle between irradiated X-rays beam and the scattered beam that corresponds to diffraction pattern of materials. Identification of XRD pattern was conducted by using ICDD database.

3.5.5 Titration

To determine specific surface area of materials usually carried out with Brunauer–Emmett–Teller (BET) technique. However, our samples cannot use with this technique because of small substrate area and size of sample loading tube. Thus, we selected a titration method instead to determine the surface roughness of our samples. The technique can determine a number of molecules adsorbed on the surface substrates. In case more surface roughness that means a large number of molecules

provides. This can confirm the difference in surface roughness between the alloyed- and dealloyed substrates.

A traditional weak acid-strong base titration technique was applied using 4-MBA as the surface absorbing molecule. 4-MBA acted as the weak acid and sodium hydroxide titrant was the strong base wherein 4-MBA molecules transfer protons to hydroxide ions of NaOH via a hydrolysis reaction (Koivisto et al., 2016). Therefore, the number of 4-MBA molecules equals to the amount of NaOH added in the titration. Briefly, the titration of 2 ml of 15 mM 4-MBA dissolved in ethanol with 0.01 M NaOH was carried out. The NaOH solution was slowly added in 20 μ l aliquots. At the beginning of the titration, the curve gradually increases and reaches saturation at around pH 11-12 due to the neutralization process. At the equivalence point or half-neutralization, moles of added NaOH equals moles of 4-MBA and then calculated the number of 4-MBA adsorbed on the SERS substrates.

3.6 Raman Measurement

In this study, we will observe Raman spectrum of 4-MBA on the SERS substrate. The main characteristic peaks are 1078 and 1587 cm^{-1} . The Raman measurement was performed by Raman spectroscopy (Invia Renishaw, UK) using an excitation laser source at 532 nm at normal incidence (as shown in Figure 3.4). The laser power was maintained at 90 μ W. A 50x objective lens was used to focus the laser beam, ca. 1.2 μ m in diameter, onto a targeted spot. The grating used was 1800 lines/mm, and exposure time was kept constant at 10 s. The Raman system was calibrated beforehand using the 520 cm^{-1} band of bare silicon wafer before measurement. 10^{-4} M 4-MBA solution dissolved in ethanol was used as Raman probe for SERS characterization. For the sensitivity part of this study, only 4-MBA was tested in concentrations varied from 10^{-3} - 10^{-9} M. SERS acquisition proceeded as follows: 2 μ l of probe solution were dispersed on the Au-Ag alloyed and Au-Ag dealloyed SERS substrates. Samples were then allowed to dry in air, where 15 minutes were allocated to ensure good drying before recording the Raman spectra. Raman signals were collected from 15 different areas for each $5 \times 5 \text{ mm}^2$ substrate.

Figure 3.4

Raman Instrument



For reproducibility, Au-Ag alloyed samples were synthesized from three different batches of co-sputtered substrates followed by etching for 40 s. Raman signals of 10^{-4} M 4-MBA on these samples were observed and % relative standard deviation (RSD) was calculated for each sample. For the long term performance study, Au-Ag dealloyed substrates with 40 s etching were used to observe stability for 35 days and compare to Au-Ag alloyed substrates (no etching) and pure Ag substrates. During the storage period, all substrates were left at ambient conditions without protection. Then, 10^{-4} M 4-MBA was once again applied before measurements.

3.7 Urinary Crystal Detection

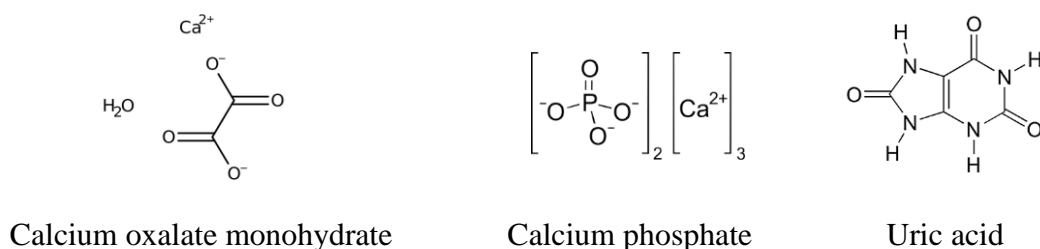
The urinary crystals including calcium oxalate monohydrate (COM), calcium phosphate (CAP) and uric acid were investigated by Raman measurement. The chemical structures of these compounds are shown in Figure 3.5. A grinding process is required before Raman measurement because the sizes of synthetic or commercial crystals are typically in micron to millimeter scale, and when these large particles adsorbed on nanostructured SERS surface, the Raman signal is diminished (Ausman & Schatz, 2008). The grinding process was carried out by mechanical method using an automatic grinding machine (Emax, Retsch, Germany). Briefly, 3 g of crystals powders were mixed with 15 ml of ethanol and put into the grinding jars containing 120 g of 1 mm diameter zirconium balls. Grinding speed and time were set at 2000 rpm and 4 hr, respectively. The overall process was repeated twice to ensure obtained particles are small enough to get a good Raman signal. After the grinding process,

crystals were then rinsed with DI water and re-suspended into DI water to prepare 10^{-4} M crystal solution. 25 μ l crystal solution was dropped on the dealloyed substrate and dried at 60 °C before Raman measurement.

The Raman measurement was performed using an excitation laser source at 532 nm at normal incidence. The laser power was maintained at 315 μ W. A 50x objective lens was used to focus the laser beam. Raman signals were then collected from 15 different areas of the substrate. Due to its highest solubility, uric acid was selected for Raman sensitivity test. Various uric acid concentrations, 10^{-3} - 10^{-7} M, were prepared by a serial dilution with DI water. In order to observe the interference effect, the same Raman sensitivity test was carried out with uric acid in synthetic urine. The synthetic urine was diluted with DI water to 1% and added uric acid into the solution to obtain a concentration of 10^{-3} - 10^{-7} M.

Figure 3.5

Chemical Structure of Calcium Oxalate Monohydrate (COM), Calcium Phosphate (CAP) and Uric Acid



3.8 Data Analysis

All Raman spectra were subtracted baseline using a software program namely Wire 4.2 in the Raman instrument. After baseline correction, the Raman intensity was directly compared by means of the main characteristic peaks of each sample.

3.8.1 SERS Enhancement Factor

The SERS enhancement factor (EF) is described as the intensity ratio between the SERS signal and that expected from regular non-SERS Raman scattering for a given

analyte molecule, normalized by the special number of the probed molecule. The EF can be calculated by the following equation:

$$EF = \frac{I_{SERS}}{I_{Raman}} \times \frac{N_{Raman}}{N_{SERS}} \dots\dots\dots(3.1)$$

where I_{SERS} and I_{Raman} denote the intensities of 4-MBA at 1078 cm^{-1} Raman shift of the SERS and normal Raman spectra. N_{SERS} is the number of 4-MBA molecules adsorbed on the SERS substrate in the area being probed. N_{Raman} is the number of molecules within the excitation volume of the laser used in a regular Raman measurement. The SERS and normal Raman spectra were measured under the same condition (a 532 nm laser excitation at a power of $315 \mu\text{W}$, with ND filter 5, and an exposure time of 10 s).

3.8.2 Limit of Detection

Limit of detection (LOD) was calculated from the standard curve of different of concentration according to the formula:

$$LOD = 3.3 \times \frac{SD_{Blank}}{Slope} \dots\dots\dots(3.2)$$

SD_{Blank} = Standard deviation of blank sample

Blank sample = the solution without analytes

Slope = Slope of the regression line

CHAPTER 4

RESULTS AND DISCUSSION

4.1 Fabrication of Au-Ag Bimetallic Nanorods via Galvanic Replacement and Dealloying Process

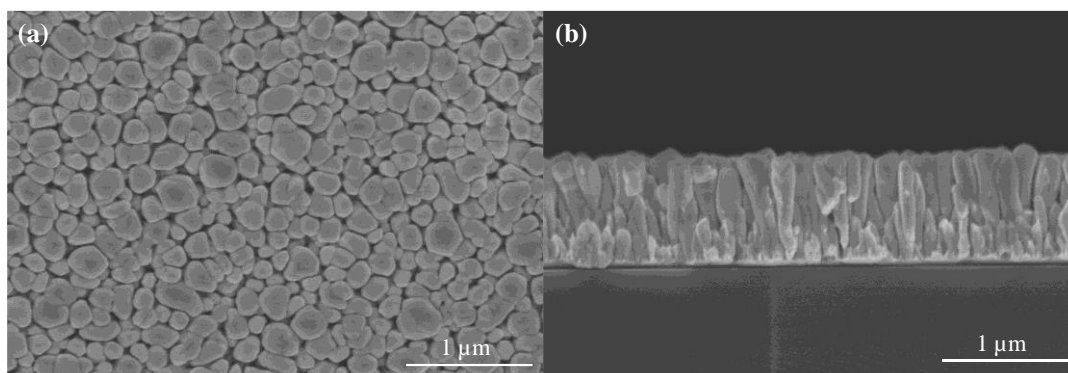
The Au-Ag bimetallic substrates were first prepared by sputtering of Ag nanorods followed by galvanic replacement of Ag with Au in HAuCl_4 solution. In the process, aligned Ag nanorods film on silicon substrate was initially fabricated by sputtering technique with glancing angle deposition. Then, the Ag film was exposed to HAuCl_4 solution to create Au-Ag bimetallic structure driven by spontaneous galvanic reaction. To further enhance the surface roughness, selective Ag dealloying from the Au-Ag bimetallic film surface was carried out by using acid and base etching. The conditions of the dealloying process were studied by varying concentrations of the etchants and etching time. Morphology, metal composition, optical property, crystal structure and SERS properties of the prepared Au-Ag bimetallic dealloyed substrates were investigated and subsequently discussed below.

4.1.1 Ag Film Morphology

Figure 15 shows SEM images of (a) top and (b) cross-section views of Ag nanorods grown on Si substrate using the GLAD sputtering technique. Vertically aligned Ag nanorods of varying diameters were observed on the silicon surface. The average diameter of these Ag nanorods, obtained from Figure 4.1 (a), was equal to 220 nm with a variation of 55 nm. The cross-sectional SEM view, as shown in Figure 4.1 (b), indicated a tightly packed arrangement of the Ag nanorods with length around 880 ± 17 nm. Considering the growth mechanism, the combination of GLAD technique and substrate rotation can result in different nanostructure configuration. Typically, at glancing angle (θ) greater than 70° with an optimum rotation speed, ordered columnar nanostructures can be generated (Horprathum, 2014). However, the rotation speed of the substrate and self-shadowing effect still have an effect on the size variation of the nanorods (Horprathum et al., 2014; Jayaraman et al., 2016).

Figure 4.1

SEM Images of (a) top and (b) Cross-section of Ag Thin Film Fabricated by GLAD Sputtering With Rotation of Silicon Substrate.

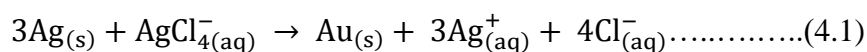


4.1.2 Au-Ag Bimetallic Film Morphology and Composition

The Au-Ag bimetallic thin films were prepared by galvanic replacement of Ag by Au by treating the Ag thin films, fabricated by GLAD sputtering method, with HAuCl_4 solution. The concentration of HAuCl_4 plays an important role in the galvanic replacement and affects the structure, morphology and metal composition in the thin films. Thus, we prepared the Au-Ag bimetallic thin films by varying the HAuCl_4 concentration, starting from 0.1 wt% down to 0.001 wt%, with different deposition time ranging between 1-10 minutes and investigated their morphology and chemical compositions. Figure 4.2 shows the top and cross-sectional SEM views of the Ag film after immersion in 0.1 wt% HAuCl_4 solution for (a, d) 1, (b, e) 3 and (c, f) 5 minutes, respectively. Ag nanorods were observed to cover with thin and irregular gold layers distributed on the surfaces, showing an increasing trend of these irregular layers as the immersion time increases from 1 to 5 minutes. During the galvanic replacement mechanism, the reaction generally occurs spontaneously when a less noble metal comes in contact with a more noble metal or more standard reduction potential.

In our case, the standard reduction potential of $\text{AuCl}_4^-/\text{Au}$ is 1.002 V versus SHE while the oxidation potential of Ag^+/Ag is lower, about 0.8 V vs SHE. As a result, as shown in the equation 4.1, three Ag atoms are oxidized and dissolved into the solution while only one Au atom is reduced and displaced on the Ag template.

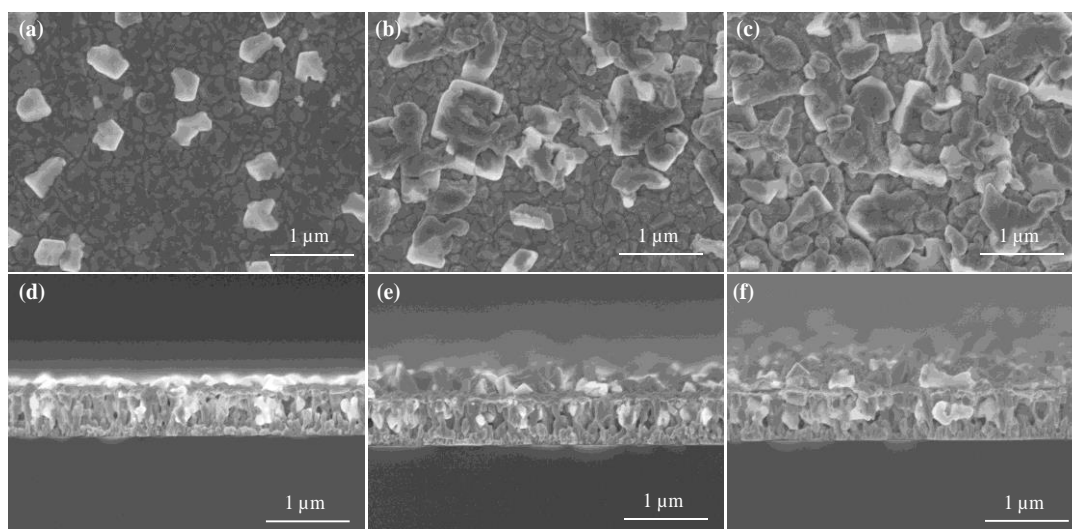
Nucleation of Au metal then occurs, followed by the growth process and finally forming to thin sheets as observed in Figure 4.2.



The obtained Au-Ag bimetallic structure depends on the amount of Ag displaced by Au metal. The final structure depends on various factors including surface area of the Ag template, concentration of AuCl_4^{-} , incubation time and temperature. With the 0.1 wt% HAuCl_4 solution, the gold concentrations are rather high causing deformation of the sacrificial Ag structure leading to large gold agglomeration on the surface. Thus, the HAuCl_4 concentration should be decreased to find a condition where the Au metals are partially deposited on the Ag surface forming Au-Ag bimetallic structure without deforming or collapsing the Ag core template.

Figure 4.2

SEM Images of the top and Cross-sectional SEM Views of the Ag Film After Immersion in 0.1 wt% HAuCl_4 Solution for (a, d) 1, (b, e) 3 and (c, f) 5 Minutes



The HAuCl_4 solution was therefore further diluted by 10 and 100 folds to 0.01 wt% and 0.001 wt% respectively, and the Ag films were immersed into the diluted solutions for 1, 3, 5 and 10 minutes. The SEM micrographs of the Au-Ag bimetallic structures obtained with the 0.01 wt% HAuCl_4 solution at various immersion time are shown in Figure 4.3. The micromorphology of the Ag nanorods revealed a great

change upon immersion in 0.01 wt% HAuCl_4 solution. First of all, no thin and irregular Au layers were observed on the Ag film surface when the diluted HAuCl_4 solution was used. The immersed samples showed nearly a homogenous surface roughness with small pores at 1 minute immersion time and gradually the pore size became larger with increasing immersion time, 3-5 minutes. When the immersion was prolonged to 10 minutes, no pores were observed at the Ag surface and large amount of gold clusters was appeared. EDS analysis, summarized in Table 4.1, showed that the relative weight percent of Au increased (0.50, 1.62, 2.53 and 6.50) as the immersion time was increased from 1 to 10 minutes. In contrast, the relative Ag weight percent was decreased (99.51, 98.39, 97.47 and 93.50 respectively).

Figure 4.3

SEM Micrographs of Au-Ag Bimetallic Thin Films Obtained by Galvanic Replacement of Ag With 0.01 wt% HAuCl_4 Solution for (a) 1, (b) 3, (c) 5 and (d) 10 Minutes.

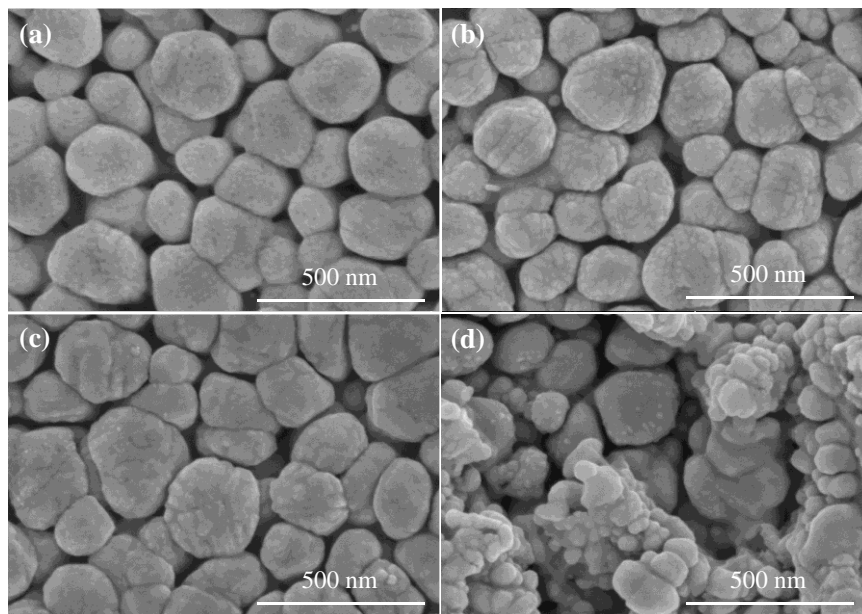


Table 4.1

Elemental Composition of the Au-Ag Bimetallic Thin Films Obtained for EDS Analysis. The Au-Ag Bimetallic Structures Were Obtained by Galvanic Replacement of Ag With 0.01 wt% HAuCl₄ Solution for Varying Immersion Time Ranging From 1-10 Minutes.

Immersion time (minutes)	Weight (%) ± SD	
	Ag	Au
1	99.51 ± 0.05	0.50 ± 0.05
3	98.39 ± 0.26	1.62 ± 0.26
5	97.47 ± 0.00	2.53 ± 0.00
10	93.50 ± 0.79	6.50 ± 0.79

In case of the 0.001 wt% HAuCl₄ solution, the obtained Au-Ag bimetallic structures exhibited a small but not clear change in terms of the surface roughness. Figure 4.4 shows the SEM micrographs of the Au-Ag bimetallic structures obtained by galvanic replacement using the 0.001 wt% HAuCl₄ solution for varying immersion time (1-10 minutes). EDS results, summarized in Table 4.2, also revealed significantly less amount of Au on the bimetallic structure when 0.001 wt% HAuCl₄ solution was used. Interestingly, the amount of Au on the Au-Ag bimetallic structure was found to remain almost the same (approximately 0.1 wt%-0.2 wt%) irrespective of the immersion time, suggesting that the concentration 0.001 wt% HAuCl₄ is not enough to proceed the galvanic replacement reaction (GRR).

Figure 4.4

SEM Micrographs of Au-Ag Bimetallic thin Films Obtained by Galvanic Replacement of Ag With 0.001 wt% HAuCl₄ Solution for (a) 1, (b) 3, (c) 5 and (d) 10 Minutes.

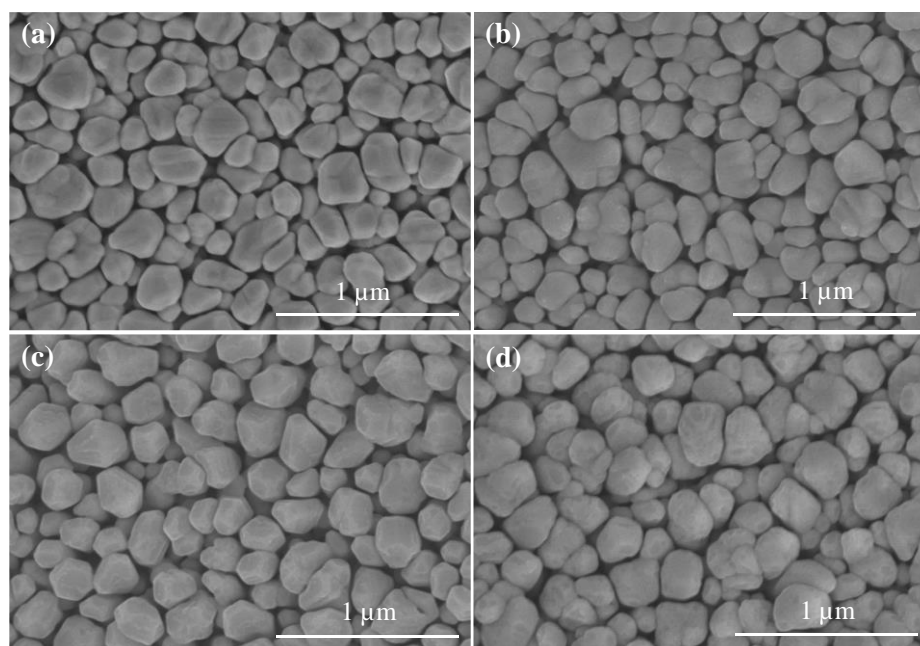


Table 4.2

Elemental Composition of the Au-Ag Bimetallic Thin Films Obtained for EDS Analysis. The Au-Ag Bimetallic Structures Were Obtained by Galvanic Replacement of Ag With 0.001 wt% HAuCl₄ Solution for Varying Immersion Time Ranging From 1-10 Minutes.

Immersion time (minutes)	Weight (%) ± SD	
	Ag	Au
1	99.82 ± 0.02	0.18 ± 0.02
3	99.87 ± 0.11	0.13 ± 0.11
5	99.89 ± 0.05	0.11 ± 0.05
10	99.84 ± 0.06	0.16 ± 0.06

Based on these findings, we concluded that the 0.01 wt% H_{AuCl}₄ concentration exhibited controlled surface roughness concordance with the change in relative composition of the two metals in the Au-Ag bimetallic thin film. Thus, we continued only with this concentration for the further experiments.

4.1.3 Optical and Crystallographic Properties of the Au-Ag Bimetallic Thin Films

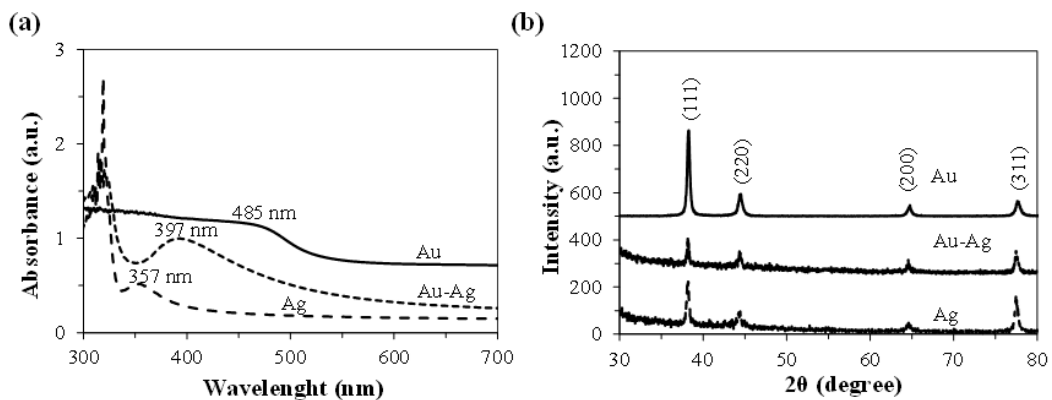
UV-vis spectroscopy was used to study the optical properties of the prepared Au-Ag thin films. Figure 4.5 (a) shows absorption spectra of Ag, Au and Au-Ag bimetallic substrates (obtained at 0.01 wt% H_{AuCl}₄ solution for 3 minutes). The spectra showed maximum absorption at 485 and 357 nm for pure Au and Ag films respectively, corresponding to their surface plasmon absorption peaks. While the Au-Ag bimetallic substrate presents only a single absorption peak, maximum at 397 nm, that is located between pure Au and pure Ag. This confirms the Au-Ag bimetallic alloy formation. Owing to the rich Ag content, the absorption peak of the Au-Ag bimetallic structure is close to the Ag and shift towards a higher wavelength region due to the presence of the Au particles (Moore, 1928; Zhou et al., 2016). Similar results of red-shift of the absorption peak to longer wavelengths were also observed by other researchers at the early stage of the alloy formation via galvanic replacement (Sun & Xia, 2004).

To investigate the crystalline structure of the prepared Au-Ag bimetallic thin films, XRD analysis was carried out and compared to the pure Ag and Au metallic substrates. XRD patterns of Ag, Au and Au-Ag bimetallic substrates are depicted in Figure 4.5 (b). The Au-Ag bimetallic substrates showed prominent peaks at diffraction angles 2θ equal to 38.2°, 44.3°, 64.5° and 77.4°. This profile is similar to those associated with pure Ag and pure Au. Au and Ag have similar crystalline structure due to their similarity of lattice constants (Ag = 4.086 Å, Au = 4.078 Å) (Xia et al., 2013; Yu et al., 2017). The observed peaks corresponded to (111), (220), (200) and (311) planes, characteristic of a face centered cubic (FCC) structure for natural Ag and Au crystallites (Godipurge et al., 2016). Based on the Scherrer equation shown in equation 4.2, the average crystallite size of the Au-Ag bimetallic structure was estimated to be 30.7 nm which lies in between the crystallite sizes of Au and Ag (24.5 and 33.6 nm). As the results indicated, the crystallite size decreases

from 33.6 nm (for pure Ag) down to 30.7 nm when Au replaces some of the Ag atoms forming the Au-Ag bimetallic alloy structure.

Figure 4.5

(a) UV-vis Absorption Spectra and (b) XRD Patterns of Pure Ag, pure Au and Au-Ag Bimetallic Substrates.



Note. Pure Ag and pure Au substrates were prepared by using the GLAD sputtering method and the Au-Ag bimetallic structures were obtained by galvanically replacing Ag with Au, as described earlier.

$$D = \frac{K \times \lambda}{\beta \times \cos \theta} \dots \dots \dots (4.2)$$

where D is the crystallite size in nm, $K = 0.94$ is a shape factor or Scherrer constant, $\lambda = 0.154056$ nm is the wavelength of the X-ray radiation, β is the angular full-width at half maximum (FWHM) of the XRD peak, and θ is the diffraction angle of the peak.

From the UV-vis and XRD results, we concluded the alloy formation between Au and Ag resulting in the Au-Ag bimetallic structure. However, the alloy formation is not completely extended to the entire Ag nanorods due to the short galvanic reaction time. The Au-Ag bimetallic thin films obtained in this way are further referred to as Au-Ag bimetallic substrates.

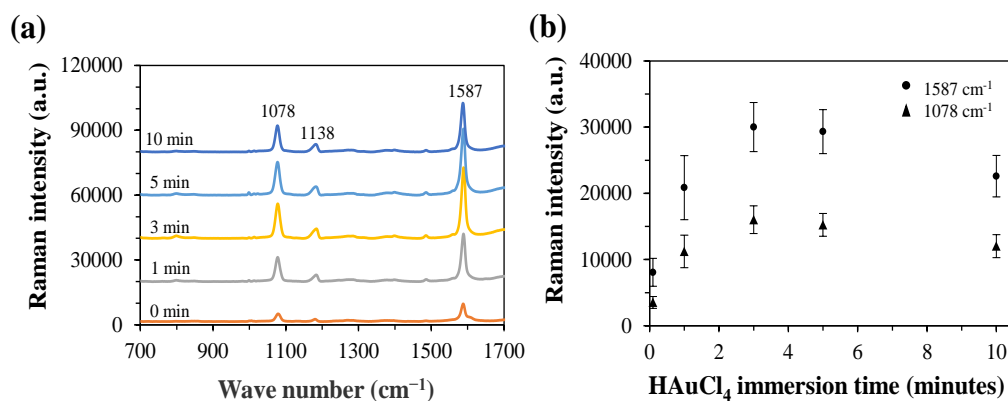
4.1.4 Raman Characterization and SERS Performance of the Au-Ag Bimetallic Substrates

Raman measurements were carried out using 4-MBA as a Raman probe molecule with 532 nm laser excitation wavelength. The Raman spectra obtained from the Au-Ag bimetallic substrates prepared with different immersion time (1-10 minutes) and the corresponding intensities of the characteristic Raman peaks of 4-MBA are given in Figure 4.6 (a). Raman spectra of 4-MBA on the substrates clearly showed two main characteristic peaks at 1078 and 1587 cm^{-1} attributed to the aromatic ring-breathing modes of the molecule. The less intense peak, at 1183 cm^{-1} , corresponds to the C-H deformation mode of 4-MBA (Ho & Lee, 2015). In Figure 4.6 (b), the Raman intensities of the two characteristic peaks of 4-MBA are shown as a function of the immersion time of the Ag substrates during the galvanic replacement process. At immersion time of 3 minutes, highest intensities for both the peaks were observed, which then gradually decreased with increasing immersion times from 5 minutes until 10 minutes. During the galvanic replacement, as described in section 4.1.2, Ag is removed from the template substrate and Au nanoparticles are deposited resulting in surface roughness. Higher surface roughness can generate more plasmonic hot spots with an intense local field enhancement contributing to higher SERS intensities.

As a result, the Raman intensities of the probe molecule with the Au-Ag bimetallic SERS substrates increased, initially attaining maximum for the 3 minutes immersion samples. However, for longer immersion times, as the Ag metals decreased further and Au content increased, the SERS intensity was observed to decreased indicating that the Au-Ag bimetallic substrates obtained at 3 minutes of galvanic replacement with 0.01 wt% HAuCl_4 solution provides the best condition to achieve highest SERS performance. Thus, the Au-Ag bimetallic SERS substrates obtained by using galvanic replacement of Ag in 0.01 wt% HAuCl_4 solution for 3 minutes were selected to use for subsequent studies.

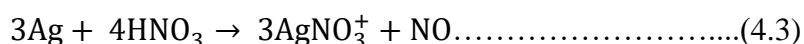
Figure 4.6

(a) Raman Spectrum of 10^{-4} M 4-MBA on the Au-Ag Bimetallic Substrate With Different Immersion Time in 0.01 wt% HAuCl₄ Solution, and (b) Variations in the Raman Intensities of the 4-MBA Characteristic Peaks at 1078 and 1587 cm^{-1} as a Function of the Immersion Time for Galvanic Replacement. 0-minute Sample Indicates the Pure Ag Substrate Which was Used as a Control Sample.



4.1.5 Selective Etching of the Au-Ag Bimetallic Substrates

4.1.5.1 HNO₃ Acid Etching. The dealloying using wet chemical etching methods usually uses HNO₃ for the selective Ag etching especially in alloy composition. The chemical reaction between Ag with HNO₃ is given by,



In this experiment, we investigated the dealloying process of the Au-Ag bimetallic film with HNO₃ as ethant at various concentrations (10, 15, 20 and 25%) and incubation time (1, 3, 5, 10 and 15 minutes). As mentioned above, Au-Ag bimetallic film immersed in 0.01 wt% HAuCl₄ solution for 3 minutes was selected to study the dealloying process. Aqueous HNO₃ solution was dropped on the Au-Ag bimetallic substrates to selectively remove Ag. At higher concentrations of HNO₃ we observed complete peeling of the Au-Ag film from the Si substrate. The film was peeled off within 1 minute after dropping the 20-25% HNO₃ and within 3 minutes with 15% HNO₃. With 10% HNO₃, no peeling of the Au-Ag bimetallic film was observed until 15 minutes. Figure 4.7 shows the SEM micrographs of the dealloyed substrates obtained with 10% HNO₃ etchant at different points in time. After the dealloying

process, a significant alteration in the surface morphology of the Au-Ag bimetallic substrates was observed. The nano-scale roughness of the surface disappeared within 1 minute of acid etching resulting in more smoother nanostructures and the nanostructures tended to coalesce as etching time was increased to 10 minutes (Figure 4.7 (a-e)). At 15 minutes etching time, nanostructures were etched into smaller sized irregular structures and partially formed islands as shown in Figure 4.7 (f). From the EDS analysis (Table 4.3), no significant change in the % weight of Ag and Au was observed as the acid etching time was increased.

Figure 4.7

SEM Micrographs of Au-Ag Dealloyed Substrates Obtained by Using 10% HNO₃ Solution as Etchant Showing the Surface Morphology at Different Etching Time: (a) 0 Minute (b) 1 Minute (c) 3 Minutes (d) 5 Minutes (e) 10 Minutes and (f) 15 Minutes.

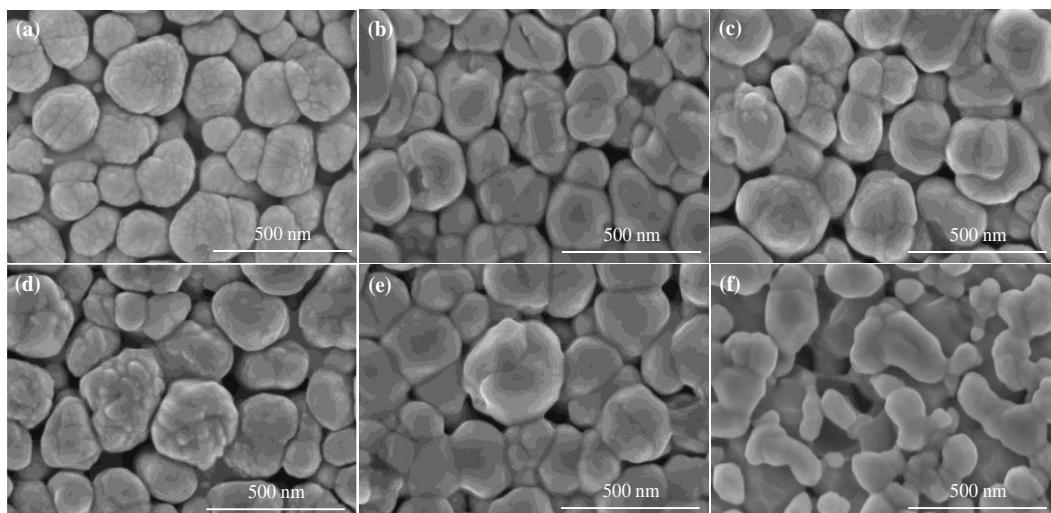


Table 4.3

Elemental Composition of the Au-Ag Dealloyed Films Obtained by Etching With 10% HNO₃ Solution at Different Etching Times (0-15 Minutes).

10% HNO ₃ etching time (minutes)	Weight (%) ± SD	
	Ag	Au
0	98.39 ± 0.26	1.62 ± 0.26
1	98.98 ± 0.11	1.03 ± 0.11
3	98.28 ± 0.14	1.73 ± 0.14
5	98.96 ± 0.11	1.04 ± 0.11
10	98.54 ± 0.18	1.47 ± 0.18
15	98.62 ± 0.20	1.38 ± 0.20

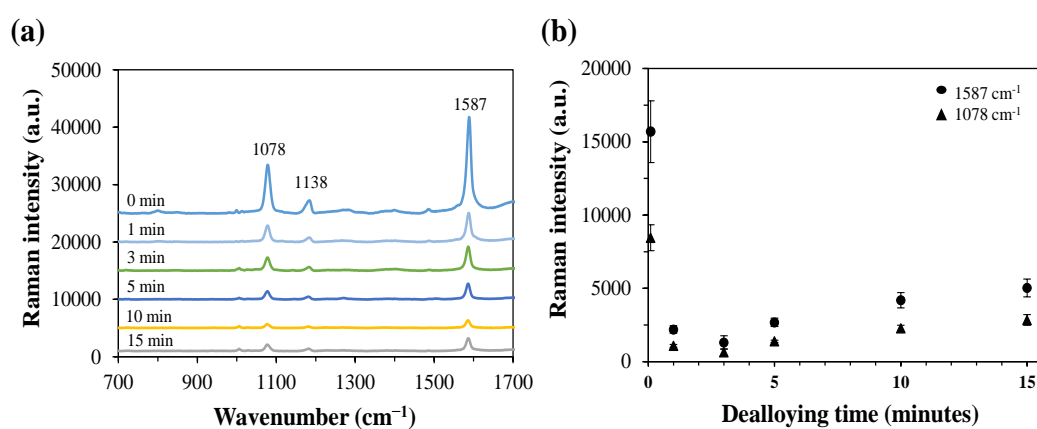
The Raman signal intensities of 4-MBA molecules recorded using the Au-Ag dealloyed substrates, however, were found about 3-6-folds lower than the corresponding unetched Au-Ag bimetallic substrates, as shown in Figure 4.8. Previously, it has been reported that HNO₃ with a concentration more than 3.5 M can effectively create surface roughness on Ag foil substrate (Lu et al., 1993). To compare with this report, the % concentrations of HNO₃ used in this study were converted into molarity (M) and based on the calculations, 10-25% HNO₃ yielded concentrations equal to 2.25, 3.38, 4.51 and 5.64 M respectively. The higher concentrations of HNO₃ (4.51-5.64 M) have potential for effective Ag etching from the bimetallic substrate. However, at these concentrations we observed lifting or peeling of the films from the silicon substrate within a few minutes. One possible reason for this is that our Au-Ag bimetallic films did not use any adhesive sputtering layer underneath to promote adhesion with the Si substrate.

If the film contains a pre-deposited chromium adhesion layer, an optimum etching condition can be reached with 70% HNO₃ (Huang et al., 2017). However, it certainly increases more complex sputtering processes and also increases the fabrication cost.

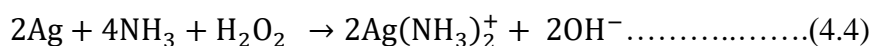
This finding implies that a mild etching reaction with 10% (2.25 M) HNO₃ acid results only in Ag atoms self-diffusion or rearrangement on surface due to low dissolution rate and does not remove Ag effectively from the substrate. This can be also confirmed from the EDS results shown in Table 4.3 where no significant variations in the Ag content in the dealloyed films was observed until 15 minutes of etching using 10% HNO₃ solution. The Ag atoms self-diffusion or rearrangement at 10% HNO₃ concentration, therefore, produce a smoother surface rather than creating roughness and consequently lower the SERS signal from the Au-Ag dealloyed substrates.

Figure 4.8

(a) SERS Intensity of 10⁻⁴ M 4-MBA on the Au-Ag Dealloyed Substrates Obtained by Etching With 10% HNO₃ Solution at Different Time (0-15 Minutes) and (b) Variations of the Raman Intensities of the Characteristic Peaks of 4-MBA (1078 and 1587 cm⁻¹) With Respect to the Dealloying Time.



4.1.5.2 30% H₂O₂: 30% NH₄OH: Methanol Base Etching. As an alternative to the acid etching, a base etching approach was used to study the dealloying process of the Au-Ag bimetallic substrates. Earlier it has been reported that a mixture of H₂O₂, NH₄OH and methanol is an effective etching solution to remove Ag from metal oxide crystals (Okamoto, 1973). A mixture of 30% H₂O₂: 30% NH₄OH diluted in methanol at a volume ratio of 1:1:4 was used to selectively remove Ag from our Au-Ag bimetallic films. The chemical reaction of Ag with NH₃ and H₂O₂ is shown below.



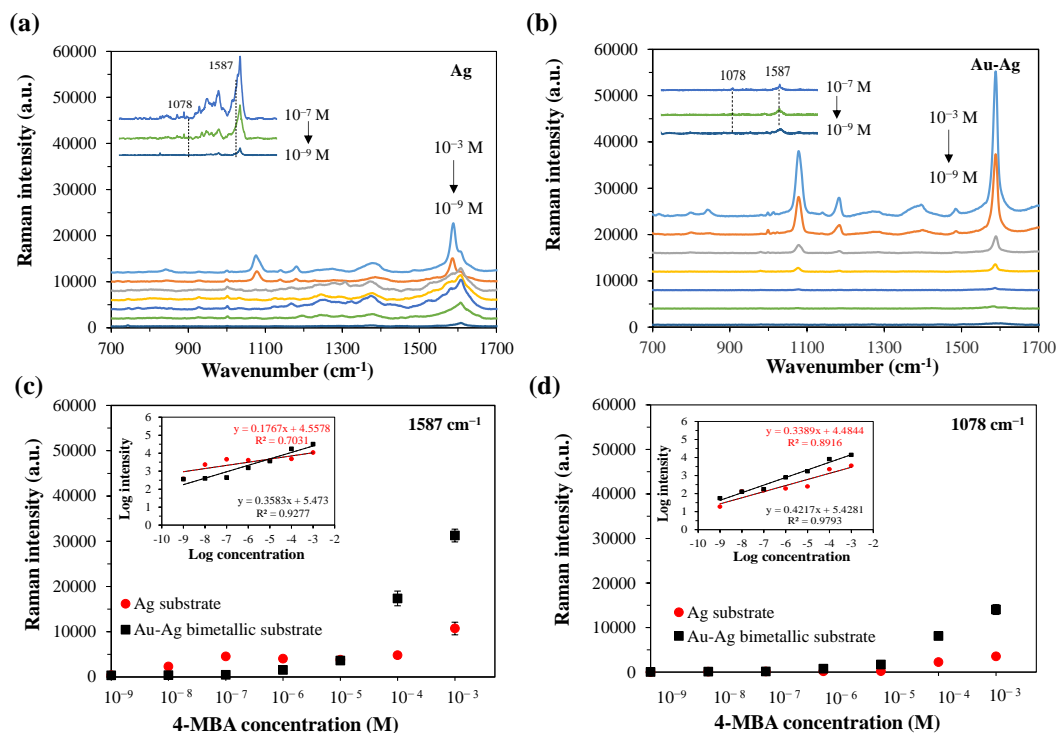
Upon immersion of the Au-Ag bimetallic substrates into the base etchant, we found peeling of the film within 5 s. This is because the NH_4OH and H_2O_2 mixture in methanol is a strong etchant and can rapidly react with the Ag metallic film with a high etching rate resulting in quick peeling of the film. We therefore did not continue with this approach of base etching to dealloy the Au-Ag bimetallic films.

4.1.6 Sensitivity Measurements

In this experiment, we investigated the Raman signals of 4-MBA on the Au-Ag bimetallic substrate and compared the same with pure Ag substrates, where the concentration of 4-MBA was varied between 10^{-9} - 10^{-3} M. Figure 4.9 (a-b) shows the Raman spectra of 4-MBA measured by using pure Ag and Au-Ag bimetallic films as SERS substrates. In all cases the 4-MBA Raman spectrum was clearly observed at all concentrations. By comparing the SERS performance, the intensity of the two main characteristic peaks of 4-MBA at 1078 and 1587 cm^{-1} were plotted against the concentration of 4-MBA as shown in Figure 4.9 (c-d). At 1587 cm^{-1} , for the 4-MBA concentration of 10^{-3} - 10^{-5} M, the signal on the Au-Ag bimetallic substrate was larger than that from the Ag substrate. For the lower 4-MBA concentrations of 10^{-6} - 10^{-9} M, the signal on pure Ag was higher than on the bimetallic substrate. Considering at 1078 cm^{-1} , the result shows that the bimetallic substrates exhibit a larger signal than the Ag substrates at all concentrations. The insets graph in Figure 4.9 (c-d) shows a log scale plot between Raman intensity and 4-MBA concentration. The graphs exhibited a linear regression in a range of 10^{-3} - 10^{-9} M. Limit of detection was then calculated to be 1.2×10^{-8} M and 1.6×10^{-9} M for Ag and Au-Ag bimetallic substrates. These results confirm that the bimetallic substrates composed of enriched-Ag metal structure and a small amount of Au deposited on the surface could provide a higher SERS signal compared to pure Ag. This enhancement is concordance with large SERS hotspots generated from surface roughness of the bimetallic substrates.

Figure 4.9

(a) SERS Intensity of 10^{-9} - 10^{-3} M 4-MBA on Ag Substrate (b) on Au-Ag Bimetallic Substrate. Dependence of the 4-MBA Concentration and Raman Intensities at Characteristic Peaks of (c) 1587 and (d) 1078 cm^{-1} .



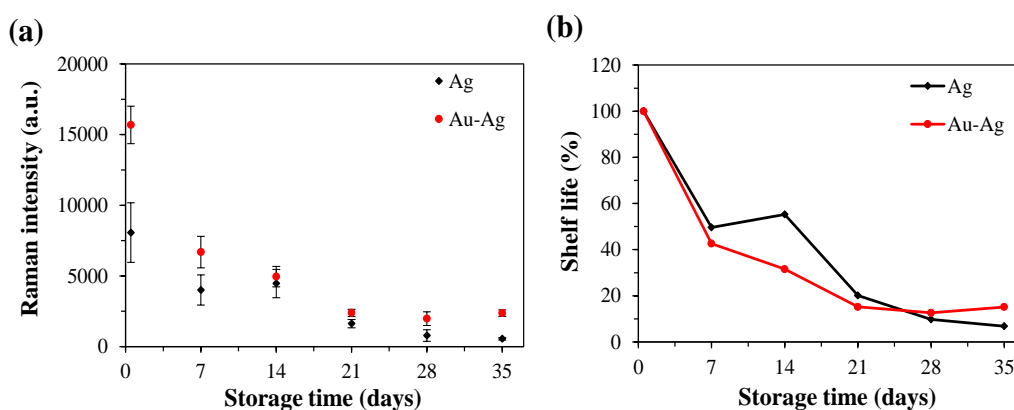
4.1.7 Stability of the Au-Ag Bimetallic SERS Substrates

Besides SERS sensitivity, the stability of the Au-Ag bimetallic substrate was also studied and compared with pure Ag substrates. For the stability tests, freshly prepared pure Ag and Au-Ag bimetallic SERS substrates were exposed to the air in ambient conditions for about a month. 4-MBA molecules were dropped on the surface of the substrates right before the Raman measurements which were conducted on day 0, 7, 14, 21, 28 and 35. Raman intensity of 4-MBA at a characteristic peak of 1078 cm^{-1} obtained from the SERS substrates as a function of storage time were shown in Figure 4.10 (a). The results demonstrated that the shelf life of pure Ag substrate was dramatically decreased to 49% within 7 days and remained only 7% at 35 days. Meanwhile, the shelf-life of the Au-Ag bimetallic substrates were also dramatically decreased to around 42 % at day 7 and around 15% signal was still observable at the end of the month (Figure 4.10 (b)). The degradation of the two SERS substrates found

to be similar because of almost same amount of Ag present in both cases with very little Au in the bimetallic substrate.

Figure 4.10

(a) SERS Signal of 10^{-4} M 4-MBA at 1078 cm^{-1} Characteristic Peak on Pure Ag and Au-Ag Bimetallic (0.01 wt% HAuCl_4 for 3 Minutes) Substrates and (b) Shelf Life Until 35 Days.



4.2 Fabrication of Au-Ag alloyed Nanorods by Co-sputtering Deposition and Their Dealloying Process

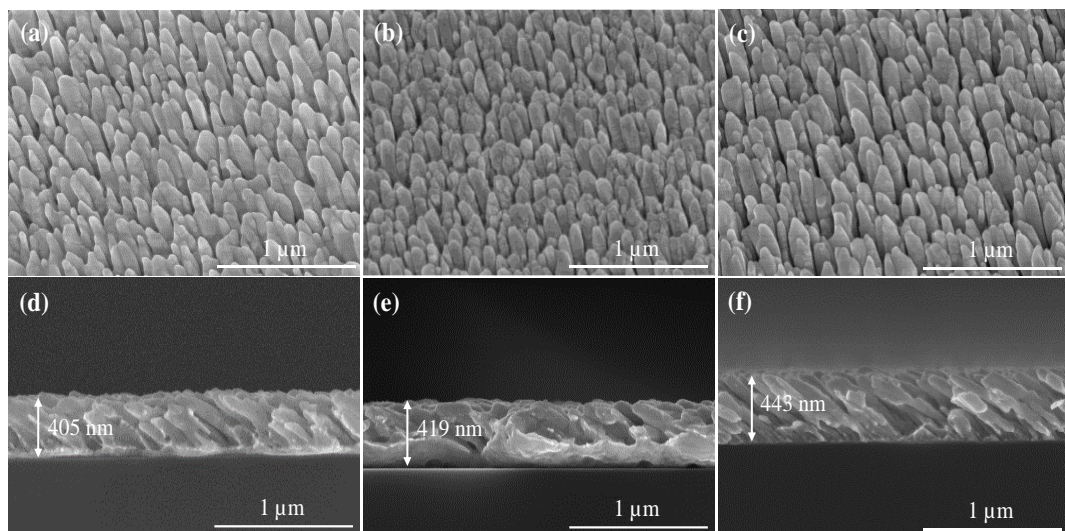
4.2.1 Au-Ag Alloyed Film Morphology and Composition

In the previous section for the Au-Ag bimetallic thin films, we have seen that the percent weight of Au in the nanostructure can be controlled by varying the HAuCl_4 concentration and incubation time. In this section we report the fabrication of the Au-Ag alloyed nanorods by co-sputtering method where we have varied the Au and Ag composition in the nanorods simply by changing the sputtering power of Au during the co-sputtering process while the sputtering power of Ag was kept constant. The sputtering power of Au was varied as 10, 30 and 50 W and the resultant Au-Ag alloyed nanorod films were then characterized for their morphology and metal composition by SEM and EDS analysis. Figure 4.11 shows the SEM micrographs of the Au-Ag alloyed substrates with various Au sputtering power while Ag power was kept constant at 80 W. All the Au-Ag alloyed films exhibited a tilted nanorods structure when fabricated using different Au sputtering power. The average diameters of the Au-Ag nanorods fabricated at Au sputtering power of 10, 30 and 50

W were 103 ± 18 nm, 104 ± 14 nm and 120 ± 18 nm, respectively. The nanorod film thickness was also varied to 405 ± 9 nm, 419 ± 9 nm and 443 ± 9 nm. As the results, we found that the diameter and film thickness were increased when the Au sputtering increased. When the sputtering power increases, this can generate an increased flux of target atoms growing to the substrate with a higher deposition rate. More atoms deposit on the substrate, these can improve both diameter and film thickness (Naveed, 2016).

Figure 4.11

Surface and Cross-sectional SEM Images of Au-Ag Alloyed Substrates Fabricated by Co-sputtering With Fixed 80 W Ag Sputtering Power and Varied Au Sputtering Power of (a -d) 10 W (b-e) 30 W and (c-f) 50 W.



EDS analysis on the elemental composition of the films (shown in Table 4.4) revealed that the alloy substrates were composed of 8.01, 21.16 and 30.52% Au and 91.99, 78.84 and 69.48% of Ag respectively. This suggests that the film composition can be tuned by varying the Au sputtering power during the co-sputtering process without altering the overall morphology of the Au-Ag alloyed nanorod films.

Table 4.4

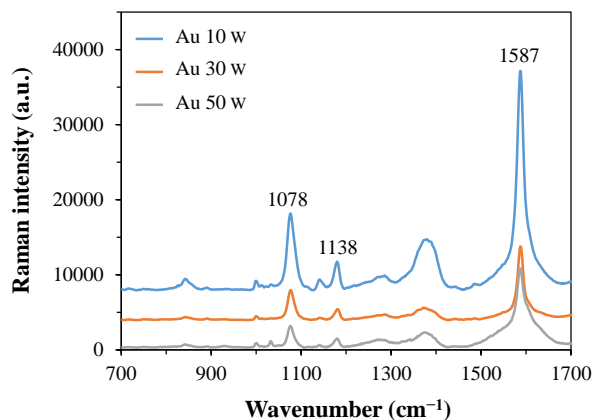
Elemental Composition of Au-Ag Alloyed Nanorods Fabricated With 10, 30 and 50 W of Au Sputtering Power. Ag Sputtering Power was Kept Constant at 80 W During the Process.

Au sputtering power (W)	Weight (%) \pm SD	
	Ag	Au
10	91.99 \pm 0.63	8.01 \pm 0.63
30	78.84 \pm 0.20	21.16 \pm 0.20
50	69.48 \pm 0.58	30.52 \pm 0.58

After the morphological and compositional investigations, the obtained Au-Ag alloyed nanorod films were tested for their SERS performance using Raman spectroscopy. Figure 4.12 shows the Raman spectra of 4-MBA on the Au-Ag alloyed substrates fabricated at different Au sputtering power of 10, 30 and 50 W. All SERS substrates showed strong 4-MBA characteristic peaks at Raman shift of 1078 and 1587 cm^{-1} that corresponded to ring breathing modes $\nu(\text{CC})$ of 4-MBA molecules. The less intense peak observed at 1138 cm^{-1} was assigned to the C-H deformation mode. Once compared, the SERS intensities of the 4-MBA molecules were observed to decrease gradually as Au content in the Au-Ag nanorod films was increased by increasing the Au sputtering power. This is because of the diminishing electromagnetic enhancement effect resulting from the increasing Au content and decreasing Ag content in the Au-Ag alloyed nanorods. Previous studies also claimed similar observations and suggested that the SERS enhancement observed from the Au-Ag alloyed structures is highly dependent on the ratio between the Au and Ag in the substrate (Fan et al., 2013). Thus, the Au-Ag alloyed nanorod substrates obtained at 10 W Au sputtering power, for which highest SERS enhancement was observed in our studies, were selective for the further experiments.

Figure 4.12

Raman Spectra of 10^{-4} M 4-MBA on the Au-Ag Alloyed Substrates Fabricated With 10, 30 and 50 W Au Sputtering Power.



4.2.2 Selective Etching of the Au-Ag Alloyed Substrates

4.2.2.1 HNO₃ Acid Etching. In this study, we investigated the dealloying of the Au-Ag alloyed nanorod films by treating them with HNO₃ solution to selectively remove Ag metals from the alloy template. The Au-Ag alloyed substrates (10 W Au & 80 W Ag) were dipped into HNO₃ solution with various concentrations of 10, 15, 20 and 25% for 5, 10 and 15 minutes. For the higher HNO₃ concentrations (20 & 25%), the Au-Ag alloyed films were observed to peel off from the Si base within 1 minute of immersion. At 15% HNO₃ concentration, the Au-Ag alloyed films were found to be stable up to about 5 minutes of immersion but observed to peel off when immersion time was increased beyond 5 minutes. These observations indicated that at higher HNO₃ concentrations the reaction between Ag and HNO₃ as explained in equation 4.3 earlier occurs very quickly making it difficult to control the etching process. At 10% HNO₃ concentration, we observed a relatively slow etching of the Au-Ag films and films were stable until about 15 minutes of immersion.

Figure 4.13 illustrates the morphology of the Au-Ag alloyed substrates before and after etching with 10% HNO₃ solution from 5 to 15 minutes. For etched samples, the nanorods showed change in their structure showing coalescence resulting in smoother surfaces. EDS analysis revealed that the Au and Ag content in the etched substrates were not significantly changed after the etching process (Table 4.5).

Figure 4.13

SEM Micrographs of Au-Ag Alloyed Substrates (a) Before and (b-d) After Etching With 10% HNO₃ Solution at Different Etching Times of 5, 10 and 15 Minutes, Respectively.

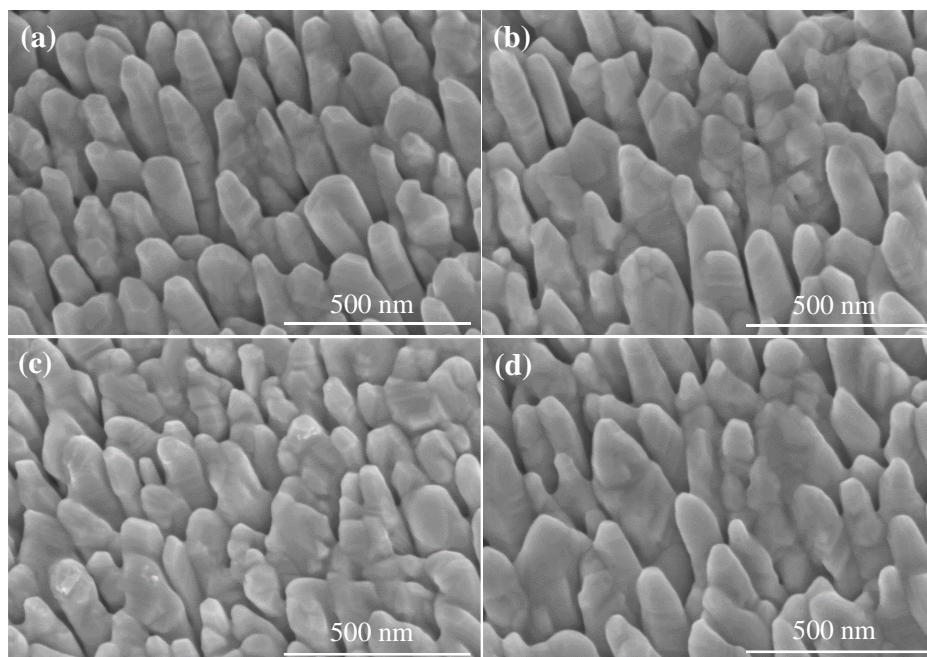


Table 4.5

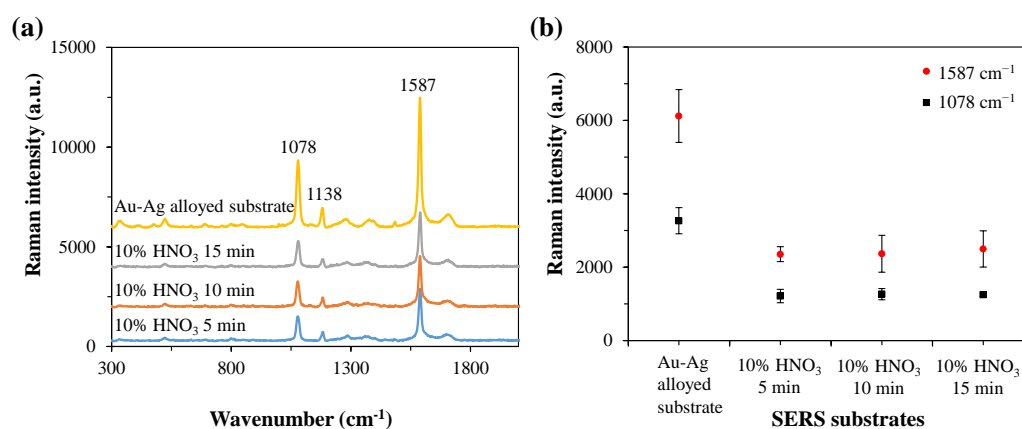
Elemental Composition of the Au-Ag Alloyed Substrates Fabricated by the Co-sputtering Method and After Etching With 10% HNO₃ Solution Upto 15 Minutes.

10% HNO ₃ etching time (minutes)	Weight (%) ± SD	
	Ag	Au
0	91.00 ± 0.17	9.00 ± 0.17
5	90.35 ± 0.13	9.65 ± 0.13
10	91.12 ± 0.13	8.88 ± 0.13
15	92.27 ± 0.13	7.73 ± 0.13

Raman spectra of 10^{-4} M 4-MBA on the Au-Ag alloyed substrates were shown in Figure 4.14. Comparing the two main characteristic peaks of 4-MBA at 1078 and 1587 cm^{-1} , we found that the Au-Ag alloyed substrates before etching generated the highest SERS signal. Upon etching, a significant drop in the 4-MBA Raman peak intensities was observed due to the formation of smoother surfaces as seen in the SEM micrographs above. Similar observations have been made by other researchers as well suggesting that the coarsening of the Au-Ag alloyed nanorods upon etching reduces the density of the nanorods and increases the gaps between them resulting in reduced SERS enhancement (Mun et al., 2019).

Figure 4.14

(a) SERS Intensity of 10^{-4} M 4-MBA on the Au-Ag Alloyed Substrate With 10% HNO_3 Etching for 0-15 Minutes and (b) Dependence of the Dealloying Time and Raman Intensities at Characteristic Peaks of 1078 and 1587 cm^{-1} of 10^{-4} M 4-MBA.

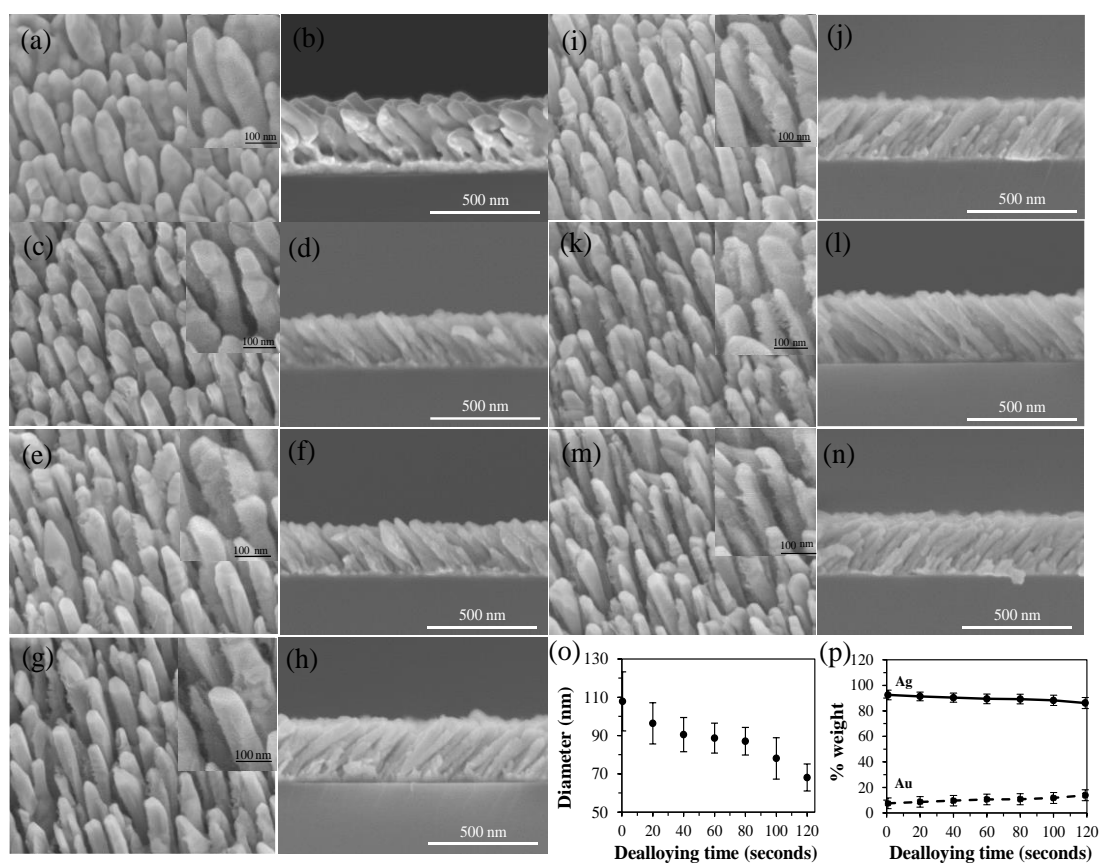


4.2.2.2 30% H_2O_2 : 30% NH_4OH : Methanol Etching. Figure 4.15 (a-n) shows surface and cross-section SEM images of Au-Ag alloyed/dealloyed substrates of various etching times starting with 0 (control) up to 120 s and at an interval of 20 s in 30% H_2O_2 : 30% NH_4OH : methanol solution. All Au-Ag alloyed nanorods showed a 45 degree tilt from the normal with respect to substrates, which is a consequence of the OAD sputtering procedure. Variations in surface roughness were detected as a function of etching time. Roughened areas were detected on Au-Ag dealloyed nanorods on the side nearest to the Ag sputtering target, the left side of the nanorods

in images (Figure 4.15 (c-n)), compared to Au-Ag alloyed samples (Figure 4.15 (a-b)). This is most likely due to the asymmetrical arrangement of the Au and Ag sputtering targets.

Figure 4.15

Surface and Cross-sectional SEM Images of Au-Ag Alloyed Substrates With Different Dealloying Times: (a-b) Au-Ag Alloyed Substrate (0 s), (c-d) 20 s, (e-f) 40 s, (g-h) 60 s, (i-j) 80 s (k-l) 100 s and (m-n) 120 s. The Change in Nanorod Diameter and Content (% weight) of Ag and Au With Increasing Dealloying Time is Graphically Depicted in (o) and (p) Respectively.



The average diameter of the control (unetched) sample was 108 ± 15 nm. With etching or dealloying, the overall nanorod diameter decreased from 108 nm to 68 nm (a decrease of nearly 40 nm in diameter) as the dealloying or etching time was increased from 0 to 120 s, respectively, as shown in Figure 4.15 (o). EDS analysis revealed a decrease in Ag mass percent and a relative increase in the Au mass percent

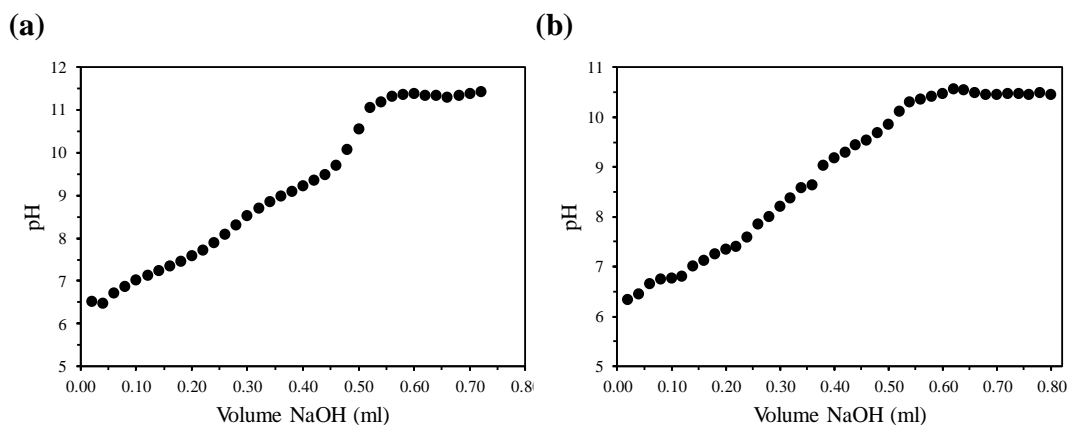
as etching time was increased from 0 to 120 s. These trends are depicted graphically in Figure 4.15 (p). The percent mass of Ag decreased from 92.5 for the unetched sample to 91.4, 90.4, 89.4, 89.2, 88.3 and 86.2% respectively. In contrast and concomitantly, Au content percent increased from 7.5 for the unetched samples to 8.6, 9.6, 10.6, 10.8, 11.7 and 13.8 respectively as etching time was increased from 0 to 120 s. The SEM images also show that the etching process enabled the formation of roughened or protruded surface structures (see insets in Figure 4.15) on the Au-Ag alloyed substrates.

4.2.3 4-MBA Detection

Au-Ag dealloyed substrates (40 s etching) have been shown by SEM to have enhanced surface roughness. Quantitative determination of the number of 4-MBA molecules adsorbed on the substrate supported these SEM results (Figure 4.16). From the curve, we can calculate number of 4-MBA molecules adsorbed on the Au-Ag alloyed substrate to be approximately 6.1×10^{16} molecules. On the other hand, the number of 4-MBA molecules adsorbed on the Au-Ag dealloyed substrate was found to be 4.1×10^{17} molecules (calculation in Appendix A). Therefore, the dealloyed substrate had a greater number of adsorbed 4-MBA molecules on the surface more than on the alloyed substrate—roughly an order of magnitude higher. Corresponding to XPS result, the dealloyed surface provided more gold content that can bind with the thiol group of 4-MBA, thus resulting in an increase of molecules adsorption over the dealloyed substrate.

Figure 4.16

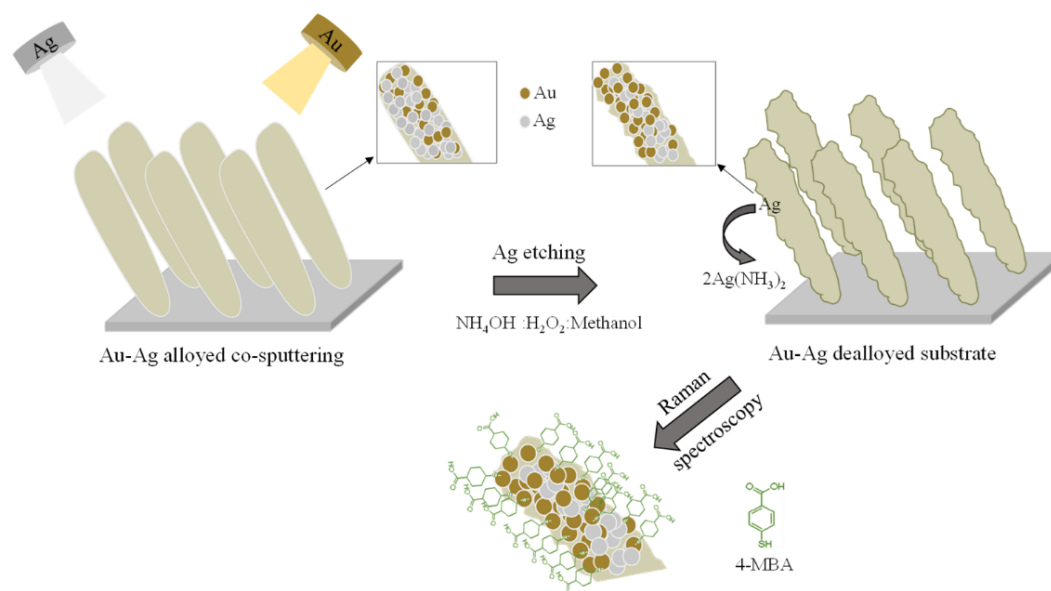
Titration Curve of 4-MBA Titrated With Strong Base (NaOH) of Au-Ag Alloyed Substrate (a); and (b), for the Au-Ag Dealloyed Substrate.



The dealloying process can be described as shown in Figure 4.16. The process starts with a dissolution of Ag atoms into the etchant solution in the form of silver ammine ion (equation 4.4), leaving behind the gold atoms with no lateral coordination on the alloy surface. These gold atoms then diffuse and rearrange on the crystal lattice and agglomerate into islands forming the locally passivated pure gold clusters. Consequently, the continuous dissolution process induces formation of a porous, rough and enhanced surface area substrate (Erlebacher et al., 2001). The gold islands on the dealloyed substrates formed due to the Au atoms rearrangement potentially bind the 4-MBA molecules through the Au-S thiol functional group on the surface, as depicted in Figure 4.17.

Figure 4.17

Schematic Representation Describing the Dealloying Process of the Au-Ag Alloyed Substrates Prepared by Co-sputtering Deposition Method in $\text{NH}_4\text{OH}:\text{H}_2\text{O}_2$:Methanol Etching Solution.



Note. The selective dissolution of Ag atoms induces rearrangement of gold atoms on the dealloyed surface forming tiny Au islands and facilitates more 4-MBA molecules absorption through the Au-S thiol binding.

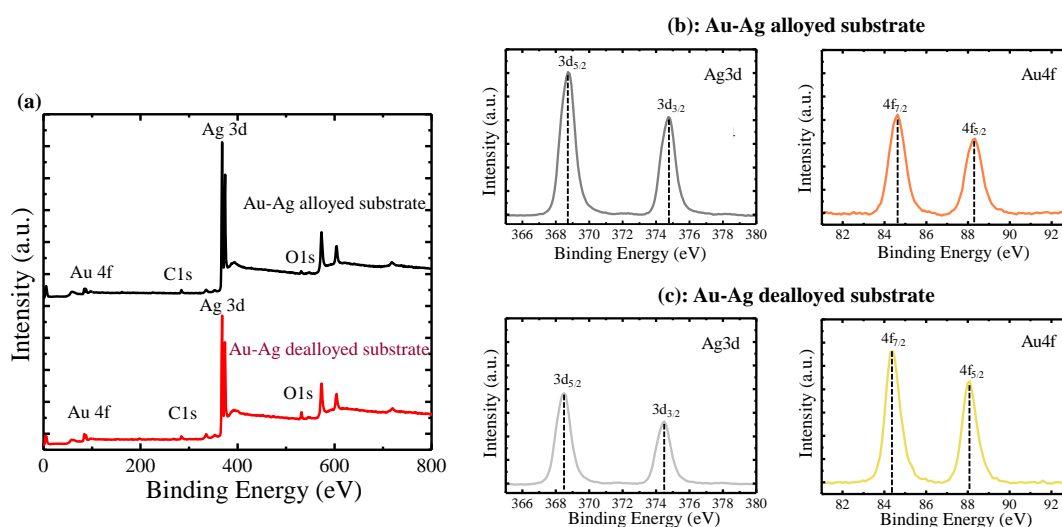
4.2.4 Surface Chemical Composition of the Substrates

The XPS measurements were performed to investigate the surface composition of the Au-Ag alloyed and dealloyed substrates. As shown in Figure 4.18 (a), the surface chemical composition spectra of the prepared Au-Ag alloyed and dealloyed (for 40 s-etching time) substrates indicated typical Ag, Au, C and O signals. The peaks at 368.7 and 374.7 eV in a high-resolution XPS spectrum of Au-Ag alloyed substrate, shown in Figure 4.18 (b), can be assigned to the Ag 3d_{5/2} and 3d_{3/2} of the binding energy of metallic Ag state, respectively, while other two peaks at 88.3 and 84.6 eV can be assigned to the Au 4f_{7/2} and 4f_{5/2} of metallic Au state, respectively. The binding energies exhibit shifts from the pure metallic Au and Ag state compared with the previous reports (Sangpour et al., 2007, 2009) (Ag 3d 5/2 = 368.0-368.3 eV, Au4f_{5/2} = 84.0 eV). This indicates that Au and Ag metals composed in the prepared substrates are forming an alloy phase. After the dealloying process, the binding energies of Ag

$3d_{5/2}$ and $3d_{3/2}$ peaks shifted to 368.4 and 374.4 eV, respectively, while the binding energies of Au $4f_{7/2}$ and $4f_{5/2}$ peaks shifted to 88.1 and 84.4 eV, respectively as shown in Figure 4.18 (c). The exhibited binding energy shifts of both Ag and Au peaks of dealloyed sample can be attributed to the change in alloy composition during etching. In more detail, the relative atomic concentration of Au after the dealloying increased from 2.9 to 5.7%, which is calculated by deconvolution of the Au peak area, showing improved Au passivation of the substrate surface. Importantly, no peak corresponding to AgO at 367.4 eV was observed in the XPS spectra after dealloying process, indicating no oxide formation on the surface that could deteriorate SERS performance of the substrate.

Figure 4.18

(a) The Complete XPS Spectra of Au-Ag Alloyed and Dealloyed Substrates. (b) Main Peaks of Ag 3d and Au 4f of the Au-Ag Alloyed Substrates and (c) Au-Ag Dealloyed Substrates.



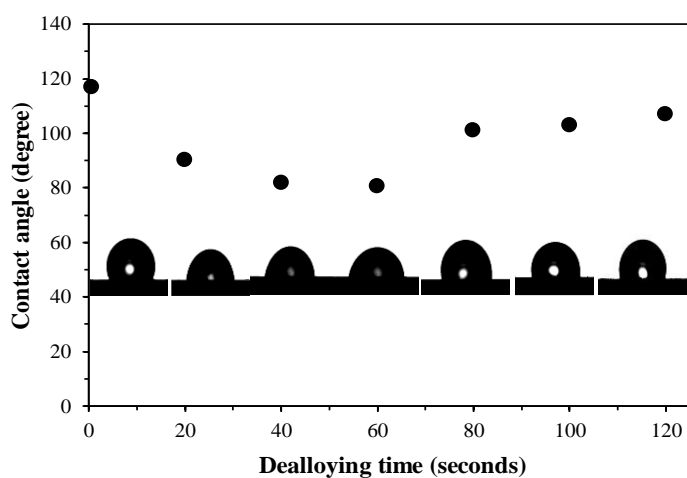
4.2.5 Surface Wettability of the Substrates

The water contact angle (WCA) measurement of Au-Ag alloyed substrate (before etching) and Au-Ag dealloyed substrate with various etching times are graphically depicted in Figure 4.19. The graph shows that average water contact angle of the initial Au-Ag alloyed substrate was about $117^\circ \pm 0.8$, indicating a hydrophobic surface. Samples etched for 20 s exhibited an average contact angle of $90.2^\circ \pm 0.1$.

For 40 s and 60 s etch time samples, the surfaces assumed more hydrophilic character displaying WCA of $81.8^\circ \pm 0.1$ and $80.4^\circ \pm 0.3$ respectively. However, when etching time was increased to 80, 100 and 120 s, WCA slipped back, but barely, into the hydrophobic domain giving values of $101^\circ \pm 0.1$, $103^\circ \pm 0.1$, and $107^\circ \pm 0.2$ respectively. Previous studies have reported that Ag or Au based thin films with oblique structure have shown borderline to hydrophobic character with contact angles ranging from 90.0° to 120° (Siabi-garjan, 2019, Kumar, 2014). This increase in hydrophobicity from the 60 s etch time sample to the 120 s etch time sample can be explained by the decrease in surface energy, this time due to increasingly smaller diameter nanorods. Although the number of nanorods remained constant following etching, two physical changes occurred: (1) The spaces between nanorods was increased; and concomitantly, (2) the amount of surface available to contact liquid water was decreased. These changes result in an increase in the area fraction of the trapped air beneath the water droplet leading to increased contact angle (Khudhayer et al., 2009).

Figure 4.19

The Water Contact Angle and Drop Profile of Au-Ag Alloyed Substrate (Before Etching) and Au-Ag Dealloyed Substrate With Different Dealloying Times are Depicted.



Note. Two Trends are Apparent: a trend towards hydrophilicity from 0 s to 60 s, followed by another trend back towards hydrophobicity from 60 s to 120 s of etching time.

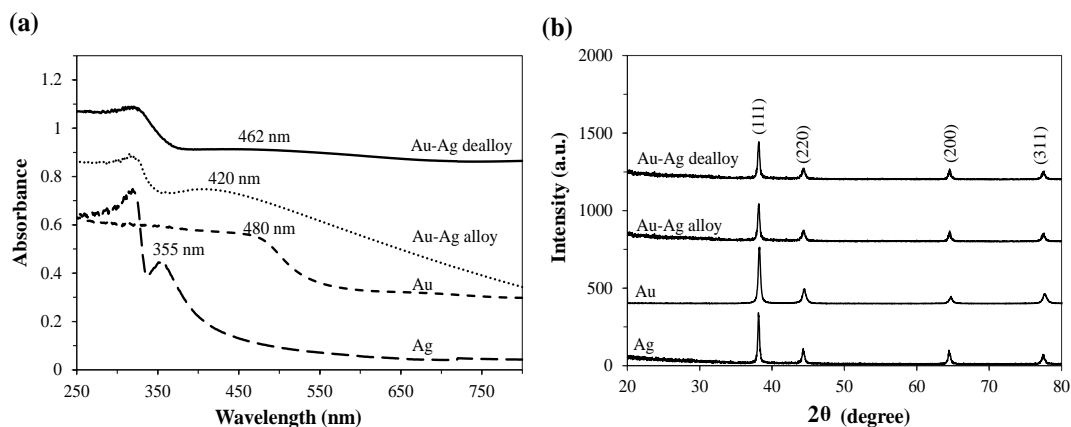
4.2.6 Optical and Crystallographic Properties of the Substrates

The UV-visible absorption spectra of the Au-Ag alloyed and Au-Ag dealloyed substrates were characterized and compared with pure Au and Ag nanorods as shown in Figure 4.20 (a). All nanorods exhibited their characteristic plasmon absorption peaks. The Au-Ag alloyed and Au-Ag dealloyed substrates showed broad absorption peaks at 420 and 462 nm—both located at intermediate positions between the absorption of 355 nm and 480 nm for pure Ag and Au films, respectively (please refer to Appendix B for information regarding fabrication method and physical form). Au-Ag alloyed nanomaterials are expected to have plasmon absorption maxima in between those of the pure substances based on simulations with Bruggeman effective medium theory (Hornyak et al., 1997). By comparing with the alloyed nanorod substrates, the absorption peak of the Au-Ag dealloyed substrate is red-shifted from 420 nm to 462 nm due to depletion of Ag in the alloyed material following etching. However, the absorption is still mostly dominated by the Ag due to its higher absorption coefficient and content in the structure.

XRD patterns of Ag, Au, Au-Ag alloyed and Au-Ag dealloyed substrates are depicted in Figure 4.20 (b). Both Au-Ag alloyed and Au-Ag dealloyed substrates showed intense peaks at diffraction angles 2θ equal to 38.2° , 44.3° , 64.5° and 77.6° . This profile is similar to those associated with pure Ag and pure Au. These peaks corresponded to (111), (220), (200) and (311) planes, characteristic of a face centered cubic structure for natural Ag and Au crystallites (Godipurge et al., 2016). Based on the Scherrer equation, crystallite sizes were estimated to be on the order of 24 and 26 nm respectively for the alloyed and the 40 s dealloyed samples, respectively. Please note that Au and Ag have similar crystalline structure due to their similarity of lattice constants (Ag = 4.086 \AA , and Au = 4.078 \AA), which makes it difficult to identify the individual XRD phases in the alloyed and dealloyed samples (Xia et al., 2013; Yu et al., 2017).

Figure 4.20

(a) UV-Visible Absorption Spectra and (b) XRD Patterns of Pure Au, Pure Ag, Au-Ag Alloyed Nanorods and 40 s Etched Au-Ag Dealloyed Nanorod Samples are Depicted.



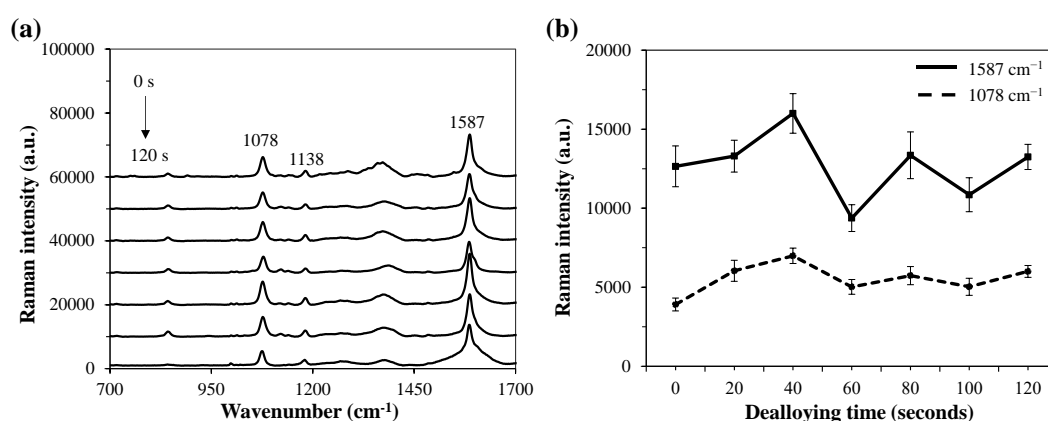
4.2.7 Raman Characterization

Raman characterization was conducted using 4-MBA as the probe molecule on the Au-Ag dealloyed SERS substrates with different etching times (0-120 s). Regardless of etching times, Raman spectra of 4-MBA showed two main peaks at 1078 and 1587 cm^{-1} as shown in Figure 4.21 (a), that are characteristic of aromatic ring breathing modes. The other less intense mode at 1183 cm^{-1} corresponded to C-H deformation and the broad peak at 1390 cm^{-1} is due to COO^- stretching (Ho & Lee, 2015). In Figure 4.21 (b), the peak intensities of the two characteristic Raman peaks of 4-MBA molecules were shown with respect to the etching or dealloying time, where highest intensity peaks were observed at the etching time of 40 s. The 40 s etching time was therefore selected as the optimal condition for sample preparation. Interestingly, a strong case cannot be made for statistical significance between and among 0, 20, 80, 100 and 120 s sample intensities due to the small variations in terms of the Raman intensities. However, SEMs (Figure 4.15) indicated that nanorods etched for 40 s possessed the greatest roughness. In this case, 40 s dealloyed SERS substrates achieved optimal structural configurations regarding high surface roughness that resulted in generation of hot spots during Raman measurements (Chao et al., 2017; Wiriyakun et al., 2016). The case of the 60 s etched substrate is more difficult to rationalize. The 60 s substrates demonstrated the lowest intensities of all samples.

Considering WCA data, it demonstrated a similar trend with the 40 s sample due to the introduced hydrophobic property of samples after 60 s etching time. However, EDS analysis (Figure 4.15 (p)) suggests that the Ag content in the 60 s sample is lower than the 40 s sample resulting in decreased SERS signal (Miele et al., 2014).

Figure 4.21

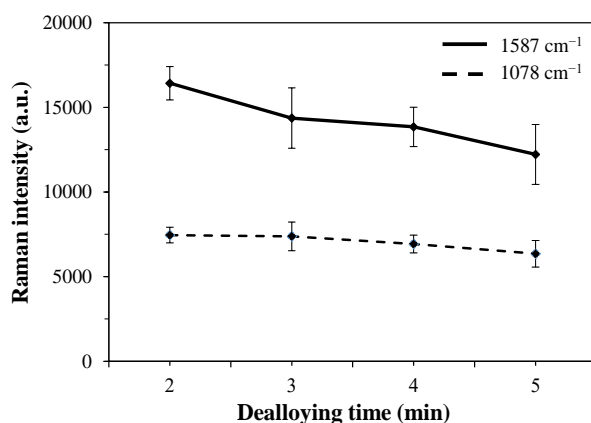
(a) SERS Spectra of 10^{-4} M 4-MBA on the Au-Ag Dealloyed SERS Substrates for Different Etching Times 0, 20, 40, 60, 80, 100 and 120 s From Top-to-bottom. (b) Raman Intensities of 4-MBA at Characteristic Peaks of 1587 cm^{-1} and 1078 cm^{-1} Derived From Spectra Depicted in (a).



The 30% H_2O_2 : 30% NH_4OH : methanol etching solution used in our study was a strong oxidizing agent and it reacts quickly with the Au-Ag substrate. To see the effect, we indeed performed etching of our substrates for a longer time duration up to 5 minutes. However, in terms of SERS performance, we found significant drop in the signal intensity with the substrates etched beyond 120 s, along with higher standard deviations in the results. We, therefore, considered etching time up to 120 s for our remaining experiments. These results are shown in Figure 4.22.

Figure 4.22

Raman Intensities of 4-MBA at Characteristic Peaks of 1587 cm⁻¹ and 1078 cm⁻¹ for Different 30% H₂O₂: 30% NH₄OH: Methanol Etching Time 2-5 Minutes.



It was remarkable that increased etching time, wherein Ag particles were selectively etched away from the alloyed nanorods, resulted in decreasing signal since Ag technically has a stronger Raman interaction. Plasmonic properties of Ag, Au and Au-Ag alloy structure and the calculation on the electromagnetic field distribution by previous reports demonstrated that Ag exhibits a stronger electric field than Au-Ag alloy and Au metals. Therefore, the plasmonic resonance of materials is not only generated from the coupling effect but the surface roughness on the dealloyed substrate as well, since the rough plasmonic film exhibit intense and abundant hotspot originated by the coupling of propagating and localized surface plasmons (Lee et al., 2015; Macias et al., 2016).

4.2.8 Sensitivity Measurements

Sensitivity of the Au-Ag alloyed and dealloyed (40 s etching time) substrates was examined by collecting Raman spectra of 4-MBA at concentrations in the range of 10⁻⁴-10⁻⁹ M as shown in Figure 4.23 (a-b). The intensities of these SERS substrates also were evaluated at the characteristic peaks of 1587 cm⁻¹ (Figure 4.23 (c)) and 1078 cm⁻¹ (Figure 4.23 (d)) respectively. Comparing SERS signals, the 40 s etched sample Au-Ag dealloyed substrates provided higher SERS signals than that of Au-Ag alloy substrates at all concentrations. The Raman signal was distinctive until 10⁻⁹ M on the Au-Ag dealloyed substrate while on the alloyed substrate, detection limit

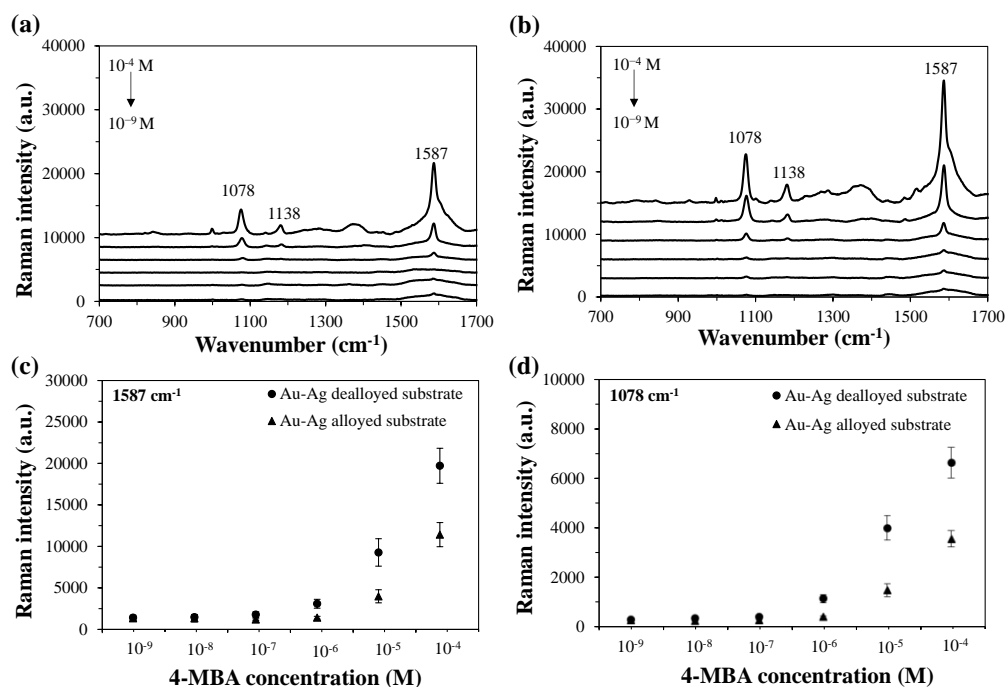
was ten times less at 10^{-8} M. The calculated signal to noise ratio was greater than three for both characteristic peaks. From this result, the dealloyed structure etched for 40 s with enhanced surface roughness improved SERS signal at least one order of magnitude over the alloyed SERS substrates and was capable of detecting 4-MBA at nM concentrations.

The EF was then calculated, which is described as the intensity ratio between SERS and normal Raman scattering for a given analyte normalized by the number of molecules probed. The EF normally is used to estimate the effectiveness of the SERS substrate and can be calculated with a conventional method using the equation 3.1.

Based on the intensities of diagnostic peaks at 1078 cm^{-1} of 10^{-4} M 4-MBA, EF was found to be 1.5×10^6 for Au-Ag dealloyed substrate and 4.6×10^5 for the Au-Ag alloyed substrate (The detailed calculation is given in the Appendix C). The EF of Au-Ag dealloyed substrate is similar to values reported in previous work that also studied Au-Ag dealloyed substrates based on a similar sputtering technique (Hu et al., 2019; Huang et al., 2017) and other synthesis methods (See in Table A1 in Appendix C). The differences in structure and metal composition of SERS substrates have certain impacts on SERS enhancement. As it is widely known, two main SERS enhancement mechanisms contribute to enhancing detection signals: (1) Electromagnetic enhancement (EM) which involves near-field coupling of localized surface plasmon resonance (LSPR); and (2) Chemical enhancement (CM) caused by interactions between the metal surface and the target molecule by means of charge transfer interactions. However, increasing surface roughness by selective etching of Au-Ag alloyed substrates is capable of augmentation of both EM, via generation of greater numbers of hotspots, and CM, via higher surface area for adsorption. In this study, the improved SERS enhancement of the Au-Ag dealloyed substrate originated from the combination of the surface roughness and the complex effect of functional group on gold surface leading to both EM and CM mechanism.

Figure 4.23

Raman Spectra of 4-MBA Molecules With Concentration Ranging From 10^{-4} to 10^{-9} M Absorbed (a) on the Au-Ag Alloyed Substrates (Before Etching) and (b) on the Au-Ag Dealloyed Substrates (40 s Etching). SERS Intensity of the Characteristic 4-MBA Raman Bands on the Alloyed and Dealloyed Substrates at (c) 1587 cm^{-1} and for (d) 1078 cm^{-1} as a Function of 4-MBA Concentrations.



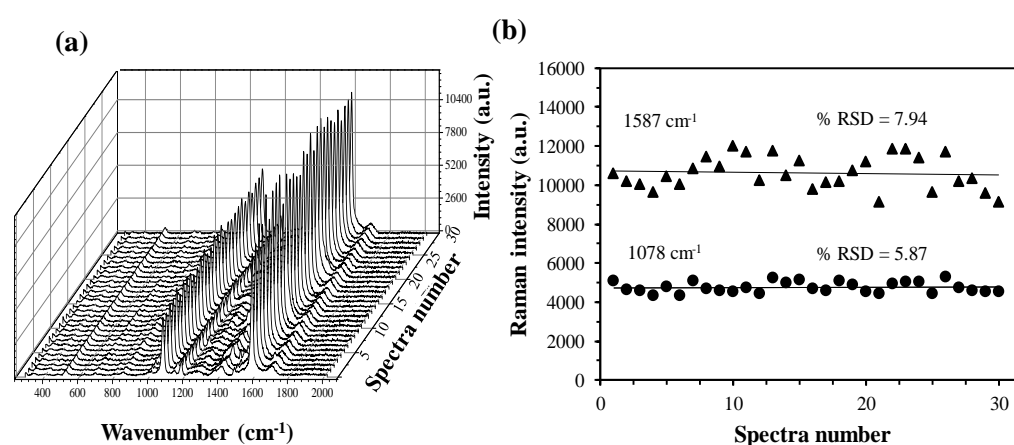
4.2.9 Reproducibility and Reliability

Uniformity and reproducibility are common issues of SERS substrates. For practical applications, it is important that the designed structures are able to provide reliable and reproducible spectra. In this study, SERS spectra of 10^{-4} M 4-MBA on the Au-Ag dealloyed substrate with 40 s etching were collected from 30 different mapping areas (the measurement area is $120 \times 100\ \mu\text{m}^2$) and then calculated percent relative standard deviation (%RSD) served as an estimate of uniformity (Figure 4.24 (a-b)). %RSD of the Au-Ag dealloyed substrate was 5.87 and 7.94 at characteristic peaks of 4-MBA at 1078 and 1587 cm^{-1} respectively. For reproducibility, Au-Ag dealloyed substrates were fabricated from three different batches resulting in %RSD of 11.6 and 9.3, respectively, also calculated from two main characteristic peaks of 4-MBA. Based on the synthesized sputtering technique, the size distribution of nanorods is

much broader compared to the periodic structure of the arrays that were fabricated by AAO template-assisted co-electrodeposition by other researchers. However, such AAO-based structure provided RSD of 6.5% (Chen et al., 2014) which is comparable to our results. In addition, variation of the dealloyed structure still presents in a range of acceptable value (less than 10-15%) corresponding with previous reports of SERS substrate fabrication (Bekana et al., 2016; Liu et al., 2014; Syu et al., 2018). Considering these literatures, the as-prepared Au-Ag dealloyed substrate has shown relatively good uniformity and reproducibility.

Figure 4.24

(a) SERS Spectra of 10^{-4} M 4-MBA Collected From 30 Different Spots on the Au-Ag Dealloyed Substrates. (b) Raman Intensities of 30 Spectra at Wavenumber of 1587 cm^{-1} and 1078 cm^{-1} .



4.2.10 Long Term Performance

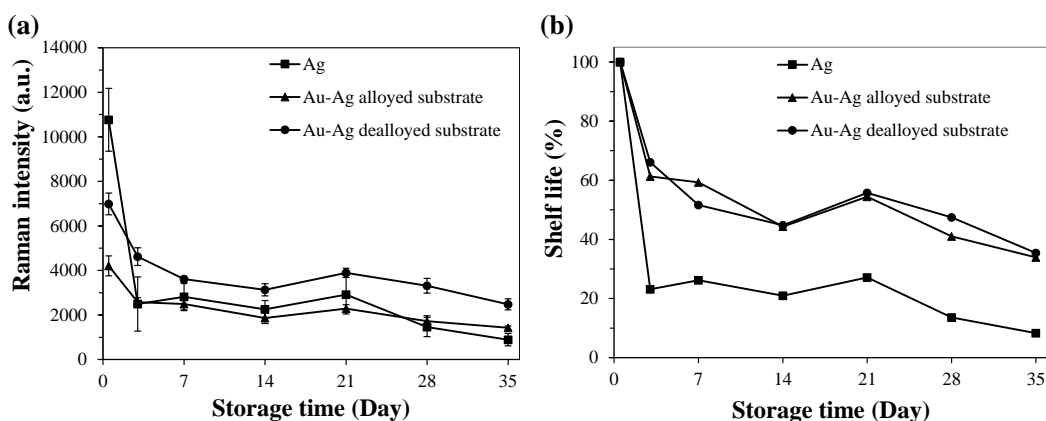
Besides SERS sensitivity, the long term performance of the Au-Ag alloyed substrate and the Au-Ag dealloyed substrate were studied and compared with pure Ag substrates. In this study, freshly synthesized substrates were exposed to ambient conditions for a month. 4-MBA molecules were dropped on the surface substrate before Raman measurement at 0, 3, 7, 14, 21, 28 and 35 days. Raman intensity of 4-MBA at a characteristic peak of 1078 cm^{-1} was measured until 5 weeks (Figure 4.25). The results indicated that the signal from the pure Ag substrate was higher than the Au-Ag alloyed and the dealloyed substrate around 2.5 and 1.5 times respectively at

day 0. Then, the signal from pure Ag dramatically decreased to 23% within 3 days and remained only at 8% after 35 days.

Meanwhile, the signal from the Au-Ag alloyed and the dealloyed substrates gradually decreased to around 60% at day 3 but still demonstrated a robust signal strength at around 35% for the duration of 35 days. Comparing to pure Ag, the aged alloyed and dealloyed substrate had better performance for longer lifetimes due to the presence of Au metal. There were no significant differences in lifetimes between the alloyed and the dealloyed SERS substrates. The degradations of these substrates were found to be similar due to only small changes in gold and silver contents following etching. It is well known that the stability depends on gold content. According to the previous reports, the porous Au-Ag hybrid structure provide a stable SERS signal of about 70% within 20 days due to high gold content of 80% (Li et al., 2019). Besides a small change in gold surface, such structures could be observed on only one side of the alloyed nanorods, so rearrangement of Au atoms also occurred at specific sites and partially prevent the formation of silver oxide.

Figure 4.25

SERS Signal of 10^{-4} M 4-MBA at 1078 cm^{-1} Characteristic Peak on Pure Ag, Au-Ag Alloyed and Au-Ag Dealloyed Substrates for 35 Days.



4.3 Urinary Crystal Detection Using Au-Ag Dealloyed Substrate

In this part, we investigated the Au-Ag dealloyed SERS substrates for the potential detection of urinary crystals in synthetic urine samples. The substrates were

fabricated by the co-sputtering method and subsequently etched in 30% H₂O₂: 30% NH₄OH: methanol solution for 40 s to obtain an ordered dealloyed nanorods structure with enhanced surface roughness (as described in the section 4.2.2.2). At first, the as-prepared substrates were used to identify SERS spectra of urinary crystals; calcium oxalate monohydrate (COM), calcium phosphate (CAP) and uric acid in aqueous solution. Then, to examine the sensitivity of detection, uric acid crystals were dissolved in DI water and in 1% synthetic urine with concentration of 10⁻⁷-10⁻³ M.

4.3.1 Crystals Dissolved in Deionized (DI) Water

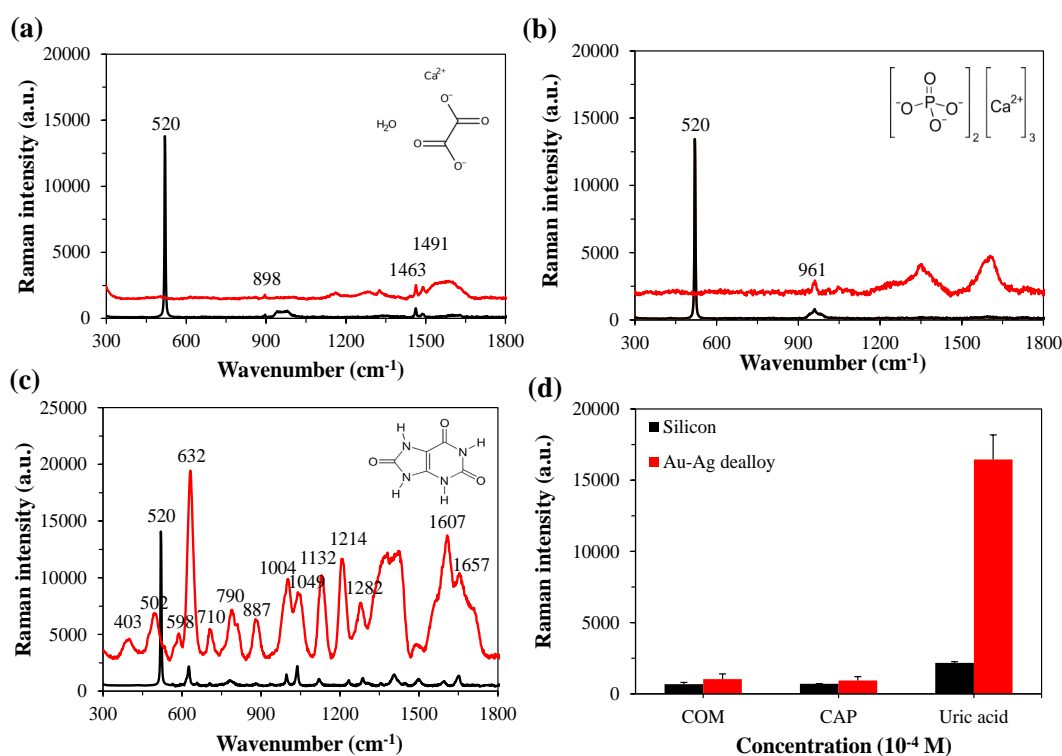
To verify the efficiency of as-prepared SERS substrate for the urinary crystal detection, Raman spectra were collected and compared with bare silicon substrates. The Raman spectra of 10⁻⁴ M COM, CAP and uric acid on the Au-Ag dealloyed substrates and silicon wafer were shown in Figure 4.26. The silicon substrate generated a predominant peak at 520 cm⁻¹ that assigns to the crystalline silicon, a less intense peak at 898 cm⁻¹ that is assigned to O-C-O in plane bending for the COM and two main characteristic peaks of COM at 1463 and 1491 cm⁻¹ belongs to the C-O symmetric stretching as shown in Figure 4.26 (a) (Frausto-Reyes et al., 2014; Hug et al., 2012). In Figure 4.26 (b), the characteristic vibration of CAP showed a strong peak at around 961 cm⁻¹ and less intense peak at 1046 cm⁻¹ that originate from symmetric and antisymmetric stretching of phosphate group. (De Aza et al., 1997). As shown in Figure 4.26 (c), the uric acid distinctly presented the spectrum at characteristic bands of 502, 632, 764, 887, 1004, 1132, 1214, and 1607 cm⁻¹. The peak at 502 cm⁻¹ is due to the C-N bending/in-plane ring deformation. The intense peak of 632 cm⁻¹ belongs to skeletal ring deformation. The peak at 764 cm⁻¹ is probably due to the out-of-plane N-H bending/ring vibration and the peak at 887 cm⁻¹ arises from the N-H in-plane bending. The peak at 1004 cm⁻¹ is attributed to the C-N stretching/ring vibrations and the band at 1132 cm⁻¹ is a mixed vibration of C-O, C-C, C-N ring vibration, C-N stretching/mixed modes and at 1214 cm⁻¹ corresponds to in-plane N-H bending. The last peak at 1607 cm⁻¹ is attributed to C=O stretching of uric acid molecule (Pucetaite et al., 2016; Villa & Poppi, 2016).

The assignments of spectral bands of all crystals are presented in Table A3 Appendix. To compare the SERS performance between the dealloyed and silicon substrate, only main characteristic peak of each crystal was plotted as an intensity that are shown in

Figure 4.26 (d). The intensity of COM, CAP and uric acid deposited on the dealloyed substrate was increased approximately 1.5, 1.3 and 7.6 times as compared to the silicon substrate. Considering water solubility among these three crystals, uric acid is 60 mg/L at 20 °C while COM and CAP have a lower soluble potential at 0.67 mg/L and 20 mg/L (NIST, 2012). This supports the result that more water solubility of uric acid is coherence with small crystallite size and is explicit in its identifiable SERS signals on the Au-Ag dealloyed substrate. Because of the higher SERS intensities, uric acid is then selected to study in further experiments.

Figure 4.26

SERS Spectrum and Chemical Structure of (a) 10^{-4} M Calcium Oxalate Monohydrate (COM), (b) Calcium Phosphate (CAP) and (c) Uric Acid Dispersed in DI water on the Au-Ag Dealloyed and Bare Silicon Substrates. (d) The Comparison Between SERS and Raman Intensity of the Main Characteristic Peaks at 1463, 961, and 632 cm^{-1} Corresponding to COM, CAP, and Uric acid, Respectively Substrates.



4.3.2 Uric Acid Dissolved in DI Water

SERS spectra of uric acid at various concentrations varied in the range of 10^{-7} - 10^{-3} M is shown in Figure 4.27 (a). At concentrations of 10^{-3} and 10^{-4} M, all characteristic peaks of uric acid were clearly visible. Considering only at main characteristic peaks at 632, 1132 and 1214 cm^{-1} , the spectra also exhibited SERS signals down to a concentration of 10^{-5} M. All intense peaks at 632, 1132 and 1214 cm^{-1} were plotted in the linear dependence relationship between intensity of the peaks and the concentration of uric acid in the range of 0 M- 5×10^{-5} M as shown in the inset of Figure 4.27 (b-d). The linear regression analysis yielded R^2 in the range of 0.9754 - 0.9936, indicating a good linear fit. Thus, quantitative detection of uric acid in a concentration range from 0 to 5×10^{-5} M was possible according to this linear relationship. An average detection limit was estimated to be 6.95×10^{-6} M as calculated from the three intense characteristic peaks as summarized in Table 4.6 and using the equation 3.2.

Table 4.6

LOD of Uric Acid Dispersed in DI Water Calculated From the Peaks of 632, 1132 and 1214 cm^{-1}

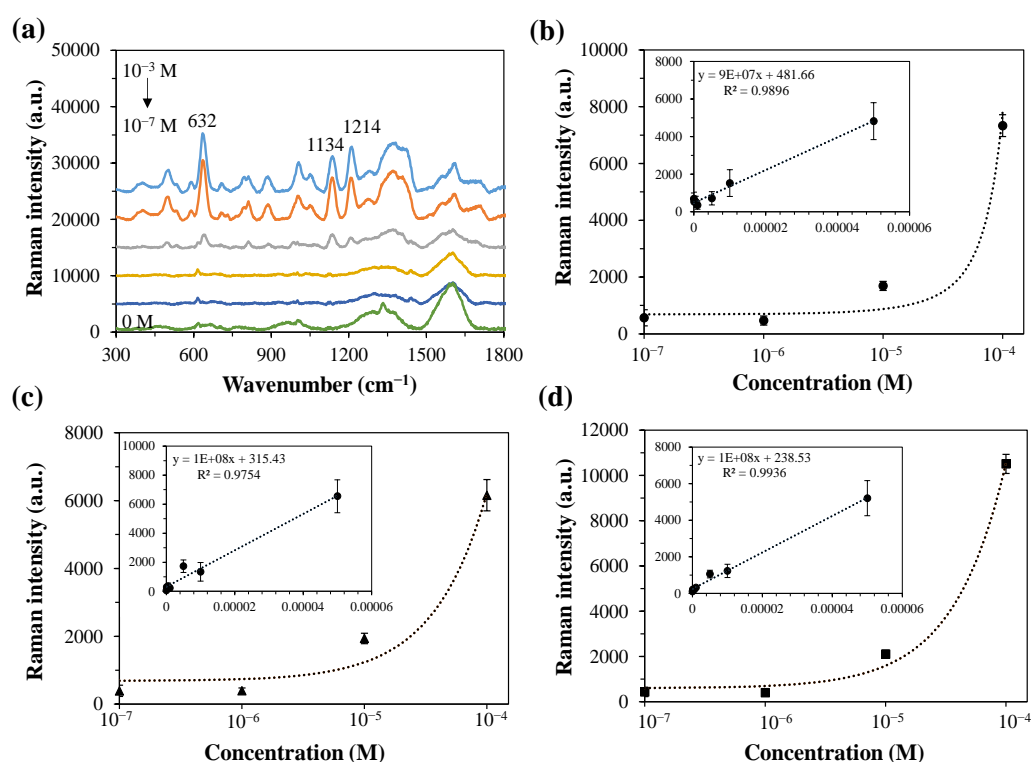
SERS peak (cm^{-1})	Limit of detection (LOD) (M)
632	4.81×10^{-6}
1132	4.22×10^{-6}
1214	1.18×10^{-5}

It is noteworthy that the sensitivity was down to 10^{-6} M on the Au-Ag dealloyed substrate. This is similar to the previous reports as compared in Table (Lu et al., 2018; Pucetaite et al., 2016; Villa & Poppi, 2016). Moreover, in healthy adult, the concentration of uric acid is in a range of 16-100 mg/dL per 24-hour (~ 0.95 -5 mM) in urine (Feig et al., 2006). Thus, the detection limit of this study shows promise for trace level uric acid detection in urine. Such a good efficiency may be obtained from a periodic nanorods structure with surface roughness. It is well known that surface

roughness introduces a high density of SERS hotspots which generates local field enhancement (Asiala & Schultz, 2011; Lee et al., 2015). The result found that the Au-Ag dealloyed substrates have a potential to detect urinary crystals in aqueous solution as low as 10^{-4} M for COM and CAP and down to 10^{-6} M in uric acid. All these findings suggest an efficient SERS substrate with a high sensitivity that have a potential for medical screening or early diagnosis.

Figure 4.27

(a) SERS Spectrum of Uric Acid Dispersed in DI at Different Concentration of 10^{-7} - 10^{-3} M. The Signal Intensity at Raman Peak of (b) 632 cm^{-1} , (c) 1134 cm^{-1} and (d) 1214 cm^{-1} at Various Concentrations, 10^{-7} M to 10^{-4} M. (Linear Relationship in a Range of 0 - 5×10^{-5} M Shown in the Inset.)



4.3.3 Uric Acid Detection in Synthetic Urine

To evaluate the performance of the Au-Ag dealloyed SERS substrate in uric acid detection in the presence of interference, uric acid was added into 1% diluted synthetic urine at concentrations ranging between 10^{-7} - 10^{-3} M. As shown in Figure 4.28 (a), SERS spectra of uric acid on the Au-Ag dealloyed substrate showed clear

uric acid spectra at all concentrations. An intense peak at 1000 cm^{-1} belongs to urea attributed from N-C-N stretching that is a main component in synthetic urine. To verify the sensitivity, average intensities of the prominent uric acid Raman peaks at 637 , 1139 and 1214 cm^{-1} at uric acid concentrations from 0 M - 10^{-4} M were plotted and shown in Figure 4.28 (b). It was observed that the average intensity linearly increased with the increasing concentration of uric acid in synthetic urine. The linear regression analysis yielded a $R^2 > 0.96$ indicating good linear fitting (as shown in an inset of Figure 4.28 (b-d)) with an average LOD of $1.27 \times 10^{-6}\text{ M}$ calculated from the three intense characteristic peaks as summarized in Table 4.7. As compared to a previous study where gold nanoparticles-coated paper substrates were used, the substrates developed in this study exhibited a higher performance by around two orders of magnitude (Villa & Poppi, 2016).

Figure 4.28

(a) SERS Spectrum of Uric Acid Dispersed in Synthetic Urine at Different Concentration of 10^{-7} - 10^{-3} M. The Signal Intensity at Raman Peak of (b) 637 cm^{-1} , (c) 1139 cm^{-1} and (d) 1214 cm^{-1} at Various Concentrations, 10^{-7} M to 10^{-4} M. (Linear Relationship in a Range of $0-1 \times 10^{-5}$ M Shown in the Inset.)

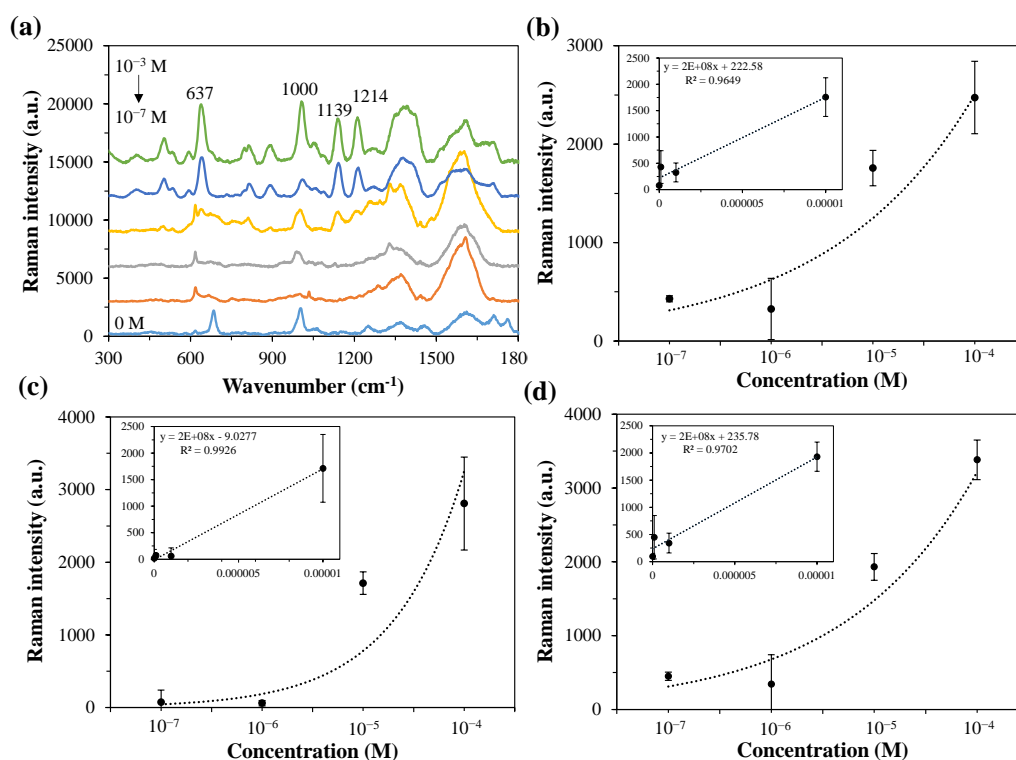


Table 4.7

LOD of Uric Acid Spiked in Synthetic Urine Calculated From the Peaks of 637 , 1139 and 1214 cm^{-1}

SERS peak (cm^{-1})	Limit of detection (LOD) (M)
637	8.63×10^{-7}
1139	2.50×10^{-6}
1214	4.63×10^{-7}

Table 4.8

Summarizes the Performance of Various SERS Substrate for Uric Acid Determination.

Substrate	Detection range (M)	LOD (M)	Reference
AgNPs colloid dropped onto Al ₂ O ₃ surface	10 ⁻⁶ -10 ⁻³	10 ⁻⁶ in DI	(Pucetaite et al., 2016)
Ag colloid dropped onto Ag films	5×10 ⁻⁶ -10 ⁻³	-	(Lu et al., 2018)
AuNPs dropped on paper	0-3.5×10 ⁻³	1.1×10 ⁻⁴ in synthetic urine	(Villa & Poppi, 2016)
AgNPs coated on ZnO/Fe ₃ O ₄	0-1×10 ⁻⁵	-	(Alula et al., 2019)
AgNPs	0-1×10 ⁻⁴	-	(Westley et al., 2017)
AgNPs drop coat on screen printed carbon electrode	-	< 4×10 ⁻⁴ in urine simulant	(Goodall et al., 2012)
Au-Ag dealloyed nanorods	10 ⁻⁷ -10 ⁻³	6.95×10 ⁻⁶ in DI 1.27×10 ⁻⁶ in synthetic urine	This study

CHAPTER 5

CONCLUSION AND RECOMMENDATIONS

5.1 Conclusion

This chapter summarizes the conclusions of Au-Ag nanorods SERS substrate fabrication based on galvanic replacement, co-sputtering and dealloying process. The results of all characterization and application of the prepared substrates also are concluded. The recommendations are described in the last part.

5.1.1 Au-Ag Bimetallic Nanorods via Galvanic Replacement and Dealloying Process

Ag nanorods substrates are successfully fabricated using GLAD sputtering with rotation method. The obtained nanostructured thin film exhibited an ordered columnar nanorod structure with an average diameter approximately 220 ± 55 nm and height around 880 ± 17 nm. The Ag nanorods were then converted to Au-Ag bimetallic nanorods using a spontaneous galvanic replacement method. The conditions of the GRR are varied in terms of the HAuCl_4 concentrations and reaction time. The galvanic replacement of Ag with Au led to a largely roughened surface and maximum roughness was seen at 0.01 wt% HAuCl_4 concentration with replacement reaction time of 3 minutes. The relative weight percent of Au at this condition was around 1.62% while Ag was 98.39%. The as obtained Au-Ag bimetallic SERS substrates contributed higher SERS intensity compared to the pure Ag nanorod substrates because of their increased roughness that enhances the plasmonics hotspots on the substrate causing intense local field enhancement. At higher HAuCl_4 concentrations above 0.1 wt%, deformation of the sacrificial Ag film was observed resulting in agglomeration of Au on the surface.

In order to create more porous structure, dealloying of the Au-Ag bimetallic substrate was carried out using wet etching with nitric acid to selectively etch Ag from the substrate. For nitric acid concentration above 10%, the reaction was found to proceed very quickly resulting in peeling of the Au-Ag bimetallic thin film from the base Si substrate within a few minutes. At 10% nitric acid concentration the reaction was somewhat slow and changes on the surface morphology of the Au-Ag bimetallic substrates was observed at different etching time until 15 minutes. However, no

variations in terms of porosity were observed and the nanorods exhibited coalescence effect resulting in smoother nanostructures and partially formed islands at longer etching time. Relative weight % of the two metals were not significantly changed after etching when compared to the substrate before etching. This indicated that the mild etching reaction of HNO₃ acid introduces only Ag atoms self-diffusion and rearrangement on the surface of the nanostructures due to low dissolution rate of the etchant, leading to a smoother surface. Another selective etching solution for Ag film composed of 30% NH₄OH and 30% H₂O₂ diluted in methanol at a volume ratio of 1:1:4 was used to increase porosity. In this etching process, however, the reaction rapidly occurred to consume Ag and the Au-Ag bimetallic film was completely peeled off from the silicon substrate within 5 s. Therefore, no further attempt was made with this process.

For all the SERS substrates prepared, Raman characterization was carried out using 4-MBA molecule as a Raman probe. 4-MBA Raman spectrum was clearly observed until 10⁻⁸ M on the Ag substrate, while the Au-Ag bimetallic substrate successfully showed spectrum until 4-MBA concentration 10⁻⁹ M, indicating that the fabricated Au-Ag bimetallic substrate composing of enriched Ag metal template and a small amount of Au can provide a higher SERS signal. The signal enhancement is due to the coupling effect with larger SERS hotspots generated from its surface roughness. For the dealloyed samples prepared by wet etching with nitric acid, no SERS enhancement was observed with 4-MBA molecules due to the reduced roughness of the resultant smoother Au-Ag dealloyed substrates.

The long term performance of the Au-Ag bimetallic substrate was then compared with pure Ag substrate by exposing the substrates to the air in ambient conditions over a month. Compared to the pure Ag, the aged bimetallic substrate provided a high performance for long shelf-life. A small amount of deposited Au atoms partially prevents silver oxide formation on the surface and also improves the stability, which helps to maintain the SERS effect for a longer duration. The degradation rate, however, for the two substrates was found similar because of only a small difference in gold content.

5.1.2 Au-Ag Alloyed Nanorods by Co-sputtering Deposition and Dealloying Process

Co-sputtering technique is different from the above method that is based on two processes including sputtering followed by galvanic replacement. This technique can be used to fabricate alloy structures in a single step process and allows to control each metal composition by controlling the input sputtering power. The morphology of the Au-Ag bimetallic alloyed substrate prepared using the co-sputtering method exhibited an oblique nanorods array structure with average diameter 108 ± 15 nm and 7.5 % Au and 92.5 % Ag content was recorded with EDS analysis.

Similar to the Au-Ag bimetallic substrates, nitric acid etching of the Au-Ag alloyed substrates also resulted in coalescence reducing the surface roughness and SERS enhancement. The base etching with the mixture of 30% NH_4OH and 30% H_2O_2 diluted in methanol at a ratio of 1:1:4 for 20-120 s showed successful selective etching of Ag and creation of surface roughness which varied with the etching time. In addition, nanorod diameter gradually decreased as the dealloying time was increased and EDS analysis revealed that the Ag mass percent decreased while the relative Au content was increased as etching time was increased. The optimum etching condition was found at 40 s in which resulted in 9.6% Au and 90.4% Ag on the Au-Ag dealloyed substrate.

The optical absorption of the Au-Ag alloyed nanorods showed LSPR spectrum located between pure Ag and Au film. XRD also revealed the Au and Ag FCC phases. Likewise, the binding energies of Au and Ag from XPS analysis exhibited shifts from the pure metallic Au and Ag state indicating alloy formation. Oxide formation was not observed on the surface during dealloying process, which is desired for SERS. The hydrophilicity of the Au-Ag dealloyed substrate was found to increase initially with increasing etching time until 60 s. The hydrophilic property as well as the roughened surface of the Au-Ag dealloyed substrate encourage a large number of 4-MBA molecules adsorbed on its surface, where the Au in the dealloyed substrate supports the binding with the thiol group of 4-MBA molecules.

According to SERS sensitivity, the Au-Ag dealloyed substrates provided higher SERS signals than that of Au-Ag alloyed substrates at all concentrations. The Raman signal was distinctive until 10^{-9} M on the Au-Ag dealloyed substrate while on the

alloyed substrate, detection limit was ten times less at 10^{-8} M. EF was found to be 1.5×10^6 for the Au-Ag dealloyed substrate and 4.6×10^5 for the Au-Ag alloyed substrate. The improved SERS enhancement of the Au-Ag dealloyed substrate originates from the combination of surface roughness and the complex effect of functional group on gold surface induced the LSPR based on both EM and CM mechanism.

The Au-Ag dealloyed substrate exhibited good uniformity with %RSD 5.87 and 7.94 at characteristic Raman peaks of 1078 and 1587 cm^{-1} respectively. The reproducibility was also within an acceptance range with %RSD 11.6 and 9.3, respectively. The Au-Ag alloyed and the dealloyed substrates also demonstrated a robust analytical signal stability at around 35% for over a month while the aged pure Ag substrate remained only at 8%. This indicates that the co-sputtering and base etching technique provides uniform, reproducible and stable Au-Ag alloyed and dealloyed substrates that have potential for various applications.

5.1.3 Urinary Crystal Detection Using Au-Ag Dealloyed Substrate

Considering for trace molecule detection, the Au-Ag dealloyed substrate was used to detect urinary crystals which promote kidney stone formation. The distinct spectra of three different crystals; COM, CAP and uric acid are identified on the dealloyed substrate. The obtained signals on the fabricated nanostructures are higher than that on silicon substrate due to Raman signal enhancement. Among these crystals, uric acid has the highest SERS signal due to its sensitive Raman structure and higher water solubility. The Au-Ag dealloyed substrate can detect uric acid solution in a linear range from 0 to 1×10^{-5} M. The detection limit was estimated to be 1.27×10^{-6} M in synthetic urine which is less than the normal range of uric acid in healthy human. The results show promise for early diagnosis of uric acid-type kidney stone diseases in the real urine samples.

5.2 Recommendation

5.2.1 Fabrication of Au-Ag Bimetallic Nanorods via Galvanic Replacement and Dealloying Process

It should be considered to add a thin adhesive layer on the Si substrate. such as chromium, nickel, or titanium before depositing the Ag layer on the silicon substrate using the sputtering processes to enhance the adhesiveness of the SERS bimetallic

films. Metals like Cr, Ni or Ti can bind to oxygen on the silicon surface with a high binding strength. The binding renders to improve metal adhesion because of reduced surface diffusion which can form a homogenous interface of substrate and coating metals. Considering a strong adhesion between Ag thin film and Si substrate, more dealloying conditions could be studied, for example: high concentration of etchants and longer etching time. In terms of galvanic reaction, besides concentration and replacement time, temperature also should be considered. Investigation on temperature effect might result in morphology changes and reaction rate.

5.2.2 Fabrication of Au-Ag Alloyed Nanorods by Co-sputtering Deposition and Dealloying Process

In current study, the Au sputtering power is maintained in a range of 10-30 W. In this range, the % Au in the alloyed structure is around 8-20 % by weight and relatively the Ag metal is 80-92%. Other variations of Au sputtering power could be studied as it affects LSPR and SERS performance. Besides a variety of HNO₃ concentration and the etching temperature also affects dealloying rate. It is recommended to investigate the etching temperature by increasing it from the room temperature to a higher value, which might improve the Ag dissolution and morphology changes of the dealloyed substrates.

For base etching, it should be taken into the account to investigate a relationship between the etchant ratio and etching rate. As the literature claimed that increasing the amount of methanol, the reaction rate can be reduced. Thus, the amount of NH₄OH and H₂O₂ should be investigated in correspondence with reaction rate and etched morphology to further tune the dealloying process.

5.2.3 Urinary Crystal Detection Using Au-Ag Dealloyed Substrate

The urinary crystals are well known for their low water solubility. A pH adjustment should be done to completely dissolve the crystals. Acid or base solvent; NaOH, HNO₃ and HCl can be able to dissolve uric acid, CAP and COM. Thus, the effect of pH might be interesting because the crystal solubility affects SERS performance and further signal enhancement is possible with lower LOD if the solubility of the urinary crystals can be increased. For uric spiked in synthetic urine, the higher concentration of the urine should be demonstrated. If there is a high signal interference from the

components in artificial urine, the sample preparation procedure should be revised before testing in real human urine.

REFERENCES

- Albrecht, M. G., & Creighton, J. A. (1977). Anomalously intense Raman spectra of pyridine at a silver electrode. *Journal of the American Chemical Society*, 99(15), 5215-5217. <https://doi.org/10.1021/ja00457a071>
- Alula, M. T., Lemmens, P., Bo, L., Wulferding, D., Yang, J., & Spende, H. (2019). Preparation of silver nanoparticles coated ZnO/Fe₃O₄ composites using chemical reduction method for sensitive detection of uric acid via surface-enhanced Raman spectroscopy. *Analytica Chimica Acta*, 1073, 62-71. <https://doi.org/10.1016/j.aca.2019.04.061>
- Alvarez-Puebla, R. A., Bravo-Vasquez, J. P., Cheben, P., Xu, D.-X., Waldron, P., & Fenniri, H. (2009). SERS-active Ag/Au bimetallic nanoalloys on Si/SiO_x. *Journal of Colloid and Interface Science*, 333(1), 237-241. <https://doi.org/10.1016/j.jcis.2009.01.070>
- Ankudze, B., & Pakkanen, T. T. (2018). Gold nanoparticle decorated Au-Ag alloy tubes: A bifunctional substrate for label-free and in situ surface-enhanced Raman scattering based reaction monitoring. *Applied Surface Science*, 453, 341-349. <https://doi.org/10.1016/j.apsusc.2018.05.041>
- Aroca, R. F., Alvarez-Puebla, R. A., Pieczonka, N., Sanchez-Cortez, S., & Garcia-Ramos, J. V. (2005). Surface-enhanced Raman scattering on colloidal nanostructures. *Advances in Colloid and Interface Science*, 116(1), 45-61. <https://doi.org/10.1016/j.cis.2005.04.007>
- Asiala, S. M., & Schultz, Z. D. (2011). Characterization of hotspots in a highly enhancing SERS substrate. *The Analyst*, 136(21), 4472-4479. <https://doi.org/10.1039/c1an15432j>
- Ausman, L. K., & Schatz, G. C. (2008). Whispering-gallery mode resonators: Surface enhanced Raman scattering without plasmons. *The Journal of Chemical Physics*, 129(5), 054704. <https://doi.org/10.1063/1.2961012>
- Barranco, A., Borrás, A., Gonzalez-Elipe, A. R., & Palmero, A. (2016). Perspectives on oblique angle deposition of thin films: From fundamentals to devices. *Progress in Materials Science*, 76, 59-153. <https://doi.org/10.1016/j.pmatsci.2015.06.003>

- Bekana, D., Liu, R., Amde, M., & Liu, J.-F. (2016). Use of Polycrystalline Ice for Assembly of Large Area Au Nanoparticle Superstructures as SERS Substrates. *ACS Applied Materials & Interfaces*, 9(1), 513-520. <https://doi.org/10.1021/acsami.6b15378>
- Bibikova, O., Haas, J., López-Lorente, A. I., Popov, A., Kinnunen, M., Meglinski, I., & Mizaikoff, B. (2017). Towards enhanced optical sensor performance: SEIRA and SERS with plasmonic nanostars. *Analyst*, 142(6), 951-958. <https://doi.org/10.1039/c6an02596j>
- Binh, N. T., & Dong, N. Q. (2015). Preparation of Au-Ag Alloy Nanoparticles for Surface Enhanced Raman Scattering. *VNU Journal of Science: Mathematics - Physics*, 31(1). <https://doi.org/js.vnu.edu.vn/MaP/article/view/98>
- Budnyk, A. P., Damin, A., Agostini, G., & Zecchina, A. (2010). Gold Nanoparticle Aggregates Immobilized on High Surface Area Silica Substrate for Efficient and Clean SERS Applications. *The Journal of Physical Chemistry C*, 114(9), 3857-3862. <https://doi.org/10.1021/jp9112816>
- Bumrah, G. S., & Sharma, R. M. (2016). Raman spectroscopy – Basic principle, instrumentation and selected applications for the characterization of drugs of abuse. *Egyptian Journal of Forensic Sciences*, 6(3), 209-215. <https://doi.org/10.1016/j.ejfs.2015.06.001>
- Burr, L., Schubert, I., Sigle, W., Trautmann, C., & Toimil-Molaes, M. E. (2015). Surface Enrichment in Au-Ag Alloy Nanowires and Investigation of the Dealloying Process. *The Journal of Physical Chemistry C*, 119(36), 20949-20956. <https://doi.org/10.1021/acs.jpcc.5b05596>
- Butler, H. J., Ashton, L., Bird, B., Cinque, G., Curtis, K., Dorney, J., Esmonde-White, K., Fullwood, N. J., Gardner, B., Martin-Hirsch, P. L., Walsh, M. J., McAinsh, M. R., Stone, N., & Martin, F. L. (2016). Using Raman spectroscopy to characterize biological materials. *Nature Protocols*, 11(4), 664-687. <https://doi.org/10.1038/nprot.2016.036>
- Caro, C., Gámez, F., & Zaderenko, A. P. (2018). Preparation of Surface-Enhanced Raman Scattering Substrates Based on Immobilized Silver-Capped Nanoparticles. *Journal of Spectroscopy*, 2018, 4127108. <https://doi.org/10.1155/2018/4127108>

- Chae, W.-S., Lee, Hee-Ok, Kim, Eun-Mee, & Yu, Hyunung. (2011). Molecular Sensing Efficiency of Gold-Silver Alloy Nanowires. *Bulletin of the Korean Chemical Society*, 32(4), 1346–1348. <https://doi.org/10.5012/BKCS.2011.32.4.1346>
- Chao, B.-K., Xu, Y., Ho, H.-C., Yiu, P., Lai, Y.-C., Shek, C.-H., & Hsueh, C.-H. (2017). Gold-rich ligament nanostructure by dealloying Au-based metallic glass ribbon for surface-enhanced Raman scattering. *Scientific reports*, 7(1), 7485. <https://doi.org/10.1038/s41598-017-08033-7>
- Chauvin, A., Delacôte, C., Boujtita, M., Angleraud, B., Ding, J., Choi, C.-H., Tessier, P.-Y., & El Mel, A.-A. (2016). Dealloying of gold-copper alloy nanowires: From hillocks to ring-shaped nanopores. *Beilstein journal of nanotechnology*, 7, 1361-1367. <https://doi.org/10.3762/bjnano.7.127>
- Chauvin, A., Stephant, N., Du, K., Ding, J., Wathuthanthri, I., Choi, C.-H., Tessier, P.-Y., & El Mel, A.-A. (2017). Large-Scale Fabrication of Porous Gold Nanowires via Laser Interference Lithography and Dealloying of Gold-Silver Nano-Alloys. *Micromachines*, 8(6), 168. <https://doi.org/10.3390/mi8060168>
- Chauvin, A., Txia Cha Heu, W., Tessier, P.-Y., & El Mel, A.-A. (2016). Impact of the morphology and composition on the dealloying process of co-sputtered silver–aluminum alloy thin films. *physica status solidi (b)*, 253(11), 2167-2174. <https://doi.org/10.1002/pssb.201600604>
- Chee, S. W., Tan, S. F., Baraissov, Z., Bosman, M., & Mirsaidov, U. (2017). Direct observation of the nanoscale Kirkendall effect during galvanic replacement reactions. *Nature Communications*, 8(1), 1224. <https://doi.org/10.1038/s41467-017-01175-2>
- Chen-Wiegart, Y.-c. K., Wang, S., McNulty, I., & Dunand, D. C. (2013). Effect of Ag–Au composition and acid concentration on dealloying front velocity and cracking during nanoporous gold formation. *Acta Materialia*, 61(15), 5561-5570. <https://doi.org/10.1016/j.actamat.2013.05.039>
- Chen, B., Meng, G., Huang, Q., Huang, Z., Xu, Q., Zhu, C., Qian, Y., & Ding, Y. (2014). Green Synthesis of Large-Scale Highly Ordered Core@Shell Nanoporous Au@Ag Nanorod Arrays as Sensitive and Reproducible 3D SERS Substrates. *ACS Applied Materials & Interfaces*, 6(18), 15667-15675. <https://doi.org/10.1021/am505474n>

- Chen, J., McLellan, J. M., Siekkinen, A., Xiong, Y., Li, Z.-Y., & Xia, Y. (2006). Facile Synthesis of Gold-Silver Nanocages with Controllable Pores on the Surface. *Journal of the American Chemical Society*, *128*(46), 14776-14777. <https://doi.org/10.1021/ja066023g>
- Cheng, H.-W., Huan, S.-Y., Wu, H.-L., Shen, G.-L., & Yu, R.-Q. (2009). Surface-Enhanced Raman Spectroscopic Detection of a Bacteria Biomarker Using Gold Nanoparticle Immobilized Substrates. *Analytical Chemistry*, *81*(24), 9902-9912. <https://doi.org/10.1021/ac9014275>
- Cui, Y., Ren, B., Yao, J.-L., Gu, R.-A., & Tian, Z.-Q. (2006). Synthesis of AgcoreAushell Bimetallic Nanoparticles for Immunoassay Based on Surface-Enhanced Raman Spectroscopy. *The Journal of Physical Chemistry B*, *110*(9), 4002-4006. <https://doi.org/10.1021/jp056203x>
- Çulha, M., Kahraman, M., Tokman, N., & Türkoğlu, G. (2008). Surface-Enhanced Raman Scattering on Aggregates of Silver Nanoparticles with Definite Size. *The Journal of Physical Chemistry C*, *112*(28), 10338-10343. <https://doi.org/10.1021/jp711177z>
- Daza, L. G., Castro-Rodríguez, R., Cirerol-Carrillo, M., Martín-Tovar, E. A., Méndez-Gamboa, J., Medina-Esquivel, R., Pérez-Quintana, I., & Iribarren, A. (2017). Nanocolumnar CdS thin films grown by glancing angle deposition from a sublimate vapor effusion source. *Journal of Applied Research and Technology*, *15*(3), 271-277. <https://doi.org/10.1016/j.jart.2017.02.003>
- De Aza, P. N., Santos, C., Pazo, A., de Aza, S., Cuscó, R., & Artús, L. (1997). Vibrational Properties of Calcium Phosphate Compounds. 1. Raman Spectrum of β -Tricalcium Phosphate. *Chemistry of Materials*, *9*(4), 912-915. <https://doi.org/10.1021/cm960425d>
- Driskell, J. D., Shanmukh, S., Liu, Y., Chaney, S. B., Tang, X. J., Zhao, Y. P., & Dluhy, R. A. (2008). The Use of Aligned Silver Nanorod Arrays Prepared by Oblique Angle Deposition as Surface Enhanced Raman Scattering Substrates. *The Journal of Physical Chemistry C*, *112*(4), 895-901. <https://doi.org/10.1021/jp075288u>
- Erlebacher, J., Aziz, M. J., Karma, A., Dimitrov, N., & Sieradzki, K. (2001). Evolution of nanoporosity in dealloying. *Nature*, *410*(6827), 450-453. <https://doi.org/10.1038/35068529>

- Fan, M., Andrade, G. F. S., & Brolo, A. G. (2011). A review on the fabrication of substrates for surface enhanced Raman spectroscopy and their applications in analytical chemistry. *Analytica Chimica Acta*, 693(1), 7-25. <https://doi.org/10.1016/j.aca.2011.03.002>
- Fan, M., Lai, F.-J., Chou, H.-L., Lu, W.-T., Hwang, B.-J., & Brolo, A. G. (2013). Surface-enhanced Raman scattering (SERS) from Au:Ag bimetallic nanoparticles: the effect of the molecular probe. *Chemical Science*, 4(1), 509-515. <https://doi.org/10.1039/c2sc21191b>
- Feig, D. I., Mazzali, M., Kang, D.-H., Nakagawa, T., Price, K., Kannelis, J., & Johnson, R. J. (2006). Serum Uric Acid: A Risk Factor and a Target for Treatment? *Journal of the American Society of Nephrology*, 17(4), S69-S73. <https://doi.org/10.1681/asn.2005121331>
- Fleger, Y., & Rosenbluh, M. (2009). Surface Plasmons and Surface Enhanced Raman Spectra of Aggregated and Alloyed Gold-Silver Nanoparticles. *Research Letters in Optics*, 5, 475941. <https://doi.org/10.1155/2009/475941>
- Fleischmann, M., Hendra, P. J., & McQuillan, A. J. (1974). Raman spectra of pyridine adsorbed at a silver electrode. *Chemical Physics Letters*, 26(2), 163-166. [https://doi.org/10.1016/0009-2614\(74\)85388-1](https://doi.org/10.1016/0009-2614(74)85388-1)
- Fortuni, B., Fujita, Y., Ricci, M., Inose, T., Aubert, R., Lu, G., Hutchison, J. A., Hofkens, J., Latterini, L., & Uji-i, H. (2017). A novel method for in situ synthesis of SERS-active gold nanostars on polydimethylsiloxane film. *Chemical Communications*, 53(37), 5121-5124. <https://doi.org/10.1039/c7cc01776f>
- Forty, A. J., & Durkin, P. (1980). A micromorphological study of the dissolution of silver-gold alloys in nitric acid. *Philosophical Magazine A*, 42(3), 295-318. <https://doi.org/10.1080/01418618008239360>
- Frausto-Reyes, C., Loza-Cornejo, S., Terrazas, T., Miranda-Beltran Mde, L., Aparicio-Fernandez, X., Lopez-Macias, B. M., Morales-Martinez, S. E., & Ortiz-Morales, M. (2014). Raman spectroscopy study of calcium oxalate extracted from cacti stems. *Applied Spectroscopy*, 68(11), 1260-1265. <https://doi.org/10.1366/14-07485>
- Garcia-Leis, A., Torreggiani, A., Garcia-Ramos, J. V., & Sanchez-Cortes, S. (2015). Hollow Au/Ag nanostars displaying broad plasmonic resonance and high

- surface-enhanced Raman sensitivity. *Nanoscale*, 7(32), 13629-13637. <https://doi.org/10.1039/c5nr02819a>
- Gisbert Quilis, N., Lequeux, M., Venugopalan, P., Khan, I., Knoll, W., Boujday, S., Lamy de la Chapelle, M., & Dostalek, J. (2018). Tunable laser interference lithography preparation of plasmonic nanoparticle arrays tailored for SERS. *Nanoscale*, 10(21), 10268-10276. <https://doi.org/10.1039/c7nr08905h>
- Godipurge, S. S., Yallappa, S., Biradar, N. J., Biradar, J. S., Dhananjaya, B. L., Hegde, G., Jagadish, K., & Hegde, G. (2016). A facile and green strategy for the synthesis of Au, Ag and Au-Ag alloy nanoparticles using aerial parts of *R. hypocrateriformis* extract and their biological evaluation. *Enzyme and Microbial Technology*, 95, 174-184. <https://doi.org/10.1016/j.enzmictec.2016.08.006>
- Gómez-Graña, S., Pérez-Juste, J., Alvarez-Puebla, R. A., Guerrero-Martínez, A., & Liz-Marzán, L. M. (2013). Self-Assembly of Au@Ag Nanorods Mediated by Gemini Surfactants for Highly Efficient SERS-Active Supercrystals. *Advanced Optical Materials*, 1(7), 477-481. <https://doi.org/10.1002/adom.201300162>
- Goodall, B. L., Robinson, A. M., & Brosseau, C. L. (2012). Electrochemical-surface enhanced Raman spectroscopy (E-SERS) of uric acid: a potential rapid diagnostic method for early preeclampsia detection. *Physical Chemistry Chemical Physics*, 15(5), 1382-1388. <https://doi.org/10.1039/c2cp42596c>
- Gutés, A., Maboudian, R., & Carraro, C. (2012). Gold-Coated Silver Dendrites as SERS Substrates with an Improved Lifetime. *Langmuir*, 28(51), 17846-17850. <https://doi.org/10.1021/la303421s>
- He, S., Chua, J., Tan, E. K. M., & Kah, J. C. Y. (2017). Optimizing the SERS enhancement of a facile gold nanostar immobilized paper-based SERS substrate. *RSC Advances*, 7(27), 16264-16272. <https://doi.org/10.1039/c6ra28450g>
- Herrera, G. M., Padilla, A. C., & Hernandez-Rivera, S. P. (2013). Surface Enhanced Raman Scattering (SERS) Studies of Gold and Silver Nanoparticles Prepared by Laser Ablation. *Nanomaterials (Basel, Switzerland)*, 3(1), 158-172. <https://doi.org/10.3390/nano3010158>

- Ho, C.-H., & Lee, S. (2015). SERS and DFT investigation of the adsorption behavior of 4-mercaptobenzoic acid on silver colloids. *Colloids and Surfaces A: Physicochemical and Engineering Aspects*, 474, 29-35. <https://doi.org/10.1016/j.colsurfa.2015.03.004>
- Hornyak, G. L., Patrissi, C. J., Oberhauser, E. B., Martin, C. R., Valmalette, J. C., Lemaire, L., Dutta, J., & Hofmann, H. (1997). Effective medium theory characterization of Au/Ag nanoalloy-porous alumina composites. *Nanostructured Materials*, 9(1), 571-574. [https://doi.org/10.1016/S0965-9773\(97\)00127-X](https://doi.org/10.1016/S0965-9773(97)00127-X)
- Horprathum, M., Eiamchai, P., Kaewkhao, J., Chananonawathorn, C., Patthanasettakul, V., Limwichean, S., Nuntawong, N., & Chindaudom, P. (2014). Fabrication of nanostructure by physical vapor deposition with glancing angle deposition technique and its applications. *AIP Conference Proceedings*, 1617(1), 7-11. <https://doi.org/10.1063/1.4897091>
- Hu, L.-W., Liu, X., Le, G.-M., Li, J.-F., Qu, F.-S., Lu, S.-Y., & Qi, L. (2019). Morphology evolution and SERS activity of the nanoporous Au prepared by dealloying sputtered Au-Ag film. *Physica B: Condensed Matter*, 558, 49-53. <https://doi.org/10.1016/j.physb.2019.01.019>
- Huang, H., Lai, J., Lu, J., & Li, Z. (2019). Pulsed laser ablation of bulk target and particle products in liquid for nanomaterial fabrication. *AIP Advances*, 9(1), 015307. <https://doi.org/10.1063/1.5082695>
- Huang, J., Liu, Y., He, X., Tang, C., Du, K., & He, Z. (2017). Gradient nanoporous gold: a novel surface-enhanced Raman scattering substrate. *RSC Advances*, 7(26), 15747-15753. <https://doi.org/10.1039/c6ra28591k>
- Huang, Y., Lin, D., Li, M., Yin, D., Wang, S., & Wang, J. (2019). Ag@Au Core-Shell Porous Nanocages with Outstanding SERS Activity for Highly Sensitive SERS Immunoassay. *Sensors (Basel, Switzerland)*, 19(7), 1554. <https://doi.org/10.3390/s19071554>
- Hug, S., Grohe, B., Jalkanen, J., Chan, B., Galarreta, B., Vincent, K., Lagugn e-Labarthe, F., Lajoie, G., Goldberg, H. A., Karttunen, M., & Hunter, G. K. (2012). Mechanism of inhibition of calcium oxalate crystal growth by an osteopontin phosphopeptide. *Soft Matter*, 8(4), 1226-1233. <https://doi.org/10.1039/c1sm06232h>

- Hwang, J. S., & Yang, M. (2018). Sensitive and Reproducible Gold SERS Sensor Based on Interference Lithography and Electrophoretic Deposition. *Sensors (Basel)*, *18*(11). <https://doi.org/10.3390/s18114076>
- Jayaraman, V. K., Kuwabara, Y. M., Álvarez, A. M., & Amador, M. d. I. I. O. (2016). Importance of substrate rotation speed on the growth of homogeneous ZnO thin films by reactive sputtering. *Materials Letters*, *169*, 1-4. <https://doi.org/10.1016/j.matlet.2016.01.088>
- Jeanmaire, D. L., & Van Duyne, R. P. (1977). Surface raman spectroelectrochemistry: Part I. Heterocyclic, aromatic, and aliphatic amines adsorbed on the anodized silver electrode. *Journal of Electroanalytical Chemistry and Interfacial Electrochemistry*, *84*(1), 1-20. [https://doi.org/10.1016/S0022-0728\(77\)80224-6](https://doi.org/10.1016/S0022-0728(77)80224-6)
- Jen, Y.-J., Chan, S., Huang, J.-W., Jheng, C.-Y., & Liu, W.-C. (2015). Self-Shadowing Deposited Pure Metal Nanohelix Arrays and SERS Application. *Nanoscale Research Letters*, *10*(1), 498. <https://doi.org/10.1186/s11671-015-1205-8>
- Jensen, L., Aikens, C. M., & Schatz, G. C. (2008). Electronic structure methods for studying surface-enhanced Raman scattering. *Chemical Society Reviews*, *37*(5), 1061-1073. <https://doi.org/10.1039/b706023h>
- Jun Yin, H., Yang Chen, Z., Mei Zhao, Y., Yang Lv, M., An Shi, C., Long Wu, Z., Zhang, X., Liu, L., Li Wang, M., & Jun Xu, H. (2015). Ag@Au core-shell dendrites: a stable, reusable and sensitive surface enhanced Raman scattering substrate. *Scientific reports*, *5*(1), 14502. <https://doi.org/10.1038/srep14502>
- Kertis, F., Snyder, J., Govada, L., Khurshid, S., Chayen, N., & Erlebacher, J. (2010). Structure/processing relationships in the fabrication of nanoporous gold. *The Journal of The Minerals*, *62*(6), 50-56. <https://doi.org/10.1007/s11837-010-0087-6>
- Khudhayer, W. J., Sharma, R., & Karabacak, T. (2009). Hydrophobic metallic nanorods with Teflon nanopatches. *Nanotechnology*, *20*(27), 275302. <https://doi.org/10.1088/0957-4484/20/27/275302>
- Kim, M. H., Lu, X., Wiley, B., Lee, E. P., & Xia, Y. (2008). Morphological Evolution of Single-Crystal Ag Nanospheres during the Galvanic Replacement

- Reaction with H₂AuCl₄. *The Journal of Physical Chemistry C*, 112(21), 7872-7876. <https://doi.org/10.1021/jp711662f>
- Koivisto, J., Chen, X., Donnini, S., Lahtinen, T., Häkkinen, H., Groenhof, G., & Pettersson, M. (2016). Acid-Base Properties and Surface Charge Distribution of the Water-Soluble Au₁₀₂ (pMBA)₄₄ Nanocluster. *The Journal of Physical Chemistry C*, 120(18), 10041-10050. <https://doi.org/10.1021/acs.jpcc.6b00922>
- Krishnan, S. K., Esparza, R., Flores-Ruiz, F. J., Padilla-Ortega, E., Luna-Bárceñas, G., Sanchez, I. C., & Pal, U. (2018). Seed-Mediated Growth of Ag@Au Nanodisks with Improved Chemical Stability and Surface-Enhanced Raman Scattering. *ACS Omega*, 3(10), 12600-12608. <https://doi.org/10.1021/acsomega.8b02333>
- Lai, Y.-C., Ho, H.-C., Shih, B.-W., Tsai, F.-Y., & Hsueh, C.-H. (2018). High performance and reusable SERS substrates using Ag/ZnO heterostructure on periodic silicon nanotube substrate. *Applied Surface Science*, 439, 852-858. <https://doi.org/10.1016/j.apsusc.2018.01.092>
- Lau, W.-F., Bai, F., & Huang, Z. (2013). Ballistic glancing angle deposition of inclined Ag nanorods limited by adatom diffusion. *Nanotechnology*, 24(46), 465707. <https://doi.org/10.1088/0957-4484/24/46/465707>
- Lee, C., Robertson, C. S., Nguyen, A. H., Kahraman, M., & Wachsmann-Hogiu, S. (2015). Thickness of a metallic film, in addition to its roughness, plays a significant role in SERS activity. *Scientific reports*, 5(1), 11644. <https://doi.org/10.1038/srep11644>
- Li, J., Zhang, G., Wang, J., Maksymov, I. S., Greentree, A. D., Hu, J., Shen, A., Wang, Y., & Trau, M. (2018). Facile One-Pot Synthesis of Nanodot-Decorated Gold-Silver Alloy Nanoboxes for Single-Particle Surface-Enhanced Raman Scattering Activity. *ACS Appl Mater Interfaces*, 10(38), 32526-32535. <https://doi.org/10.1021/acsami.8b10112>
- Li, K., Liu, G., Zhang, S., Dai, Y., Ghafoor, S., Huang, W., Zu, Z., & Lu, Y. (2019). A porous Au-Ag hybrid nanoparticle array with broadband absorption and high-density hotspots for stable SERS analysis. *Nanoscale*, 11(19), 9587-9592. <https://doi.org/10.1039/c9nr01744e>

- Li, Y., Cai, W., & Duan, G. (2008). Ordered Micro/Nanostructured Arrays Based on the Monolayer Colloidal Crystals. *Chemistry of Materials*, *20*(3), 615-624. <https://doi.org/10.1021/cm701977g>
- Lin, WC., Huang, SH., & Chen, CL. (2010). Controlling SERS intensity by tuning the size and height of a silver nanoparticle array. *Applied Physics A*, *101*, 185–18. <https://doi.org/10.1007/s00339-010-5777-y>
- Link, S., Wang, Z. L., & El-Sayed, M. A. (1999). Alloy Formation of Gold-Silver Nanoparticles and the Dependence of the Plasmon Absorption on Their Composition. *The Journal of Physical Chemistry B*, *103*(18), 3529-3533. <https://doi.org/10.1021/jp990387w>
- Liu, X., Shao, Y., Tang, Y., & Yao, K.-F. (2014). Highly uniform and reproducible surface enhanced raman scattering on air-stable metallic glassy nanowire array. *Scientific reports*, *4*, 5835. <https://doi.org/10.1038/srep05835>
- Liu, Y., Wu, H., Ma, L., Zou, S., Ling, Y., & Zhang, Z. (2018). Highly stable and active SERS substrates with Ag-Ti alloy nanorods. *Nanoscale*, *10*(42), 19863-19870. <https://doi.org/10.1039/c8nr07138a>
- Liu, Y. J., Chu, H. Y., & Zhao, Y. P. (2010). Silver Nanorod Array Substrates Fabricated by Oblique Angle Deposition: Morphological, Optical, and SERS Characterizations. *The Journal of Physical Chemistry C*, *114*(18), 8176-8183. <https://doi.org/10.1021/jp1001644>
- Lu, X., Chen, J., Skrabalak, S. E., & Xia, Y. (2007). Galvanic replacement reaction: A simple and powerful route to hollow and porous metal nanostructures. *Proceedings of the Institution of Mechanical Engineers, Part N: Journal of Nanoengineering and Nanosystems*, *221*(1), 1-16. <https://doi.org/10.1243/17403499jnn111>
- Lu, Y., Wu, C., You, R., Wu, Y., Shen, H., Zhu, L., & Feng, S. (2018). Superhydrophobic silver film as a SERS substrate for the detection of uric acid and creatinine. *Biomedical Optics Express*, *9*(10), 4988-4997. <https://doi.org/10.1364/boe.9.004988>
- Lu, Y., Xue, G., & Dong, J. (1993). HNO₃ etched silver foil as an effective substrate for surface-enhanced Raman scattering (SERS) analysis. *Applied Surface Science*, *68*(4), 485-489. [https://doi.org/10.1016/0169-4332\(93\)90231-Y](https://doi.org/10.1016/0169-4332(93)90231-Y)

- Macias, G., Alba, M., Marsal, L. F., & Mihi, A. (2016). Surface roughness boosts the SERS performance of imprinted plasmonic architectures. *Journal of Materials Chemistry C*, 4(18), 3970-3975. <https://doi.org/10.1039/c5tc02779a>
- Mahurin, S. M., John, J., Sepaniak, M. J., & Dai, S. (2011). A reusable surface-enhanced Raman scattering (SERS) substrate prepared by atomic layer deposition of alumina on a multi-layer gold and silver film. *Appl Spectrosc*, 65(4), 417-422. <https://doi.org/10.1366/10-05930>
- Mao, A., Jin, X., Gu, X., Wei, X., & Yang, G. (2012). Rapid, green synthesis and surface-enhanced Raman scattering effect of single-crystal silver nanocubes. *Journal of Molecular Structure*, 1021, 158-161. <https://doi.org/10.1016/j.molstruc.2012.04.043>
- Miele, E., Malerba, M., Dipalo, M., Rondanina, E., Toma, A., & Angelis, F. D. (2014). Controlling Wetting and Self-Assembly Dynamics by Tailored Hydrophobic and Oleophobic Surfaces. *Advanced Materials*, 26(24), 4179-4183. <https://doi.org/10.1002/adma.201400310>
- Moore, W. V. H. a. G. (1928). Transmission and Reflection of Gold and Silver Films. *The Journal of the Optical Society of America*, 16, 174-176. <https://doi.org/10.1364/JOSA.16.000174>
- Moskovits, M. (1978). Surface roughness and the enhanced intensity of Raman scattering by molecules adsorbed on metals. *The Journal of Chemical Physics*, 69(9), 4159-4161. <https://doi.org/10.1063/1.437095>
- Mun, C., Linh, V. T. N., Kwon, J.-D., Jung, H. S., Kim, D.-H., & Park, S.-G. (2019). Highly Sensitive and Selective Nanogap-Enhanced SERS Sensing Platform. *Nanomaterials (Basel, Switzerland)*, 9(4), 619. <https://doi.org/10.3390/nano9040619>
- NIST. (2012). IUPAC-NIST Solubility Database. <https://doi.org/10.18434/T4QC79>
- Nuntawong, N., Eiamchai, P., Somrang, W., Denchitcharoen, S., Limwichean, S., Horprathum, M., Patthanasettakul, V., Chaiya, S., Leelapojanaporn, A., Saiseng, S., Pongsethasant, P., & Chindaudom, P. (2017). Detection of methamphetamine/amphetamine in human urine based on surface-enhanced Raman spectroscopy and acidulation treatments. *Sensors and Actuators B: Chemical*, 239, 139-146. <https://doi.org/10.1016/j.snb.2016.07.129>

- Nuntawong, N., Eiamchai, P., Wong-ek, B., Horprathum, M., Limwichean, K., Patthanasettakul, V., & Chindaudom, P. (2013). Shelf time effect on SERS effectiveness of silver nanorod prepared by OAD technique. *Vacuum*, 88, 23-27. <https://doi.org/10.1016/j.vacuum.2012.08.006>
- Okamoto, F. (1973). Etching solution for silver. *Patent, US3860423A*.
- Olea-Mejía, O., Fernández-Mondragón, M., Rodríguez-de la Concha, G., & Camacho-López, M. (2015). SERS-active Ag, Au and Ag-Au alloy nanoparticles obtained by laser ablation in liquids for sensing methylene blue. *Applied Surface Science*, 348, 66-70. <https://doi.org/10.1016/j.apsusc.2015.01.075>
- Ouyang, L., Ren, W., Zhu, L., & Irudayaraj, J. (2017). Prosperity to challenges: recent approaches in SERS substrate fabrication. *Reviews in Analytical Chemistry*, 36(1). <https://doi.org/10.1515/revac-2016-0027>
- Pawar, S., Teja, B. R., Nagarjuna, R., Ganesan, R., & Nag, A. (2019). Probing the surface composition effect of silver-gold alloy in SERS efficiency. *Colloids and Surfaces A: Physicochemical and Engineering Aspects*, 578, 123638. <https://doi.org/10.1016/j.colsurfa.2019.123638>
- Peng, Z., Spliethoff, B., Tesche, B., Walther, T., & Kleinermanns, K. (2006). Laser-Assisted Synthesis of Au–Ag Alloy Nanoparticles in Solution. *The Journal of Physical Chemistry B*, 110(6), 2549-2554. <https://doi.org/10.1021/jp056677w>
- Péron, O., Rinnert, E., Lehaitre, M., Crassous, P., & Compère, C. (2009). Detection of polycyclic aromatic hydrocarbon (PAH) compounds in artificial sea-water using surface-enhanced Raman scattering (SERS). *Talanta*, 79(2), 199-204. <https://doi.org/10.1016/j.talanta.2009.03.043>
- Petti, L., Capasso, R., Rippa, M., Pannico, M., La Manna, P., Peluso, G., Calarco, A., Bobeico, E., & Musto, P. (2016). A plasmonic nanostructure fabricated by electron beam lithography as a sensitive and highly homogeneous SERS substrate for bio-sensing applications. *Vibrational Spectroscopy*, 82, 22-30. <https://doi.org/10.1016/j.vibspec.2015.11.007>
- Pucetaite, M., Velicka, M., Pilipavicius, J., Beganskiene, A., Ceponkus, J., & Sablinskas, V. (2016). Uric acid detection by means of SERS spectroscopy

- on dried Ag colloidal drops. *Journal of Raman Spectroscopy*, 47(6), 681-686. <https://doi.org/10.1002/jrs.4875>
- Qiu, H., Zhang, Z., Huang, X., & Qu, Y. (2011). Dealloying Ag-Al alloy to prepare nanoporous silver as a substrate for surface-enhanced Raman scattering: effects of structural evolution and surface modification. *Chemphyschem*, 12(11), 2118-2123. <https://doi.org/10.1002/cphc.201100205>
- Rekha, C. R., Nayar, V. U., & Gopchandran, K. G. (2018). Synthesis of highly stable silver nanorods and their application as SERS substrates. *Journal of Science: Advanced Materials and Devices*, 3(2), 196-205. <https://doi.org/10.1016/j.jsamd.2018.03.003>
- Robbie, K., Sit, J. C., & Brett, M. J. (1998). Advanced techniques for glancing angle deposition. *Journal of Vacuum Science & Technology B: Microelectronics and Nanometer Structures Processing, Measurement, and Phenomena*, 16(3), 1115-1122. <https://doi.org/10.1116/1.590019>
- Sangpour, P., Akhavan, O., & Moshfegh, A. Z. (2007). rf reactive co-sputtered Au–Ag alloy nanoparticles in SiO₂ thin films. *Applied Surface Science*, 253(18), 7438-7442. <https://doi.org/10.1016/j.apsusc.2007.03.050>
- Sangpour, P., Akhavan, O., & Moshfegh, A. Z. (2009). The effect of Au/Ag ratios on surface composition and optical properties of co-sputtered alloy nanoparticles in Au–Ag:SiO₂ thin films. *Journal of Alloys and Compounds*, 486(1), 22-28. <https://doi.org/10.1016/j.jallcom.2009.06.201>
- Sanguansap, Y., Karn-orachai, K., & Laocharoensuk, R. (2020). Tailor-made porous striped gold-silver nanowires for surface enhanced Raman scattering based trace detection of β -hydroxybutyric acid. *Applied Surface Science*, 500, 144049. <https://doi.org/10.1016/j.apsusc.2019.144049>
- Satya Bharati, M. S., Chandu, B., & Rao, S. V. (2019). Explosives sensing using Ag-Cu alloy nanoparticles synthesized by femtosecond laser ablation and irradiation. *RSC Advances*, 9(3), 1517-1525. <https://doi.org/10.1039/c8ra08462a>
- Schwartzberg, A. M., Grant, C. D., Wolcott, A., Talley, C. E., Huser, T. R., Bogomolni, R., & Zhang, J. Z. (2004). Unique Gold Nanoparticle Aggregates as a Highly Active Surface-Enhanced Raman Scattering Substrate.

- The Journal of Physical Chemistry B*, 108(50), 19191-19197.
<https://doi.org/10.1021/jp048430p>
- Shuang, S., Lv, R., Xie, Z., & Zhang, Z. (2016). Surface Plasmon Enhanced Photocatalysis of Au/Pt-decorated TiO₂ Nanopillar Arrays. *Scientific reports*, 6(1), 26670. <https://doi.org/10.1038/srep26670>
- Sivashanmugan, K., Liao, J.-D., You, J.-W., & Wu, C.-L. (2013). Focused-ion-beam-fabricated Au/Ag multilayered nanorod array as SERS-active substrate for virus strain detection. *Sensors and Actuators B: Chemical*, 181, 361-367. <https://doi.org/10.1016/j.snb.2013.01.035>
- Song, C., Abell, J. L., He, Y., Hunyadi Murph, S., Cui, Y., & Zhao, Y. (2012). Gold-modified silver nanorod arrays: growth dynamics and improved SERS properties. *Journal of Materials Chemistry*, 22(3), 1150-1159. <https://doi.org/10.1039/c1jm14133c>
- Sun, Y., Mayers, B. T., & Xia, Y. (2002). Template-Engaged Replacement Reaction: A One-Step Approach to the Large-Scale Synthesis of Metal Nanostructures with Hollow Interiors. *Nano Letters*, 2(5), 481-485. <https://doi.org/10.1021/nl025531v>
- Sun, Y., & Xia, Y. (2004). Mechanistic Study on the Replacement Reaction between Silver Nanostructures and Chloroauric Acid in Aqueous Medium. *Journal of the American Chemical Society*, 126(12), 3892-3901. <https://doi.org/10.1021/ja039734c>
- Syu, W.-L., Lin, Y.-H., Paliwal, A., Wang, K.-S., & Liu, T.-Y. (2018). Highly sensitive and reproducible SERS substrates of bilayer Au and Ag nano-island arrays by thermal evaporation deposition. *Surface and Coatings Technology*, 350, 823-830. <https://doi.org/10.1016/j.surfcoat.2018.04.043>
- Tian, F., Bonnier, F., Casey, A., Shanahan, A. E., & Byrne, H. J. (2014). Surface enhanced Raman scattering with gold nanoparticles: effect of particle shape. *Analytical Methods*, 6(22), 9116-9123. <https://doi.org/10.1039/C4AY02112F>
- Tripp, R. A., Dluhy, R. A., & Zhao, Y. (2008). Novel nanostructures for SERS biosensing. *Nano Today*, 3(3), 31-37. [https://doi.org/10.1016/S1748-0132\(08\)70042-2](https://doi.org/10.1016/S1748-0132(08)70042-2)

- Villa, J. E. L., & Poppi, R. J. (2016). A portable SERS method for the determination of uric acid using a paper-based substrate and multivariate curve resolution. *Analyst*, *141*(6), 1966-1972. <https://doi.org/10.1039/c5an02398j>
- Vinod, M., & Gopchandran, K. G. (2014). Au, Ag and Au:Ag colloidal nanoparticles synthesized by pulsed laser ablation as SERS substrates. *Progress in Natural Science: Materials International*, *24*(6), 569-578. <https://doi.org/10.1016/j.pnsc.2014.10.003>
- Vinod, M., & Gopchandran, K. G. (2015). Ag@Au core-shell nanoparticles synthesized by pulsed laser ablation in water: Effect of plasmon coupling and their SERS performance. *Spectrochimica Acta Part A: Molecular and Biomolecular Spectroscopy*, *149*, 913-919. <https://doi.org/10.1016/j.saa.2015.05.004>
- Vinod, M., & Gopchandran, K. G. (2015). Bimetallic Au-Ag nanochains as SERS substrates. *Current Applied Physics*, *15*(8), 857-863. <https://doi.org/10.1016/j.cap.2015.03.018>
- Wachter, E. A., Moore, A. K., & Haas, J. W. (1992). Fabrication of tailored needle substrates for surface-enhanced Raman scattering. *Vibrational Spectroscopy*, *3*(1), 73-78. [https://doi.org/10.1016/0924-2031\(92\)85026-W](https://doi.org/10.1016/0924-2031(92)85026-W)
- Wang, T., Zhou, J., & Wang, Y. (2018). Simple, Low-Cost Fabrication of Highly Uniform and Reproducible SERS Substrates Composed of Ag-Pt Nanoparticles. *Nanomaterials (Basel, Switzerland)*, *8*(5), 331. <https://doi.org/10.3390/nano8050331>
- Westley, C., Xu, Y., Thilaganathan, B., Carnell, A. J., Turner, N. J., & Goodacre, R. (2017). Absolute Quantification of Uric Acid in Human Urine Using Surface Enhanced Raman Scattering with the Standard Addition Method. *Analytical Chemistry*, *89*(4), 2472-2477. <https://doi.org/10.1021/acs.analchem.6b04588>
- Wiriyakun, N., Pankhluab, K., Boonrunsiman, S., & Laocharoensuk, R. (2016). Site-Selective Controlled Dealloying Process of Gold-Silver Nanowire Array: a Simple Approach towards Long-Term Stability and Sensitivity Improvement of SERS Substrate. *Scientific reports*, *6*, 39115. <https://doi.org/10.1038/srep39115>
- Xia, X., Wang, Y., Ruditskiy, A., & Xia, Y. (2013). 25th Anniversary Article: Galvanic Replacement: A Simple and Versatile Route to Hollow

- Nanostructures with Tunable and Well-Controlled Properties. *Advanced Materials*, 25(44), 6313-6333. <https://doi.org/10.1002/adma.201302820>
- Xiao, G.-N., & Man, S.-Q. (2007). Surface-enhanced Raman scattering of methylene blue adsorbed on cap-shaped silver nanoparticles. *Chemical Physics Letters*, 447(4), 305-309. <https://doi.org/10.1016/j.cplett.2007.09.045>
- Xue, Y., Scaglione, F., Rizzi, P., & Battezzati, L. (2017). High performance SERS on nanoporous gold substrates synthesized by chemical de-alloying a Au-based metallic glass. *Applied Surface Science*, 426, 1113-1120. <https://doi.org/10.1016/j.apsusc.2017.07.302>
- Yan, WG., Qi, JW., Li, ZB. *et al.* (2014). Fabrication and Optical Properties of Au-Coated Polystyrene Nanosphere Arrays with Controlled Gaps. *Plasmonics* 9, 565–571. <https://doi.org/10.1007/s11468-013-9665-0>
- Yan, Z., Wu, Y., & Di, J. (2015). Formation of substrate-based gold nanocage chains through dealloying with nitric acid. *Beilstein journal of nanotechnology*, 6, 1362-1368. <https://doi.org/10.3762/bjnano.6.140>
- Yang, Y., Shi, J., Kawamura, G., & Nogami, M. (2008). Preparation of Au-Ag, Ag-Au core-shell bimetallic nanoparticles for surface-enhanced Raman scattering. *Scripta Materialia*, 58(10), 862-865. <https://doi.org/10.1016/j.scriptamat.2008.01.017>
- Yu, K., Sun, X., Pan, L., Liu, T., Liu, A., Chen, G., & Huang, Y. (2017). Hollow Au-Ag Alloy Nanorices and Their Optical Properties. *Nanomaterials (Basel, Switzerland)*, 7(9), 255. <https://doi.org/10.3390/nano7090255>
- Zhang, C., Jiang, S. Z., Yang, C., Li, C. H., Huo, Y. Y., Liu, X. Y., Liu, A. H., Wei, Q., Gao, S. S., Gao, X. G., & Man, B. Y. (2016). Gold@silver bimetal nanoparticles/pyramidal silicon 3D substrate with high reproducibility for high-performance SERS. *Scientific Reports*, 6, 25243. <https://doi.org/10.1038/srep25243>
- Zhang, L., Chen, L., Liu, H., Hou, Y., Hirata, A., Fujita, T., & Chen, M. (2011). Effect of Residual Silver on Surface-Enhanced Raman Scattering of Dealloyed Nanoporous Gold. *The Journal of Physical Chemistry C*, 115(40), 19583-19587. <https://doi.org/10.1021/jp205892n>
- Zhang, Q., Cobley, C. M., Zeng, J., Wen, L.-P., Chen, J., & Xia, Y. (2010). Dissolving Ag from Au-Ag Alloy Nanoboxes with H₂O₂: A Method for Both

- Tailoring the Optical Properties and Measuring the H₂O₂ Concentration. *The Journal of Physical Chemistry C*, 114(14), 6396-6400. <https://doi.org/10.1021/jp100354z>
- Zhang, Y., Yang, C., Xue, B., Peng, Z., Cao, Z., Mu, Q., & Xuan, L. (2018). Highly effective and chemically stable surface enhanced Raman scattering substrates with flower-like 3D Ag-Au hetero-nanostructures. *Scientific reports*, 8(1), 898. <https://doi.org/10.1038/s41598-018-19165-9>
- Zhang, Y. D. a. Z. (2016). Nanoporous Metals for Advanced Energy Technologies. XIV, 223. <https://doi.org/10.1007/978-3-319-29749-1>
- Zhao, X., Wen, J., Zhang, M., Wang, D., Wang, Y., Chen, L., Zhang, Y., Yang, J., & Du, Y. (2017). Design of Hybrid Nanostructural Arrays to Manipulate SERS-Active Substrates by Nanosphere Lithography. *ACS Applied Materials & Interfaces*, 9(8), 7710-7716. <https://doi.org/10.1021/acsami.6b14008>
- Zhou, M., Zhou, S., Chen, G., Li, Y., & Liu, D. (2016). Optical performance of ultra-thin silver films under the attenuated total reflection mode. *Frontiers of Optoelectronics*, 9(4), 549-554. <https://doi.org/10.1007/s12200-016-0574-7>
- Zhou, Q., Zhang, X., Huang, Y., Li, Z., Zhao, Y., & Zhang, Z. (2012). Enhanced surface-enhanced Raman scattering performance by folding silver nanorods. *Applied Physics Letters*, 100(11), 113101. <https://doi.org/10.1063/1.3694056>

APPENDICES

APPENDIX A

DETERMINATION OF 4-MBA MOLECULES ADSORBED ON SERS SUBSTRATES

In our experiment, the difference in number of 4-MBA adsorbed on the Au-Ag alloyed substrate and the Au-Ag dealloyed substrate was indirectly determined by a weak acid-strong base titration method. The titration of 4-MBA (a weak acid) occurs via a hydrolysis reaction with a strong base (NaOH). Briefly, the SERS substrates were immersed overnight in 200 μ l of 15 mM 4-MBA dissolved in ethanol. The supernatant or unbound 4-MBA molecules of the solution was kept for titration with NaOH. By knowing the concentration and volume of NaOH needed for the half-neutralization or equivalence point of titration, the number of unbound 4-MBA molecules was determined. As a result, the adsorbed molecules on the SERS surfaces were estimated by the following equation;

$$N_{4\text{-MBA on SERS substrate}} = N_{\text{initial 4-MBA}} - N_{\text{unbound 4-MBA}}$$

In the titration process, the unbound 4-MBA molecules were first dissolved into ethanol to reach a final volume of 2 ml, followed by slowly adding 0.01 M NaOH into the 4-MBA solution and measuring pH until the value indicates neutral pH. At the equivalent point, the moles of added NaOH equals to the moles of unbound 4-MBA molecules thus we can calculate the number of 4-MBA molecules on SERS substrates as follows:

Au-Ag Alloyed Substrate

Volume of NaOH at equivalence point = 0.29 ml

Amount of added NaOH at equivalence point

$$= (0.01 \text{ M} \times 0.29) \div 1000 = 2.9 \mu\text{mol}$$

Number of unbound 4-MBA molecules

$$= (2.9 \times 10^{-6} \text{ mol}) \times (6.02 \times 10^{23} \text{ molecules}) = 1.745 \times 10^{18} \text{ molecules}$$

As above equation; $N_{4\text{-MBA on SERS substrate}} = N_{\text{initial 4-MBA}} - N_{\text{unbound 4-MBA}}$

$$N_{\text{initial 4-MBA}} = \left(15 \times 10^{-3} \frac{\text{mol}}{\text{l}} \times 0.2 \text{ ml}\right) \div (1000) \times 6.02 \times 10^{23} \frac{\text{molecules}}{\text{mol}}$$

$$= 1.806 \times 10^{18} \text{ molecules}$$

Therefore, $N_{4\text{-MBA}}$ on Au-Ag alloyed substrate

$$= 1.806 \times 10^{18} - 1.745 \times 10^{18} = 6.1 \times 10^{16} \text{ molecules}$$

Au-Ag Dealloyed Substrate

Volume of NaOH at equivalence point = 0.23 ml

Amount of added NaOH at equivalence point

$$(0.01 \text{ M} \times 0.23) \div 1000 = 2.32 \mu\text{mol}$$

Number of unbound 4-MBA molecules

$$= (2.32 \times 10^{-6} \text{ mol}) \times (6.02 \times 10^{23} \text{ molecules}) = 1.396 \times 10^{18} \text{ molecules}$$

$N_{4\text{-MBA}}$ on Au-Ag dealloyed substrate

$$= 1.806 \times 10^{18} - 1.396 \times 10^{18} = 4.1 \times 10^{16} \text{ molecules}$$

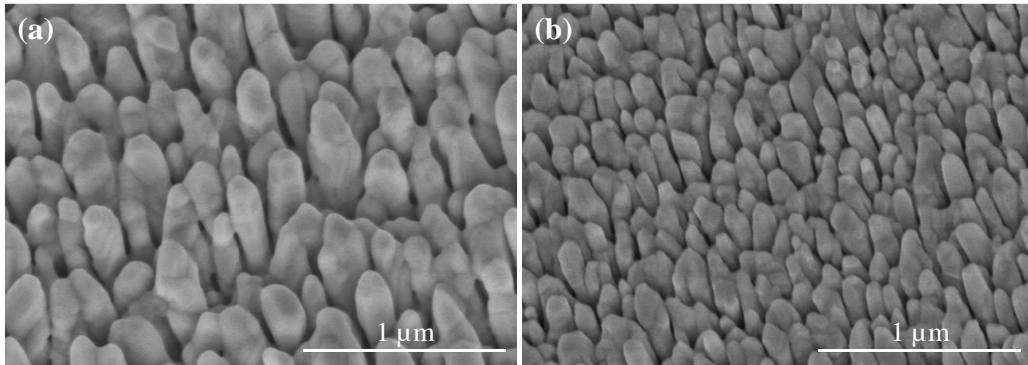
APPENDIX B

SYNTHESIS AND MORPHOLOGY OF PURE AG AND AU SUBSTRATES

The pure Au and Ag nanostructures were fabricated on $3 \times 3 \text{ cm}^2$ *p*-type silicon (100) wafers by co-sputtering with OAD technique. For fabricating the pure metal substrates, two identical targets (Au or Ag) were used in the sputtering process while the power of the two sputter guns was operated at 80 W and 10 W, respectively. During the process, argon gas was purged at a constant flow rate of 20 SCCM at pressure of 5×10^{-3} Torr with a base pressure maintained at 6.5×10^{-6} Torr. The silicon substrate was tilted at a constant angle of 86° with regard to the sputtering targets, and the deposition time was 20 minutes per sample. The morphology of the deposited samples showed the deposited Au and Ag are presented in nanorod structure (Figure A1). The average diameter of the Ag and Au nanorods obtained in this way was $155 \pm 23 \text{ nm}$ and $113 \pm 15 \text{ nm}$, respectively.

Figure B1

SEM Images of (a) Pure Ag and (b) Pure Au Substrates.



APPENDIX C

SERS ENHANCEMENT FACTOR CALCULATION

The SERS enhancement factor (EF) is described as the intensity ratio between the SERS signal and that expected from regular non-SERS Raman scattering for a given analyte molecule, normalized by the special number of the probed molecule. The EF can be calculated by equation 3.1.

Calculation of N_{Raman} and N_{SERS}

In the experiment, 2 μl of 0.1 M 4-MBA dissolved in ethanol was dropped on a bare silicon substrate, and the same amount of 4-MBA solution (2 μl , 0.1 M) was dropped on the SERS substrates. The 4-MBA solution was well dispersed on all substrates which contain a surface area of 25 mm^2 ($A_{4\text{-MBA}}$). For Raman measurement using a 50X objective lens, the area of the laser spot size was approximately 1 μm^2 (A_{laser}). The calculation of the desired value was therefore performed as the following:

$$N_{\text{Raman}} = (4\text{-MBA concentration}) (\text{Avogadro number}) (\text{Volume of 4-MBA drop}) (A_{\text{laser}}/A_{4\text{-MBA}})$$

$$N_{\text{Raman}} = (0.1)(6.02 \times 10^{23})(2 \times 10^{-6}) \left(\frac{1}{25} \times 10^{-6}\right) = 4.81 \times 10^9 \text{ molecules}$$

$$N_{\text{SERS}} = 4\text{-MBA 1 monolayer} \sim 1.55 \text{ nm}^2 \text{ (Compared with laser spot } \sim 1 \mu\text{m}^2)$$

$$N_{\text{SERS}} = \text{laser spot/ 4-MBA 1 monolayer} = \left(\frac{1 \times 10^{-12}}{1.55 \times 10^{-18}}\right) = 6.45 \times 10^5 \text{ molecules}$$

Calculation of EF

Au-Ag alloyed substrate;

$$\frac{12813.93}{207.43} \times \frac{4.81 \times 10^9}{6.45 \times 10^5} = 4.6 \times 10^5$$

Au-Ag dealloyed substrate;

$$\frac{41914.81}{207.43} \times \frac{4.81 \times 10^9}{6.45 \times 10^5} = 1.5 \times 10^6$$

Table C1

The Enhancement Factor of Au-Ag Alloyed and Dealloyed SERS Substrate Synthesized With Various Methods and Structures.

SERS substrate	Alloy synthesis method	Etching solution	Raman probe	EF	References
Au-Ag nanowires	Electrodeposition using AAO membrane as a template	15% HNO ₃	4-MBA	5.41×10 ⁶	(Wiryakun et al., 2016)
Dealloyed nanoporous Au films	Sputtering	Concentrated HNO ₃	Rhodamine B	2.4×10 ⁵	(Hu et al., 2019)
Gradient nanoporous gold	Co-sputtering	70% HNO ₃	R6G	10 ⁷	(Huang et al., 2017)
Au–Ag alloy nanoboxes	Reduction of HAuCl ₄ and AgNO ₃	-	4-MBA	10 ⁶	(Li et al., 2018)
Au-Ag alloy nanowires	Electrodeposition using AAO membrane as a template	-	4-MBA	10 ⁵	(Sanguansap et al., 2020)

gold/silver bi-layer film with alumina coating	Thermal evaporation	-	R6G	2×10^4	(Mahurin et al., 2011)
SERS substrate	Alloy synthesis method	Etching solution	Raman probe	EF	References
gold nanoparticle s decorated Au-Ag tubes (Au@Au-AgTs)	Galvanic replacement reaction	-	4-nitrothiophenol (4-NTP)	2.5×10^5	(Ankudze & Pakkanen, 2018)
Ag-Au alloy microflowers	Thermolysis of metal-alkyl ammonium halide	-	1,2,3-benzotriazole (BTA)	1.38×10^7	(Pawar et al., 2019)

APPENDIX D

OTHER ORGANIC MOLECULES DETECTION

In order to correlate testing of Raman signals with 4-MBA, other kinds of Raman active molecules including methylene blue (MB) and crystal violet (CV) were also studied. Figure A3 shows Raman spectra of MB and CV adsorbed on the Au-Ag alloyed and dealloyed substrates. Raman spectra of MB presented characteristic peaks at 447, 1394 and 1626 cm^{-1} which are assigned to C–N–C skeletal bending, C–H in-plane ring deformation and C–C stretching respectively (Xiao & Man, 2007). The characteristic peaks of CV occurred at 913, 1174 and 1388 cm^{-1} are assigned to the ring skeletal vibrations, C–H in-plane bending vibrations and N-phenyl stretching, respectively. Peaks shown at 1588 and 1620 cm^{-1} are attributed to ring C–C stretching (Mao et al., 2012; Rekha et al., 2018). Overall, Raman intensities of such molecules on the Au-Ag dealloyed substrates were ca. 1.5 times larger than those originating from the Au-Ag alloyed SERS substrates.

Figure D1

(a) Raman Spectra of CV and MB Molecules Adsorbed on the Au-Ag Alloyed and Dealloyed SERS Substrates. (b) Comparison of Raman Intensity of Major CV Peak 1620 cm^{-1} and Major MB at 1626 cm^{-1} .

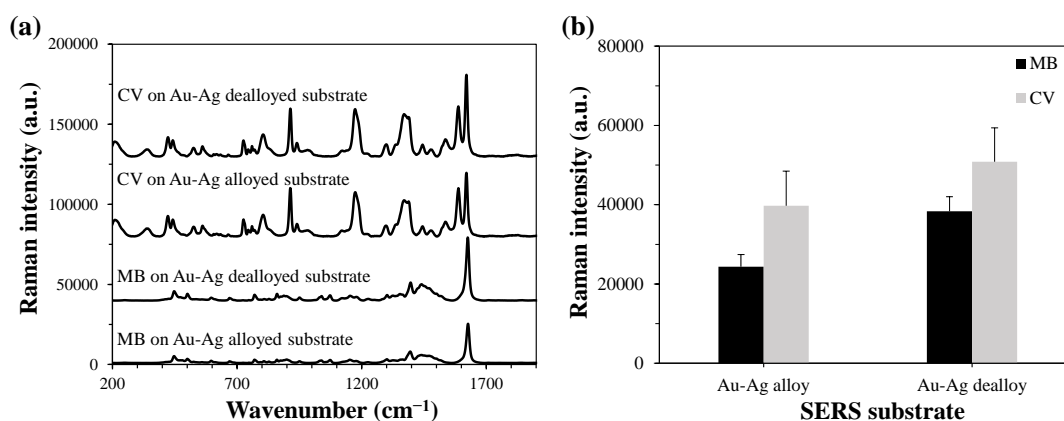


Table D1*Peak Frequencies and Assignments for CV and MB*

Molecule	Wavenumber (cm ⁻¹)	Assignment
Crystal violet	206	Breathing of central bonds
	336	In-plane vibration of phenyl-C-phenyl
	423	Out-of-plane vibrations of phenyl-C-phenyl
	524, 561	Ring skeletal vibration of radical orientation
	724, 913	Out-of-plane vibrations of ring C-H
	1169	In-plane vibrations of ring C-H
	1297	Ring C-C stretching
	1389	N-phenyl stretching
	1538, 1620	Ring C-C stretching
Methylene blue	1617	C-C ring stretching
	1597	C-C ring stretching
	1513	C-C antisymmetric stretching
	1442	C-N antisymmetric stretching
	1396	C-H in-plane ring deformation
	1301	-
	1184	C-N stretching
	1121	c(C-H) out-of-plane bending
1030	C-H in-plane bending	

Molecule	Wavenumber (cm ⁻¹)	Assignment
Methylene blue	670	C-H out-of-plane bending
	612	C-S-C skeletal deformation
	502	C-N-C skeletal deformation
	449	C-N-C skeletal deformation
	246	Ag-N stretching

Table D2

SERS Bands of Urinary Crystals and Assignments of Corresponding Vibrational Modes

Crystals	Wavenumber (cm ⁻¹)	Assignment
Calcium oxalate monohydrate	505	O-C-O in plane bending
	521	O-C-O in plane bending
	898	C-C stretching
	1465	C-O symmetric stretching
	1491	C-O symmetric stretching
Calcium phosphate	1631	C-O asymmetric stretching
	434	Symmetric and antisymmetric bending of PO ₄ ³⁻
	452	Symmetric and antisymmetric bending of PO ₄ ³⁻
	584	Symmetric and antisymmetric bending of PO ₄ ³⁻

Crystals	Wavenumber (cm ⁻¹)	Assignment	
Calcium phosphate	599	Symmetric and antisymmetric bending of PO ₄ ³⁻	
	614	Symmetric and antisymmetric bending of PO ₄ ³⁻	
	949	Internal vibration	
	964	Symmetric stretching of PO ₄ ³⁻	
	1031	Antisymmetric stretching of PO ₄ ³⁻	
	1052	Antisymmetric stretching of PO ₄ ³⁻	
	1084	Antisymmetric stretching of PO ₄ ³⁻	
	Uric acid	385	C-N-C ring vibration
		472	C-N-C ring vibration
503		C-N-C ring vibration	
562		Ring vibration	
627		Ring breathing mode	
659		Skeletal ring deformation	
707		N-H out of plane and in-plane bending	
784		Ring vibration	
885		N-H out of plane and in-plane bending	
999		C-O, C-C, C-N ring vibration	
1039		C-O, C-C, C-N ring vibration	
1122		C-N ring vibration	
1234		C-O, C-C, C-N ring vibration	

	1288	C-O, C-C, C-N ring vibration
	1356	C-O ring vibration
Crystals	Wavenumber (cm^{-1})	Assignment
Uric acid	1499	C-C, C-N stretching
	1595	C-C, C-N stretching
	1652	C=O stretching

Table D3

Constituents in Synthetic Urine

Constituents	Concentration (g/l)
$\text{CaCl}_2 \cdot 2\text{H}_2\text{O}$	0.65
$\text{MgCl}_2 \cdot 6\text{H}_2\text{O}$	0.65
NaCl	4.6
Na_2SO_4	2.3
$\text{Na}_3\text{Citrate} \cdot 2\text{H}_2\text{O}$	0.65
$\text{Na}_2(\text{COO})_2$	0.02
$\text{KH}_2\text{PO}_4^{\text{a}}$	4.2
KCl	1.6
NH_4Cl	1
$\text{CO}(\text{NH}_2)_2^{\text{a}}$	25
$\text{C}_4\text{H}_7\text{N}_3\text{O}$	1.1

VITA

Name Miss. Uraiwan Waiwijit

Birth date 15 August 1985

Telephone number +66(0)896898235

E-mail u.waiwijit@gmail.com

Education B.Sc. (Medical Technology), Faculty of Allied Health Science, Chulalongkorn University, Thailand (GPA 3.55, 2nd Class Honor) (2004-2008)

M.Sc. (Medical Biochemistry), Faculty of Medicine, Chulalongkorn University, Thailand (GPA 3.96) (2008-2010)

Address 112 Thailand Science Park, Phahonyothin Road, Klong 1, Klong Luang, Pathumthani, 12120 Thailand.

National publications

Waiwijit, U., Boonla, C., Kitikowit, W., Supoj, R., Borwornpadungkitti, S., (2010). Expression of 8-hydroxydeoxyguanosine in nephrolithiatic renal tissues and toxicity of calcium oxalate monohydrate to human kidney cell line. *The Thai Journal of Urology*, 31(2), 137-146.

International publications

Waiwijit, U., Kandhavivorn, W., Oonkhanond, B., Lomas, T., Phokaratkul, D., Wisitsoraat, A., & Tuantranont, A. (2014). Cytotoxicity assessment of MDA-MB-231 breast cancer cells on screen-printed graphene-carbon paste substrate. *Colloids and Surfaces B: Biointerfaces*, 113, 190-197. <https://doi.org/10.1016/j.colsurfb.2013.09.008>

Kitikowit, W., Waiwijit, U., Boonla, C., Ruangvejvorachai, P., Pimratana, C., Predanon, C., Ratchanon, S., & Tosukhowong, P. (2014). Increased oxidative DNA damage seen in renal biopsies adjacent stones in patients with nephrolithiasis. *Urolithiasis*, 42(5), 387-394. <https://doi.org/10.1007/s00240-014-0676-x>

- Waiwijit, U., Phokaratkul, D., Kampeera, J., Lomas, T., Wisitsoraat, A., Kiatpathomchai, W., & Tuantranont, A. (2015). Graphene oxide based fluorescence resonance energy transfer and loop-mediated isothermal amplification for white spot syndrome virus detection. *J Biotechnol*, *212*, 44-49. <https://doi.org/10.1016/j.jbiotec.2015.08.003>
- Jaruwongrungee, K., Waiwijit, U., Wisitsoraat, A., Sangworasil, M., Pintavirooj, C., & Tuantranont, A. (2015). Real-time multianalyte biosensors based on interference-free multichannel monolithic quartz crystal microbalance. *Biosens Bioelectron*, *67*, 576-581. <https://doi.org/10.1016/j.bios.2014.09.047>
- Jaruwongrungee, K., Waiwijit, U., Withayachumnankul, W., Matusos, T., Phokaratkul, D., Tuantranont, A., Wlodarski, W., Martucci, A., & Wisitsoraat, A. (2015). Microfluidic-based Split-Ring-Resonator Sensor for Real-time and Label-free Biosensing. *Procedia Engineering*, *120*, 163-166. <https://doi.org/10.1016/j.proeng.2015.08.595>
- Waiwijit, U., Matusos, T., Pakapongpan, S., Phokharatkul, D., Wisitsoraat, A., & Tuantranont, A. (2016). Highly cytocompatible and flexible three-dimensional graphene/polydimethylsiloxane composite for culture and electrochemical detection of L929 fibroblast cells. *The Journal of Biomaterials Applications*, *31*(2), 230-240. <https://doi.org/10.1177/0885328216656477>
- Chuaypen, N., Boonla, C., Dissayabutra, T., Predanon, C., Ruangvejvorachai, P., Waiwijit, U., & Tosukhowong, P. (2017). Increased intrarenal expression of sodium-dicarboxylate cotransporter-1 in nephrolithiasis patients with acidic urine pH. *Asian Biomedicine*, *7*(4), 571-577. <https://doi.org/10.5372/1905-7415.0704.214>
- Waiwijit, U., Chananonwathorn, C., Eimchai, P., Bora, T., Hornyak, G. L., & Nuntawong, N. (2020). Fabrication of Au-Ag nanorod SERS substrates by co-sputtering technique and dealloying with selective chemical etching. *Applied Surface Science*, *530*, 147171. <https://doi.org/10.1016/j.apsusc.2020.147171>